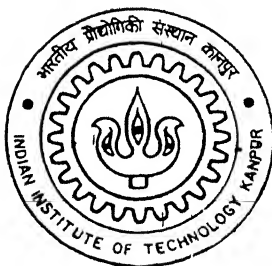


UPSTREAM EFFECT OF VORTEX SHEDDING AROUND BLUFF BODIES

By

K. ARUN



DEPARTMENT OF AEROSPACE ENGINEERING

Indian Institute of Technology Kanpur

JANUARY, 2002

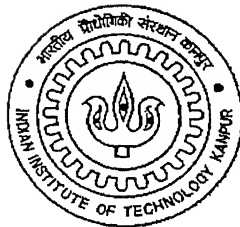
UPSTREAM EFFECT OF VORTEX SHEDDING AROUND BLUFF BODIES

*A Thesis Submitted in Partial Fulfillment of the Requirements
for the Degree of*

MASTER OF TECHNOLOGY

by

K. ARUN



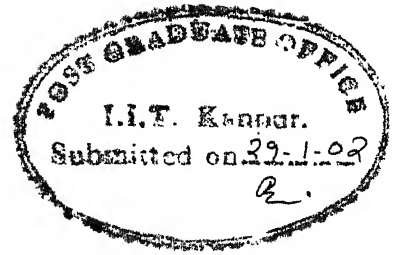
**Department of Aerospace Engineering
Indian Institute of Technology Kanpur, India
January, 2002**

- 5 MAR 2002 / AE

पुष्पोत्तम काशीनाथ केवटार पुस्तकालय
भारतीय प्रौद्योगिकी संस्थान, कानपुर
अवाप्ति क्र० **137900**



A137900



CERTIFICATE

It is certified that the work contained in the thesis entitled
“Upstream effect of Vortex Shedding around Bluff Bodies”,
by K. Arun, has been carried out under my supervision and
that this work has not been submitted elsewhere for a degree

A.K. Gupta

(Dr. A. K. Gupta)

28.1-2002

Professor,
Department of Aerospace Engineering,
Indian Institute of Technology,
Kanpur.

ABSTRACT

An experimental investigation to study the effect of Karman vortex shedding felt upstream of 2-D bluff bodies in subcritical Reynolds number range ($6.7 \times 10^3 - 2.1 \times 10^4$) is carried out. The experiments were carried out in a subsonic closed circuit closed test section wind tunnel facility, which was made operational after the installation of the transition sections and Siemens make frequency controlled speed control driving unit of two 15 HP induction motors.

The 2-D bluff body models of circular, triangular and square cross sections were tested for two test section speeds 4 m/s and 10 m/s. In all cases the flow is taking place normal to the cylindrical axis. A single wire hot wire probe is used to get the velocity fluctuations with the help of a mini CTA (DANTEC). FFT was performed to get the power spectra of the velocity fluctuations at all locations around the models. Spectral analysis of the power spectra of velocity fluctuations for a circular cylinder show a single strong spectral peak of dominant frequency at one diameter location downstream of the model indicating strong vortex shedding in the wake region. Similar single dominant spectral peaks at the frequency component corresponding to the Strouhal number in the wake region but of lesser intensity of the frequency component corresponding to the Strouhal number in the wake region appear in the model and upstream region as well. From the presence of the spectral peak of the frequency component in the upstream region, it is concluded that the Karman vortex shedding in the wake region has its influence felt all around the circular cylinder and also in the upstream region just ahead of the stagnation point. Similar results are observed in the square cylinder and triangular cylinder cases as well.

Acknowledgements

I express my deep gratitude and indebtedness to Dr. A. K. Gupta, who provided me with invaluable guidance, instruction and inspiration throughout the course of my work.

I convey my heartfelt thanks to Dr. Kamal Poddar for his valuable suggestions related to Lab VIEW and Hot Wire system.

I am also indebted to Dr. E. Rathakrishnan for his constant valuable suggestions and encouragement in my experimental work.

I would like to specially than Mr. K. Mohan who helped me immensely during the crucial phase of experimentation and extend my thanks to Mr. Rameshwar whose cooperation made my work easy in the Aerodynamics Lab.

I also thank Mr.Chauhan for workshop assistance.

I feel myself bound to thank my friends Kapil and Hasim for clarifying all the fundamentals related to signal processing and helping me when ever the need arose. My thanks are also due to all my friends who helped me in various ways and at various stages.

Nomenclature

ADC	Analog to Digital Converter
CTA	Constant Temperature Anemometer
DAQ	Data acquisition
D,d	Dimension of the model normal to flow
h	Height of the test section
L	Length of the model
Re	Reynolds number
St	Strouhal number
U_{mean}	Mean velocity
u_{rms}	RMS of fluctuating velocity
U_o, U_{∞}	Free stream velocity
x, X	Free stream co-ordinate
y, Y	Normal co-ordinate
ν	Kinematic viscosity

CONTENTS

	Page No:
Certificate	ii
Abstract	iii
Acknowledgement	iv
Nomenclature	v
Contents	vi
List of Figures	viii
1. INTRODUCTION	1
1.1 Present Investigation	2
2. LITERATURE REVIEW	3
2.1 Circular Cylinder	3
2.2 Other Bluff Bodies	6
3. EXPERIMENTAL SET-UP	9
3.1 Test Facility	9
3.1.1 The Test Section	9
3.1.2 Diffuser Sections	10
3.1.3 Fan Section	10
3.1.4 Transition Sections	11
3.1.5 Contraction Cone	11
3.2 Velocity Measurement	12
3.3 Hot Wire	12
3.4 Data Acquisition	13
3.4.1 Transducer	13
3.4.2 DAQ hard ware	13
3.4.3 Software	15
3.5 Models	15
3.6 Traverse Mechanisms	16
3.7 Precautions	16
4. RESULTS AND DISCUSSION	24
4.1 Test Section Measurements	24
4.2 Circular Cylinder	25
4.2.1 Wake Region (10m/s)	25
4.2.2 Model Region (10m/s)	26
4.2.3 Upstream Region (10 m/s)	27
4.2.4 Circular Cylinder (4 m/s)	28
4.3 Square Cylinder	29
4.3.1 Wake Region (10m/s)	29

4.3.2 Model Region (10m/s)	30
4.3.3 Upstream Region (10 m/s)	31
4.3.4 Square Cylinder (4m/s)	31
4.4 Triangular Cylinder	32
4.4.1 Wake Region (10m/s)	33
4.4.2 Model Region (10m/s)	33
4.4.3 Upstream Region (10 m/s)	33
4.4.4 Triangular Cylinder (4 m/s)	34
4.5 Mean Velocity and RMS Fluctuations	34
4.5.1 Circular Cylinder	35
4.5.2 Square Cylinder	36
4.5.3 Triangular Cylinder	37
4.6 Discussion	38
4.6.1 Strouhal Number	39
4.6.2 U_{mean} Variation in the Model and Upstream Region	40
4.6.3 u_{rms} Variation in the Model and Upstream Region	40
5. CONCLUSIONS AND SUGGESTIONS	81
5.1 Circular Cylinder Model	81
5.2 Square and Triangular Cylinder Models	82
5.3 Strouhal Number	83
5.4 Suggestions for Future Work	83
6. REFERENCES	84

	List of Figures	Page No:
3.1	Plan view of model wind tunnel	18
3.2	Test section	19
3.3	Fan and the motor section	20
3.4	Cross sectional view of first transition section	20
3.5	Cross sectional view of second transition section	21
3.6	Transition section and the fan section	21
3.7	Control panel of the 3 phase induction motor	22
3.8	Circular cylinder model mounted in the test section	22
3.9	3-D traversing mechanism	23
3.10	Experimental set-up	23
4.1	Calibration of test section speed with motor RPM	41
4.2	Velocity profile downstream of test section for different motor RPM	42
4.3	Models and probe locations	43
4.4	Power spectra and time traces of velocity fluctuations for circular cylinder 10 m/s wake region	44
4.5	Decay of power spectra and time traces in the vertical direction for circular cylinder 10 m/s wake region	45
4.6	Power spectra and time traces of velocity fluctuations for circular cylinder 10 m/s model region	46
4.7	Decay of power spectra and time traces in the vertical direction for circular cylinder 10 m/s model region	47
4.8	Power spectra and time traces of velocity fluctuations for circular cylinder 10 m/s upstream region	48
4.9	Power spectra and time traces of velocity fluctuations for circular cylinder 4 m/s wake region	49
4.10	Decay of power spectra and time traces in the vertical direction for circular cylinder 4 m/s wake region	50
4.11	Power spectra and time traces of velocity fluctuations for circular cylinder 4 m/s model region	51
4.12	Decay of power spectra and time traces in the vertical direction for circular cylinder 4 m/s model region	52
4.13	Power spectra and time traces of velocity fluctuations for circular cylinder 4 m/s upstream region	53
4.14	Power spectra and time traces of velocity fluctuations For square cylinder 10 m/s wake region	54
4.15	Power spectra and time traces of velocity fluctuations For square cylinder 10 m/s model region	55
4.16	Decay of power spectra and time traces in the vertical direction for square cylinder 10 m/s model region	56
4.17	Power spectra and time traces of velocity fluctuations For square cylinder 10 m/s upstream region	57

4.18	Power spectra and time traces of velocity fluctuations For square cylinder 10 m/s upstream region	58
4.19	Power spectra and time traces of velocity fluctuations For square cylinder 4 m/s wake region	59
4.20	Power spectra and time traces of velocity fluctuations For square cylinder 4 m/s model region	60
4.21	Decay of power spectra and time traces in the vertical direction for square cylinder 4 m/s model region	61
4.22	Power spectra and time traces of velocity fluctuations For square cylinder 4 m/s upstream region	62
4.23	Power spectra and time traces of velocity fluctuations For square cylinder 4 m/s upstream region	63
4.24	Power spectra and time traces of velocity fluctuations For Triangular cylinder 10 m/s wake region	64
4.25	Power spectra and time traces of velocity fluctuations For Triangular cylinder 10 m/s model region	65
4.26	Decay of power spectra and time traces in the vertical direction for Triangular cylinder 10 m/s model region	66
4.27	Power spectra and time traces of velocity fluctuations For Triangular cylinder 10 m/s upstream region	67
4.28	Power spectra and time traces of velocity fluctuations For Triangular cylinder 4 m/s wake region	68
4.29	Power spectra and time traces of velocity fluctuations For Triangular cylinder 4 m/s model region	69
4.30	Decay of power spectra and time traces in the vertical direction for Triangular cylinder 4 m/s model region	70
4.31	Power spectra and time traces of velocity fluctuations For Triangular cylinder 4 m/s upstream region	71
4.32	Mean velocity distribution for circular cylinder	72
4.33	RMS velocity fluctuations for circular cylinder in the vertical direction	73
4.34	Mean velocity distribution for square cylinder	74
4.35	RMS velocity fluctuations for square cylinder in the vertical direction	75
4.36	Mean velocity distribution for triangular cylinder	76
4.37	RMS velocity fluctuations for triangular cylinder in the vertical direction	77
4.38	Strouhal number vs Reynolds number for different models	78
4.39	Variation of U_{mean} in the model and upstream region for different models	79
4.40	Variation of urms in the model and upstream region for different models	80

Chapter 1 INTRODUCTION

From aerodynamics point of view bluff bodies are traditionally characterized by high drag and low or negligible lift compared to streamlined bodies at small angle of attack characterized by low drag and high lift. In addition, an important dynamic characteristic of bluff bodies is the vortex shedding in their wake. This dynamic aspect of vortex shedding in the wake of Circular Cylinder was first investigated by Strouhal in 1878 as given in “*Boundary layer theory*” by Schlichting, H. Strouhal also gave an empirical correlation between Strouhal number defined as nd / U_{∞} Where n is the frequency of vortex shedding, d is the diameter of the cylinder, U_{∞} is the free stream velocity, versus the Reynolds number defined as $U_{\infty}d / \nu$, where ν is the kinematic viscosity.

Subsequently, a large number of experimental investigations have been carried out on bluff bodies of different shapes and all of them exhibit the dominant dynamic characteristics of vortex shedding in their wakes. In the middle of last century, after world war II, bluff body aerodynamics gained important recognition due to its relevance to the problem of wind loading on civil engineering, tall terrestrial structures like tall chimneys, towers of lattice construction, hyperbolic cooling towers and tall buildings etc. As a result a large body of literature of laboratory and field experiments have become available mainly in the *Journal of Wind Engineering and Industrial Aerodynamics*.

More recently, it has also been recognized relatively that vortex shedding behind a circular cylinder causes cyclic pressure forces on the circular cylinder resulting in cyclic lift and drag forces. It is to be expected that other bluff body shapes will also experience similar periodic forces due to vortex shedding in their wake. This would also imply that the flow field around bluff bodies will undergo a cyclic circulation pattern resulting in flow oscillations and in particular flow velocity oscillations, upstream as well as around the cylinder, especially in the wake region. Numerous

wind tunnel studies have been carried out to investigate the aerodynamics of the vortex shedding characteristics of circular cylinder, one of the most simple and basic shapes of bluff bodies used in fluid dynamics. However, most of the experimental data available are for the downstream of the bluff body model especially in the wake region.

Nishimura, H. (2001) in his recent studies has investigated the effect of vortex shedding felt upstream of the circular cylinder and has concluded that the stagnation point and the separation points of the cylinder fluctuated synchronously with the vortex shedding.

Smoke flow visualization of 2-D bluff bodies yield some good qualitative results on vortex shedding characteristics like the fluctuation of separation points, stagnation point and information about the vortex shedding wake region. Close observation will show that the fluctuation of the stagnation point has something to do with the vortex shedding, but there is not much study on this aspect in the upstream region of the bluff bodies. So, this was the prime factor to take up the study. Moreover the task of taking a closed circuit model wind tunnel facility without the power unit to an operational state was itself a major challenge and was taken up and successfully completed to enable the conduct of present experimental investigation.

1.1 PRESENT INVESTIGATION

The entire present experimental investigation can be considered as made up of two phases. Phase I comprised of getting the model wind tunnel facility fully operational, while phase II comprised of conducting the wind tunnel tests in the operational model wind tunnel facility. In the present work experiments were conducted to investigate the effect of the Karman vortex shedding felt upstream of the cylinder for subcritical Reynolds number range. Conducting similar experiments for other basic bluff body geometries further validated the results. The work for the low speed closed test section closed circuit Model Wind Tunnel Facility started two decades ago but was incomplete for various reasons. One of the main objectives of the present work was to

make this facility operational. The tunnel was made operational after the installation of two, 3-phase 15 HP, AC-induction motor (speed control by frequency variation) along with the rotor assembly and with the design, fabrication and installation of the transition sections connecting the driving unit with the rest of the wind tunnel. The turbulence level, flow angularity, boundary layer growth, test section speed were measured before the start of the wind tunnel experiments.

The second phase was to detect the influence of vortex shedding felt upstream in the case of 2-D bluff cylindrical bodies of different cross sections in the sub critical Reynolds number range. The circular cylindrical model was made of aluminum tube with a good surface finish and the square and triangle cylindrical models were made of wood and latter coated with dope for good surface finish. The mean velocity and RMS of fluctuating velocity were measured at different locations for all the models and the emphasis was laid on the upstream region, which is of our present interest. A conventional single Hot Wire probe was used to detect the velocity fluctuations. The velocity fluctuations and corresponding Power Spectrum was obtained for all the models at various locations for two Reynolds number using an on line PC controlled data acquisition system.

Chapter 2 LITERATURE REVIEW

Most of the bluff body aerodynamics investigations are experimental in nature and have focused largely on circular cylinder because of its simplicity of geometry. However other geometries shapes like square cylinder, triangle, disc, flat plat etc have also been studied due to their relevance in wind engineering

2.1 CIRCULAR CYLINDER

Circular cylinder is a classic example of 2-D bluff body. When placed in a flow at very low Reynolds number ($Re < 10$) the flow around circular cylinder is symmetrical upstream and downstream. As the Reynolds number is increased the symmetry disappears and two attached eddies appear behind the cylinder for up to Reynolds number 40, after which the flow becomes unsteady, and at Reynolds number of greater than 100, these attached eddies are periodically shed from the circular cylinder to form Karman vortex street. While the eddy on one side is being shed another one is forming on the other side. This flow pattern is well known as Karman Vortex Street. The Karman Vortex Street is observed downstream of wires (Reyleigh 1915) as Aeolian tones struts of aeroplane, radio and TV towers, antennas, power lines, flame stabilizers and fuel sprays for example. Its applicability is quite wide and important. It is particularly significant if Karman vortex streets induce flutter and resonance in these structures.

The velocity fluctuation in the wake region are regular up to a Reynolds number range of 200, above which the regularity is lost as the laminar vortex undergo transition and produces ultimately a turbulent wake. Despite the transition and turbulent buffeting, markedly periodic vortex shedding remains a characteristic of flow even up to very high Reynolds number (10^7). Roshko, A. (1961) carried out extensive work to find out the Reynolds number effect on vortex shedding and classified the range in to four different regimes i) sub critical, ii) critical,

iii) supercritical, and iv) transcritical. He conducted experiments up to a Reynolds number range of 10^7 and confirmed the existence of vortex shedding but reported that the Strouhal number was highly scattered, explained by the fact that the vortex shedding was not regular in that regime. Another valuable suggestion of his study was to place the probe at 1-D location down stream in fact 2-D location downstream from the trailing edge was best for fluctuation measurements.

Gerrard, J. H. (1965) in his experiment has explained the mechanics of the formation region of vortices behind bluff bodies and has given details of the Strouhal number in the subcritical range, which is the regime of present investigation.

In addition to Roshko's (1961) classification Bearman (1968) suggested another narrow band of vortex shedding region in the range 10^5 to 7.5×10^5 in which the Strouhal number was unusually high of 0.26 and was visibly scattered. Further, his results also confirmed the fact that the probe location at 1-D from the rear of the cylinder was best suited to read peak intensity in fluctuation.

Surry, D. (1971) studied the free stream turbulence effect on the aerodynamic characteristics of the circular cylinder at subcritical Reynolds number and has measured the velocity fluctuations for the front stagnation point but has not related it to the vortex shedding.

Achenbach, E. (1980) studied the influence of surface roughness on the vortex shedding frequency in the wake of circular cylinder. He found that there is no significant change in the Strouhal number in the subcritical regime compared to critical flow regime.

Kiya, M. *et al* (1981) studied the effect of free stream turbulence on flow past circular cylinder and has given a detailed comparison of the Strouhal number with previous studies.

The experimental results of Williamson, C. H. K. (1989) have detailed information regarding the variation of Strouhal number for a wide range of Reynolds numbers. For a cylinder, the Strouhal number is around 0.2, except that it varies uniformly up to Reynolds number 200 and at very high Reynolds number there is discontinuity and

a sharp rise. According to him it is never the same for any two experiments, he explained that factors like cylinder vibration, end effects, L/D ratio, 3-D effect; oblique vortex shedding may be the reason for this. The ranges of values were further verified by numerical calculation study of Franke, R. (1990).

Nishimura, H. (2001) conducted experiment in subcritical Reynolds number regime to study the aerodynamic characteristics of fluctuating forces on a circular cylinder and has demonstrated that the flow around the body depends on vortices shed from the body, then the separated layer and boundary layer along the upwind surface are also influenced by the vortex shedding. The experimental results show that the stagnation and separation points on the bluff body with round corners fluctuated by the influence of the wake oscillation. He used simultaneous surface multi-pressure measuring system to obtain the power spectra of pressure fluctuation on several points on the surface of the cylinder and found clear peaks at the stagnation points. His study also shows that the stagnation point fluctuation ranges from 5° to 8° .

2.2 OTHER BLUFF BODIES

The vortex shedding and the associated fluctuating lift around a circular cylinder have been subjected to considerable research, comparatively little attention has been paid to other sharp edged bluff body shapes. Little is known on the upstream effect of the vortex shedding on bluff bodies although this is a problem of considerable practical significance.

The dynamic characteristic of vortex shedding in the wake is a common feature of bluff bodies. For the cylinder of square cross section the flow is known to separate at the trailing edge corner for low Reynolds number rather than at the leading edge corner, where the separation is indiscernible owing to immediate reattachment, with an increase of Reynolds number the flow separation at the leading edge corners will develop and the steady reattachment becomes impossible.

Vickery, B. J. (1965) studied the free stream turbulence effect on fluctuating lift and drag on a long cylinder of square cross section and the significance of change in angle of attack, and has given a brief comparison with circular cylinder stating that the fluctuating lift forces produced by square section area 3 to 4 times greater than those of the circular cylinder.

Lee, B. E. (1974) studied the effect of turbulence on the surface pressure field of a square prism and found that the strength of vortex shedding is reduced as the intensity of the incident turbulence is increased.

Tomonani (as referred by Okajima, A.) used the smoke visualization technique to measure the distance of the transition point from laminar to turbulent flow and he found that to be in the Reynolds number range of 10^3 and 10^4 . He concluded that at Reynolds number 1000 transition occurs downstream of the trailing edges and the point moves upstream with increase of Reynolds number.

Okajima, A. (1982) conducted experiments on the vortex shedding frequency of various rectangular cylinders of different width to height ratio and summarised that the Strouhal numbers of square cylinder show slight and continuous change around at constant value of 0.13 in the wide range of Reynolds number between 100 and 2.0×10^4 . This is in agreement with experimental findings of Nakaguchi, H. *et al* (1968). Otasuki, Y. *et al* (1974) studied the aero elastic instability of a prismatic bar with square cross section along with the variation of Strouhal number with Reynolds number.

The experimental investigations of cylinders of triangular cross-section are less numerous compared to those of 2-D bluff bodies of other cross section. Like in the case of square cross cylinder the separation of flow around a triangular cylinder takes place at the sharp edges, and the dynamic characteristics of vortex shedding is reported for all Reynolds number range.

Sullerey, R. K. (1974) for his Ph.D. thesis work carried out experiment investigation in the near wake of 2-D bluff bodies to bring out the similarity in distribution of mean flow parameters that included a 90° wedge of triangular cross section. He studied the effect of

blockage ratio on the shape and size of recirculation region for the 2-D bluff bodies. He has given detail plots of mean velocity distribution in the wake region of the 90° wedge.

Buresti, G. (1998) investigated low aspect ratio triangular prisms in cross flow and measured the wake velocity fluctuations for finite length prismatic bodies of triangular cross section with 60° and 90° apex angle oriented in the downstream direction. He found that the velocity fluctuations show dominating frequency immediately outside the wake along all the models, and the magnitude of these fluctuations decreased at a height corresponding to the free end of the bodies. The Strouhal number was also found varying with aspect ratio of the triangular prisms in the range 0.13 to 0.18

Chapter 3 EXPERIMENTAL SET-UP

This chapter gives an overview of the test facility, describes the experimental arrangement, the measurements carried out in the present investigation and various techniques developed for the same, purpose. Also the characteristics of return circuit closed test section subsonic model wind tunnel are described briefly.

3.1 TEST FACILITY

The return circuit closed test section subsonic model wind tunnel facility in the Low Speed Aerodynamics Laboratory of the Aerospace Engineering Department, INDIAN INSTITUTE OF TECHNOLOGY, KANPUR, was made use of for the present experimental investigation. The experiments were conducted for the first time in this test facility and hence a documentation and discussion about the characteristic features of this tunnel are discussed. The plan view of the model wind tunnel is shown in Fig. 3.1

3.1.1 The Test Section

In general the shape and size of the test section is based on the utility and consideration of the aerodynamics of the model to be tested. Flat ceiling and floor are preferred and it has advantage of simplicity in model installation, calibration of external balances, etc. It has also become necessary that almost all wind tunnels have window for better visibility of model mounting and observation of experiments. For the safety reasons, windows of the test section are made of shatter resistant material. The test section of the model wind tunnel is illuminated with almost one third of the total wall area made of Perspex. The rectangular test section has a cross section of 42cm * 60 cm and a length of 198 cm. It has good accessibility with three doors, two made of Perspex, on one side and a wooden door on the other side. One side of the test section in front is made of 3 mm thick Perspex sheet; the opposite side and the bottom wall are made of 4 mm thick wood. The top wall has three sections, the midsection is made of wood, which has slots for traversing the probe, and other two sections are made of Perspex sheet. A slot of 20 cm * 0.10 cm size was made on the wooden surface from 126 cm from the leading edge of the test section to facilitate the traversing of the vertical probe along the axial direction. A 5 mm slot was located in

the perspex sheet and is used to insert a 3 mm diameter pitotstatic tube to measure the free stream velocity. Another 5mm diameter slot is located on the wooden surface at 36 cm from the first slot, which is used for calibration of test section speed. All the slots were sealed from outside with wooden blocks excepting the one in use. The bottom and side wooden walls were first polished with emery paper and then coated with dope paint for good surface finish. Side view of the test section and the model mounting is shown in the Fig. 3.2.

3.1.2 Diffuser Sections

The purpose of the diffuser is to reduce the speed and recover pressure energy with as little energy loss as possible. Since the power losses at any point in the wind tunnel are expected to vary as the third power of speed. It is generally desired to reduce the speed in the shortest possible distance without incurring flow separation. The pressure recovery and pressure gradients and therefore the risk of separation are dependent on both the diffuser cone angle and area ratio. The optimum ranges of these values are 3° - 6° and 4-6 respectively. The model wind tunnel has three diffuser sections, the first diffuser (immediately following the test section) and the return diffuser (that follow the fan section) have the cone angle and area ratio within the optimum range, while the second short diffuser between the first and second corners has a large cone angle of 7° , which may have some losses due to separation.

3.1.3 Fan Section

The fan can be located anywhere in the closed circuit wind tunnel, but its favorable position is after the second corner, based on many factors like prevention of damage of blades from a failing model, also the noise disturbance does not propagate to the test section. The wind tunnel fan is quite different from aeroplane propeller. It is a ducted fan as it operates in a constant area duct and there is no increase in axial velocity across the fan. The wind tunnel fan “merely” replaces the total pressure losses of the tunnel and model. The model wind tunnel has two single stage six bladed fans of diameter 62 cm and tip clearance of 4 mm (Fig. 3.3). They are driven by two variable speed 15 HP 3 phase induction motors, and the fan speed is varied by frequency control (control panel shown in Fig. 3.7) with an over load capacity of 20 % for 1 hour.

3.1.4 Transition Sections

The transition section is necessary to transit the flow from rectangular cross section of the second corner unit to circular cross section of the ducted fans. As the driving unit, the fan section always has circular cross section. Losses are high in the absence of smooth transition. The model wind tunnel has two separate fan sections, hence a rectangular diverging frame was made first of wood and it was split it into two square sections and smooth tapering circular transition as shown in Fig.3.4 was made using hardboard plywood of 3 mm thickness. In the absence of service door for access to the tunnel the first transition section has been fabricated for easy dismantling to give better accessibility and to service the rotor assembly and the rest of the tunnel.

The second transition is part of the return diffuser or the second diffuser. This section is to incorporate a transition back to rectangular cross section of the second diffuser from circular cross section of the ducted fans. The second transition follows similar design features as that of the first transition section. The circular cross section tapers up to rectangular cross section and extend up to 60 cm starting from the exit of the fan section in to the return diffuser. The cross sectional view of the second transition section is shown in Fig. 3.5. The complete assembly of the first transition section, the fan unit and the second transition unit is shown in Fig. 3.6.

3.1.5 Contraction Cone

It is in fact never conical in shape in spite of the term being used. In case of rectangular cross sections the surface streamlines intersect the side walls and results in secondary flow in the corners. This is minimized by 45° fillet at the start of the nozzle and carrying the fillet through the test section and first diffuser. In the model wind tunnel it runs all along the tunnel walls. For the model wind tunnel the contraction ratio of the contraction cone is around 7 well within the optimum level.

3.2 VELOCITY MEASUREMENT

3mm diameter Pitot static pressure probe was used to measure the free stream velocity, which was placed at 21 cm from the test section entrance. It was connected to digital micro manometer (Furness). The effect of the pressure probe was found to be negligible in the down stream region of the test section where the models were mounted.

3.3 HOT WIRE

A conventional single wire hot-wire probe with following wire properties was used for acquiring the velocity data. The sensor for the hot wire used in the present investigation is made of wollaston platinum rhodium (90/10) wire joined to the prongs by etching and soft soldering.

Sensor resistance, R_{20}	3.3	Ω
Sensor lead resist., R_L	0.29	Ω
Support resistance, R_s	0.02	Ω
Sensor TCR, α_{20}	0.36%	/K
Desired wire temp., T_w	250	$^{\circ}\text{C}$
Temperature of flow	25	$^{\circ}\text{C}$
Operating resist., R_w	3.1	Ω
Total resistance, R_T	6.22	Ω
Overheat ratio, a	1.4	

Probe:	
Probe body diameter	6 mm
Support needle length	25.4 mm
Needle base diameter	3 mm
Needle tip diameter	0.5 mm
Spacing between needles	1.25 mm
Sensor length	1.2 mm

3.4 DATA AQUISION

In the present study software is used to acquire the velocity signals samples from the miniature CTA DANTEC (54T30) at desired sampling rate of 6000 samples per second and store the samples on the hard disk in a binary format. The basic elements of a typical PC-based DAQ system comprises of

- Transducer
- Signal conditioning
- DAQ hardware
- Personal computer
- Software

3.4.1 Transducer

The basic function of a transducer is to sense a physical phenomenon and provide the electrical signal that the DAQ system can measure. In the present study the mini CTA was used as the transducer. The electrical signals produced are proportional to the physical parameter we are monitoring. In the present study it is the velocity fluctuations.

The electrical signals generated by the transducers must be optimized for the input range of the DAQ board. Signal conditioning accessories can amplify low-level signals, and then isolate and filter them for more accurate measurements. In addition, some transducers require voltage or current excitation to generate a voltage output. In the present case all the signal conditioning was done inside the mini CTA.

3.4.2 DAQ hard ware

The basic Analog Input considerations are

- Number of channels
- Sampling rate
- Resolution
- Input range

Number of channels- The number of analog channel inputs will be specified for both single-ended and differential inputs on boards that have both types of inputs. Single-ended inputs are all referenced to a common ground point. These inputs are typically used when the input signals are high level (greater than 1 V), the leads from the signal source to the analog input hardware are short (less than 15 ft), and all input signals share a common ground reference. If the signals do not meet these criteria, one should use differential inputs. With differential inputs, each input has its own ground reference. Noise errors are reduced because the common-mode noise picked up by the leads is canceled out. In the present investigation the number of channel is one.

Sampling Rate – This parameter determines how often analog to digital conversions can take place. A faster sampling rate acquires more points in a given time and can therefore often form a better representation of the original signal. To properly digitize this signal for analysis, the Nyquist sampling theorem stipulates that the sampling rate must be more than twice the rate of maximum frequency component to be detected. In the present investigation at each measurement location 3000 velocity data were recorded at the rate of 6000 samples per second to give 0.5 seconds of real time data.

Multiplexing - A common technique employed for measuring several signals with a single ADC is multiplexing. The ADC samples from one channel, switches to the next channel, samples it, switches to the next channel, and so on. Because the same ADC is sampling many channels instead of one, the effective rate of each individual channel is inversely proportional to the number of channels sampled. In the present investigation it was not required because of one channel use.

Resolution – The number of bits that the ADC uses to represent the analog signal is the resolution. The higher the resolution, the higher the number of divisions the range is broken into, and therefore, the smaller the detectable voltage changes. A 12-bit converter divides the analog range into 4096 divisions. By increasing the resolution to 16 bits, however, the number of codes from the ADC increases from 4096 to 65,536, and one can therefore obtain an extremely accurate digital representation of the analog signal if the rest of the analog input circuitry is designed properly. But in the present study the resolution of the DAC is 12 bit and therefore 4096 divisions.

Range - Range refer to the minimum and maximum voltage levels that the ADC can quantize. The multifunction DAQ boards offer selectable ranges so that the board is configurable to handle a variety of different voltage of different voltage levels. With this flexibility, one can match the signal range to that of the ADC to take best advantage of the resolution available to accurately measure the signal.

The range, resolution, and gain available on a DAQ board determine the smallest detectable change in voltage. This change in voltage represents 1 LSB of the digital value, and is often called the code width. The ideal code width is found by dividing the voltage range by the gain times two raised to the order of bits in the resolution.

In the present case the resolution of the DAQ board is 12bit, has a voltage range of 0 to 5 V and gain of 5. Ideal code width therefore is given by

$$5 / 2 * 2^{12} = 0.61 \mu\text{V}.$$

therefore the theoretical resolution of one bit in the digitized value is $0.61 \mu\text{V}$.

3.4.3 Software

The software required for the sampling was developed using the application tool LabVIEW. In this software we can select the number of channels, sampling rate, buffer size and the minimum number of scans to write at a time on the hard disk. In addition to the above we can supply the use header, which we can use for identification of the sampling parameters during the analysis.

3.5 MODELS

The circular cylinder was hollow aluminum tube polished with fine emery paper, the triangle (equilateral) and square models were made of wood, and the edges were sharp and had a smooth surface finish. The 2-D models spanned the test section of the wind tunnel and was aligned parallel to the bottom plate and normal to the free stream. The models were located at 146 cm down stream of the test section at the height of 21 cm from the bottom surface. The table below gives the dimensions, L/D and the blockage ratios of different models.

	Circular Cylinder	Triangular Cylinder	Square Cylinder
Dimension normal to the flow	31 mm	25 mm	25 mm
Blockage Ratio	7.38 %	5.95 %	5.95 %
L / D	19.35	24	24

The models were fitted by simple screw mechanism, a slot was drilled on the sidewalls and the model was placed in position and was tightened with screws fitted with washer from outside the tunnel wall. In the case of square model the flat surface was fixed normal to the free stream, and in the case of 60° vertex for the triangular model spirit level was used to align the model in position. Circular model mounted in the test section along with the probe is shown in Fig. 3.8

3.6 TRAVERSE MECHANISMS

The hot wire probe was maneuvered to the measurement locations using a traversing mechanism which has three translation degree of freedom with maximum possible displacement of 590 mm, 180 mm, and 170 mm in the stream-wise, span-wise, and vertical directions respectively. The corresponding resolutions are 0.125 mm, 0.05 mm and 0.05 mm, respectively. This traverse mechanism is fitted with digital counters giving the above-mentioned resolution in the vertical direction. The traversing mechanism with the probe placed over the test section is shown in Fig. 3.9.

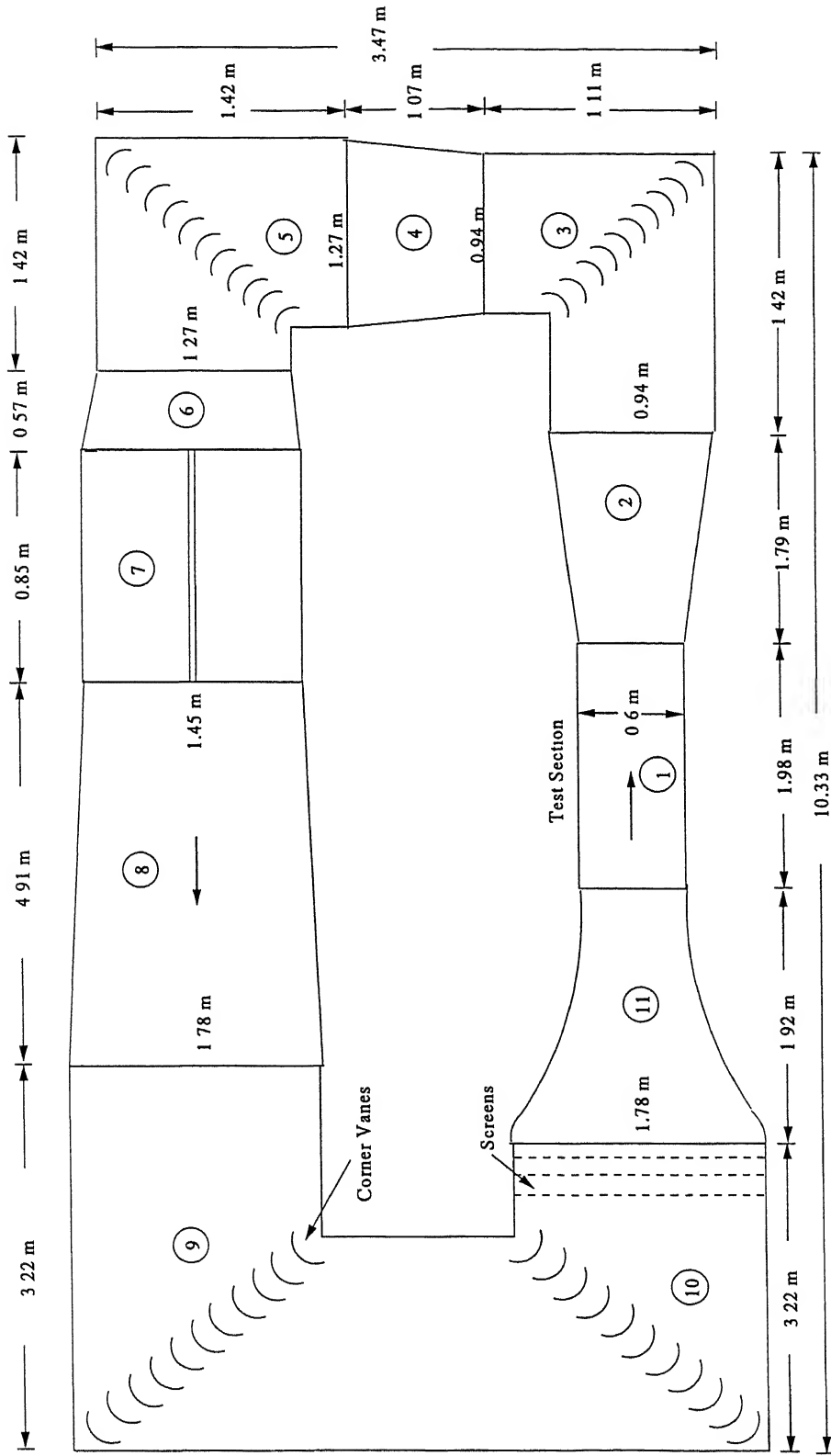
Another vertical traverse mechanism with a displacement in the vertical direction only was used for traversing the pitot static probe. This mechanism has micrometer vernier adjustment and has a resolution of 0.05 mm in the vertical direction.

3.7 PRECAUTIONS

Precautions taken during the course of the experiment are the following.

- Care was taken that the models were mounted parallel with the help of spirit level.
- The digital micro-manometer (Furness) was re-zeroed before the start of each experiment.

- The influence of the pitotstatic tube used to measure the free stream velocity was found negligible downstream of the test section where the models were mounted.
- The hot wire was calibrated every time before each run and the corresponding calibration constants were carefully noted down for further analysis. The error was less than 2 % in all cases.



- 1 - Test Section
- 2 - Diffuser
- 3 - First Corner
- 4 - Second Diffuser
- 5 - Second Corner
- 6 - First Transition
- 7 - Fan Section
- 8 - Return Diffuser
- 9 - Third Corner
- 10 - Fourth Corner
- 11 - Contraction Cone

Plan View - Model Wind Tunnel

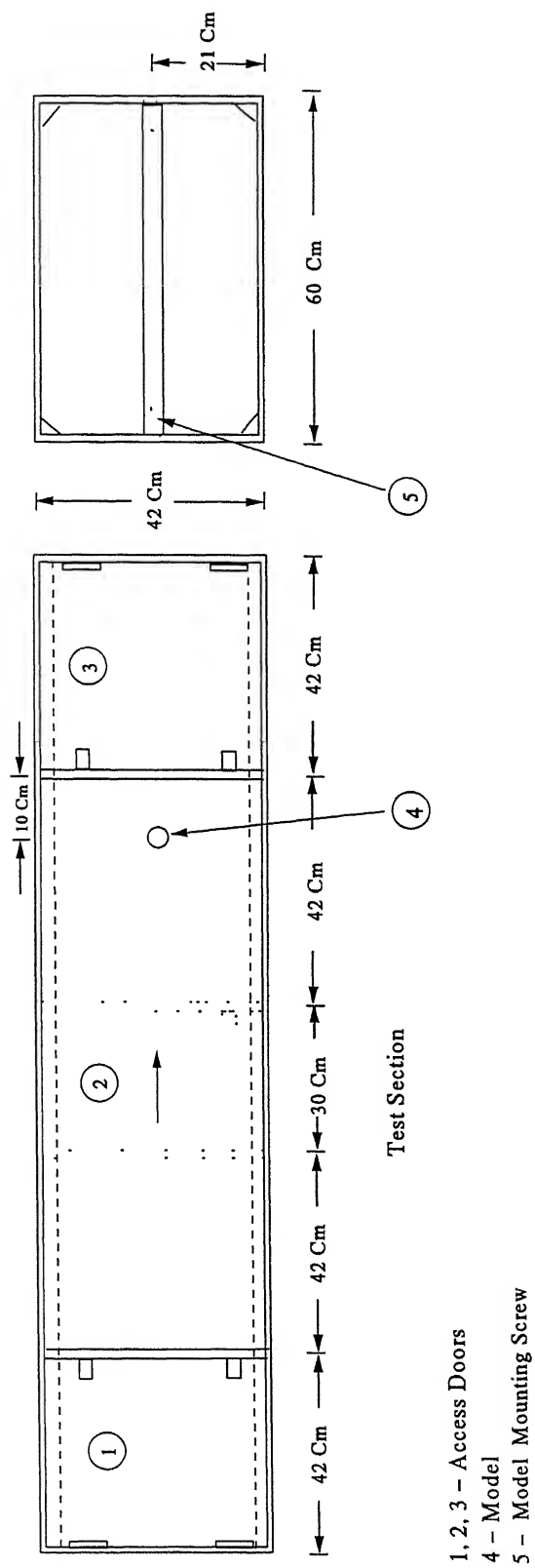


Fig. (3.2) Test Section- Side View



Fig. (3.3) Fan sections and Motor unit

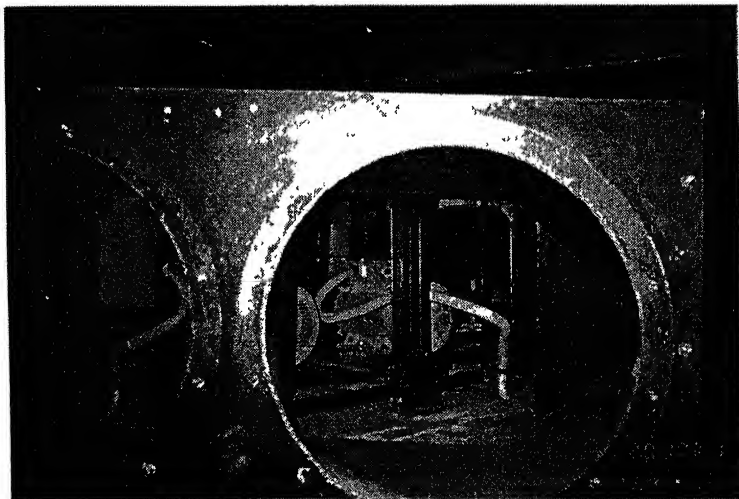


Fig. (3.4) Cross Sectional view of First Transition section

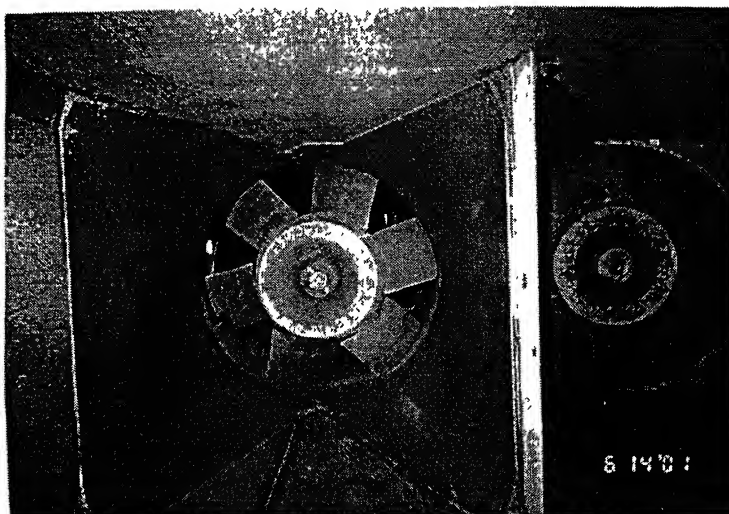


Fig. (3.5) Cross Sectional view of Second Transition section and Fan unit

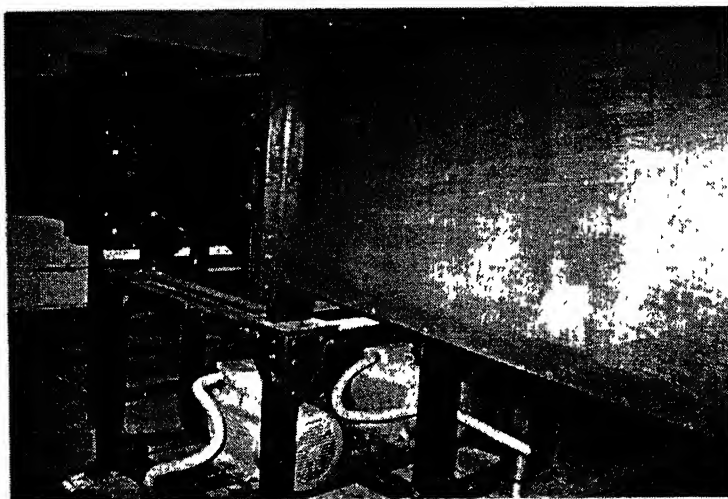


Fig. (3.6) Transition sections along with Driving unit.



Fig. (3.7) Motor Control Panel

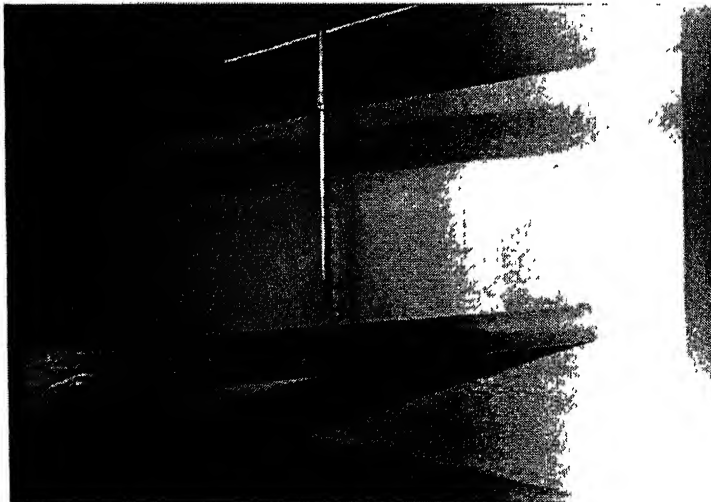


Fig. (3.8) Circular Cylinder model and the Probe

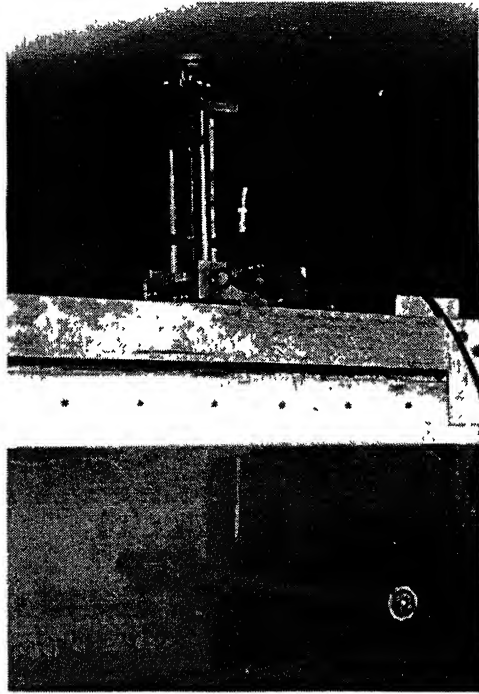


Fig. (3.9) 3-D Traversing Mechanism

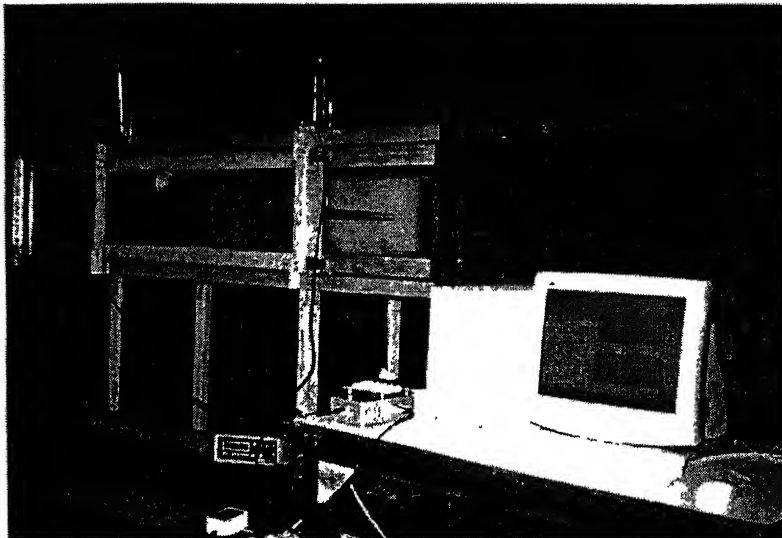


Fig. (3.10) Experimental set-up and Data acquisition P.C.

Chapter 4 RESULTS AND DISCUSSION

4.1 TEST SECTION MEASUREMENTS

The calibration of the test section speed is one of the basic requirements, once a tunnel is commissioned. A non-interference method to determine the test section speed by the wall static pressure readings at contraction cone exit wall and the settling chamber wall has been adopted in "*Low-Speed Wind Tunnel Testing*" by Pope, A. *et al.* In the present investigation, a 3 mm diameter Pitot static probe connected to Furness digital micro-manometer was positioned at 21 cm downstream of the test section inlet and 21 cm below the ceiling of the test section to measure the test section speed.

The first test was to calibrate the model wind tunnel test section speed for preset motor RPM. This calibration of the test section speed with the motor RPM was repeated a few times on different days and it was found that the test section speed remained constant for a preset motor RPM over the entire range as shown in the calibration plot shown in Fig.4.1. The flow quality in the model wind tunnel test section is good with a maximum speed of 24 m/s and lowest possible speed of 2 m/s, which could be obtained with little deviation from the mean value for a run time up to one hour continuously. The frequency controlled motor control panel can provide a wind speed resolution of up to 0.5 m/s.

Variation between results of test made in different wind tunnels at the same Reynolds number and test conditions in the past highlight the effect of the free stream turbulence level that exist in different wind tunnels during experimental studies. Hence the turbulence level of the test section is a important parameter and it was found to be around 2 % at the maximum speed in the center of the model wind tunnel test section. The velocity profile in the test section for different motor RPM and at three locations at 21 cm, 78 cm, 177 cm down stream of the test section inlet, were obtained and the corresponding graph are shown in Fig.4.2.

4.2 CIRCULAR CYLINDER

The experimental data were collected for two free stream velocities of 4 m/s and 10 m/s. Based on the kinematic viscosity of air $\nu = 15.8 \times 10^{-6} \text{ m}^2/\text{sec}$ for the diameter of the 31 cm cylinder, Reynolds number of the tests were 1×10^3 and 2×10^4 , respectively. In presenting the data, the coordinate system as shown in Fig. 4.3 has been adopted. The downstream direction is taken as the x -axis, the vertical axis as y -axis and the z -axis as the third orthogonal coordinate axis with the origin located at the center of the circular cylinder. All the distances were made non-dimensional using the circular cylinder diameter $D = 31 \text{ cm}$ as the characteristic length. West, G. S. and Apelt, C. J. (1989) found that the pressure distribution around circular cylinder varies only slightly with respect to blockage ratio. For blockage ratios of less than 6 %, the Strouhal number is independent of the blockage ratio. In the present investigation the circular cylinder model has blockage ratio of 7.3 % (marginally higher than 6 %) and hence the blockage effect has not been considered in this study.

For presentation of the data, the x stations with respect to the model are grouped into three regions; (i) wake region, (ii) model region, and (iii) upstream region, as shown in Fig. 4.3

4.2.1 wake Region (10 m/sec)

Based on the classical fluid dynamics, shedding of vorticity in the wake of a circular cylinder results in an equal circulation in the negative sense around the cylinder. This circulation changes the location of the stagnation point and in turn generates huge cyclic lift on the cylinder as well as substantial drag in case of the real fluid. The existence of circulation flows similar to this phenomenon appears in the form of fluctuating velocity around the circular cylinder, even ahead of the stagnation point in the upstream region. This is observed in the data obtained in the upstream region of the circular cylinder as shown latter.

To show the effect of Karman Vortex Street felt upstream, first the time trace and corresponding power spectra of velocity fluctuations in the wake region was studied. The power spectra of velocity fluctuations recorded the maximum magnitude of the dominant

frequency at probe location of two diameters downstream of the circular cylinder and also at one diameter location downstream in accordance with earlier suggestions by Roshko, A. (1961) this was latter confirmed by Bearman, P.W. (1965), who suggested that probe location at one diameter downstream of the model is best suited for the study of velocity fluctuations. Park, C *et al* (2000) has adopted similar method of spectral analysis using power spectra to study the effect of velocity fluctuations in wake and the effect of aspect ratio and periodic vortex shedding

The power spectra and time trace for probe position X_6Y_1 (45mm, 3mm) and X_7Y_1 (75mm, 3mm) down stream of the circular cylinder model show clear peaks at dominant frequency of 76 Hz as shown in Fig.4.4. The magnitude of the spectral peaks of the dominant frequency of 76 Hz in the wake region at point position of X_7Y_2 (75mm, 8mm) shows an increases in magnitude [Fig. 4.5(b)] and then gradually decreases to almost zero at x location two diameters downstream in the y direction as shown in the Fig.4.5. (b) to Fig. 4.5. (d). Similar pattern with increasing of height was also observed at location X_6 (45mm,) in the wake region of the circular model. This dominant frequency at 76 Hz observed in the wake region corresponds to Strouhal number of 0.23. Spectral peaks of same dominant frequency but of smaller magnitude are found all around the circular cylinder model even at upstream region, as will be shown in the next article.

4.2.2 Model Region (10 m/sec)

The power spectra and the time trace of velocity fluctuations for the circular cylinder in the model region at probe location X_3Y_1 (-18mm, 3mm), X_4Y_1 (0mm, 18mm), X_5Y_1 (18mm, 3mm) are shown in Fig.4.6. A dominant spectral peak corresponding to Strouhal number of 0.23 appears at 76 Hz for probe locations at X_3Y_1 (-18mm, 3mm), and X_4Y_1 (0mm, 18mm), and its magnitude is low compared to the wake region in Fig. 4.5. The location X_5Y_1 (18mm, 3mm) in Fig 4.6 (c) corresponding to the near stagnation point region of the circular cylinder shows some interesting feature of the flow. While the spectra shows a dominant frequency peak of 76 Hz, it shows several sub harmonics of the fundamental. The magnitude of the spectral peaks of the dominant frequency at 76 Hz decreases monotonously, and does not show any increase in magnitude as found in the wake region. The magnitude of this spectral peak corresponding to the dominant

frequency of 76 Hz dies down to almost zero at $Y = 75\text{mm}$ almost two diameters away from the model as shown in Fig.4.7 (d). However the time traces in Fig. 4.7 (d) at probe position X_4Y_5 (0mm, 75mm) still show weak vortex shedding oscillations of the dominant frequency of 76 Hz.

Power spectra and time traces shown in Fig. 4.7 show the decay of the spectral peak of the dominating frequency as the probe is moved in the y-direction at the probe location X_4 (0mm). The time trace at the position where the intensity of the spectral peak is zero has free stream velocity fluctuations similar to that of upstream region. This feature of the spectra is confirmed by the time trace on the right hand side of Fig. 4.6 (c) where fundamental harmonics is not discernible.

4.2.3 Upstream Region (10 m/sec)

Power spectra and time trace of velocity fluctuations upstream of model along the stagnation streamline at positions of X_aY_1 (-18mm, 3mm), X_bY_1 (-23mm, 3mm), X_cY_1 (-28mm, 3mm), and X_dY_1 (-38mm, 3mm) (refer Fig.4.3 for probe locations) are shown in Fig.4.8. The power spectra show single strong spectral peaks of dominant frequency at 76 Hz similar as in the case of wake and model region and it corresponds to Strouhal number of 0.23. The magnitude of the spectral peak of the dominant frequency is less compared to the model region and the peak maximum intensity appears at position X_aY_1 (-18mm, 3mm) [Fig.4.8 (a)] near the stagnation point of the circular model. Further the magnitude of spectral peak decreases as the probe position is moved away the leading edge of the circular cylinder in the upstream direction until probe position X_cY_1 (-28mm, 3mm) [Fig.4.8(c)] after which the magnitude of spectra is zero and the time trace shows the free stream velocity fluctuations with some component of vortex shedding oscillations.

Further investigation also reveals that the spectral magnitude also decreases as the probe location is moved in the y-axis direction away from the circular model. This may be due to the weak influence of the vortex shedding felt upstream. From this it is clear that the influence of the shed Karman vortices appear not only on the leeward surface but also on the windward surface of the circular cylinder. This fact indicates that the Karman vortex shedding affects fluctuations all over the flow around the circular cylinder.

4.2.4 Circular Cylinder (4 m/s)

The experiments for detecting the upstream effect of vortex shedding around the circular cylinder were repeated at a free stream wind speed of 4 m/s. The time traces and power spectra of the velocity fluctuations show results at all locations similar to the results obtained for the circular cylinder model at 10 m/s. Single strong dominant spectral peaks of the dominant frequency appear at 32 Hz for all cases at 4 m/s free stream wind speed. This dominant frequency corresponds to Strouhal number of 0.24, which appeared in all regions namely **wake region**, **model region** and **upstream region** as discussed below.

Fig. 4.9 shows the power spectra and time traces of velocity fluctuations for circular cylinder in the **wake region** at location X_6Y_1 (45mm, 3mm) and X_7Y_1 (75mm, 3mm). A single strong spectral peak of dominant frequency appears at 32 Hz for both locations at one diameter and two diameters downstream of the circular model. This indicates the onset of strong vortex shedding in the wake region for the two free stream speeds employed in the present experiments. Fig. 4.10 shows the decay of the amplitude of the spectral peaks and the time traces as the probe is moved in the vertical direction away from the circular model. This record shows similar pattern as discussed for 10 m/s location earlier in Fig.4.5 with an increase in magnitude of spectral peak at X_7Y_2 (75mm, 8mm) [Fig 4.10(a)] and gradual decrease to almost zero at a height of almost one and a half diameters [Fig 4.10(d)], where the time trace [Fig 4.10(d)] still shows a strong shedding frequency oscillations.

Similar single strong spectral peaks of the dominant frequency component appeared at 32 Hz for free stream wind speed of 4 m/s at all probe positions for the circular cylinder in the **model region** as well as **upstream region** similar to these recorded in the 10 m/s wind speed condition, but in most cases the magnitude of peaks were small. Therefore, power spectra show peaks of very low intensity, and in the present investigation their magnitude could not be determined.

Fig 4.11 shows power spectra and time traces of velocity fluctuations for the **model region** X_3Y_1 (-18mm, 3mm), X_4Y_1 (0mm, 18mm), X_5Y_1 (18mm, 3mm). Similar to the results in the 10 m/s case there are no single clear dominant peak at X_5Y_1 (18mm, 3mm) [Fig. 4.11(c)]. Again, notice the presence of sub harmonics in the power spectra in Fig. 4.11(c) corresponding to the rear stagnation region of the circular cylinder for 4 m/s free

stream wind speed, similar to the 10 m/s wind speed case in Fig 4.6 (c). The magnitude of the spectral peak weakens to zero as the probe position is moved away in the y direction away from the circular model as shown in Fig 4.12.

In the **upstream region** at probe position X_aY_1 (-18mm, 3mm) [Fig. 4.13(a)] the spectral peak of the dominating frequency is visible but is of very low magnitude. The power spectra and time trace of fluctuating velocity for the upstream region is shown in Fig.4.13. The effect of vortex shedding is weak this is evident with the presence of the single strong spectral peaks of the dominant frequency of low amplitude at position X_aY_1 (-18mm, 3mm) and at all other places upstream the magnitude is zero.

4.3 SQUARE CYLINDER

In the case of square cylinder also, the experimental data were collected for two free stream velocities of 4 m/s and 10 m/s. Based on the kinematic viscosity of air $\nu = 15.8 * 10^{-6} \text{ m}^2/\text{sec}$ for the square side dimension of the 25 cm, Reynolds number of the tests were $6.7 * 10^3$ and $1.7 * 10^4$, respectively. In presenting the data, the coordinate system that has been adopted for circular cylinder is same as shown in Fig.4.3. All the distances were non-dimensionalised using the square cylinder arm $D = 25 \text{ mm}$ as the characteristic length. For the presentation of data the same division of flow field has been followed (i) wake region, (ii) model region, and (iii) upstream region, as was followed in the circular cylinder model is adopted in this section.

4.3.1 Wake Region (10 m/sec)

Fig 4.14 shows recorded time traces and power spectra of velocity fluctuations in the wake of the square cylinder at probe position of X_6 (37mm) for different values of y coordinate. In the wake region the velocity fluctuations are sinusoidal and the spectra show single sharp spectral peak of the dominant frequency at 62 Hz which corresponds to Strouhal number of 0.15 (this is fairly high when compared to earlier experimental results). This indicates strong vortex shedding in the wake region. Further a small peak of low magnitude is also found at 120 Hz [Fig. 4.14(a)] along with the sharp peak of dominant frequency indicating doubling of frequency in the centerline of the wake as expected. The magnitude of the spectral peak first increases [Fig. 4.14 (b)] and then

decreases as the probe is moved away from the model in the y direction. The intensity of the spectral peak is almost zero at the probe location X_6Y_5 (37mm, 50mm) as shown in Fig. 4.14 (e).

4.3.2 Model Region (10 m/sec)

Fig.4.15 shows the power spectra and the time traces of velocity fluctuations for the square cylinder at probe position X_3Y_1 (-12mm, 16mm), X_4Y_1 (0mm, 16mm), X_4Y_2 (0mm, 21mm) and X_5Y_1 (12mm, 16mm) in the model region of the square cylinder. The 62 Hz frequency component of the single dominant frequency is recorded at all locations. This corresponds to the Strouhal number of 0.15, which was also observed in the wake region. The magnitude of this dominant frequency in model region is less compared to the wake region peaks at this same frequency. This indicates that the regular vortex shedding frequency components are detected in the model region also. Interestingly at probe position X_4Y_1 (0mm, 16mm), Fig. 4.15(b) does not show clearly sinusoidal peaks of any frequency but when the probe is moved further in the y direction away from the model to X_4Y_2 (0mm, 21mm) the peaks reappear at 62Hz [Fig. 4.15(c)]. Apparently the probe position X_4Y_1 (0mm, 16mm) is in the region of separated boundary layer flow where a more complex flow pattern appears to be present. Similar feature of time traces are also present in Fig. 4.15 (d) corresponding to X_5Y_1 (12mm, 16mm), which is also the region of separated boundary layer flow. Fig 4.16 shows the decay of the spectral peak of the single dominant frequency of 67 Hz and the corresponding time traces in the vertical direction as the probe position is moved away from the square model up to more than two times the square cylinder arm in the vertical direction. Similar to that of the wake region the magnitude first increases at X_5Y_2 (12mm, 21mm) [Fig 4.16(a)] and then gradually decreases to almost zero at two times the arm of the square cylinder away from the square cylinder in the vertical direction.

4.3.3 Upstream Region (10 m/sec)

62 Hz frequency, the single strong dominant frequency characteristic peak of the wake region, found in the model region is also found in the upstream region as shown in Fig. 4.17. A single strong peak of the dominating frequency at 62 Hz is found at probe position X_aY_1 (-15mm, 3mm) [Fig 4.17(a)] near the stagnation point region. It is fairly evident that the effect of vortex shedding in the wake is present upstream with the presence of this 62 Hz frequency component. The magnitude of the intensity of oscillations is less compared to the model region. The value of spectral peak of the dominant frequency decreases as the probe is moved further upstream and is recorded till probe position X_cY_1 (-25mm, 3mm) [Fig. 4.17(c)] after which it is zero showing free stream condition at X_dY_1 (-37mm, 3mm) [Fig. 4.17(d)] as the probe is moved away from the model in the upstream direction. Interestingly, the amplitude of this spectral peak of the dominant frequency increases as the probe is moved away in the vertical direction as shown in Fig. 4.18 corresponding to X_aY_2 (-15mm, 8mm) and X_aY_3 (-15mm, 13mm).

4.3.4 Square Cylinder (4m/sec)

The power spectra and time traces recorded at all locations for the square cylinder at 4 m/s show results similar to that of the square cylinder at 10 m/s. A similar single dominant spectral peak of the dominant frequency is found at 24 Hz for all locations in the three regions of consideration. This frequency corresponds to a Strouhal number of 0.15.

Fig. 4.19 shows the power spectrum and time trace of the spectral peak in the **wake region** at probe location X_6 (37mm). In addition to the strong peak of the dominating frequency at 24 Hz, another peak of small intensity 48 Hz is also found at position Y_1 (3mm) indicating doubling of shedding frequency in the centerline region. Fig 4.19 (a) and (b) show feature similar to that of the square cylinder at 10 m/s where the magnitude of the peaks first increases at location Y_3 (12mm) [Fig 4.19(b)] and then decreases to almost zero at Y_3 (50 mm) a distance of almost two times the square cylinder arm away from the cylinder in the y direction.

In the **model region** except at probe position X_4Y_1 (0mm, 16mm) [Fig. 4.20(b)] the power spectra and time traces shows spectral peaks of the dominant frequency at 24 Hz at

all other locations X_3Y_1 (12mm, 3mm) and X_5Y_1 (12mm, 3mm) as shown in Fig 4.20. Again the time traces in Fig. 20 (b) [X_4Y_1 (0mm, 16mm)] and Fig 4.20 (d) [X_5Y_1 (12mm, 16mm)] show feature of separated boundary layer flow. The decay of the spectral peak and time trace along the y direction away from the square model is shown in Fig. 4.21. However, even as far away in the y direction as two times the square model arm the vortex shedding frequency is clearly visible in the time trace of Fig. 4.21 (d).

The presence of the single dominant frequency of the spectral peak at 24 Hz in the **upstream region** and the variation of the magnitude in the upstream axial direction away from the square model is shown in Fig. 4.22 and 4.23. As in the case of circular cylinder model at test section free stream wind speed of 4 m/s, the magnitude of the single dominant spectral peak at 24 Hz corresponding to Strouhal number of 0.15 was strong enough to be picked up by the hot wire probe and it appears at probe position X_aY_1 (-15mm, 3mm) and X_bY_1 (-20mm, 3mm) [Fig. 4.22 (a) and (b)]. The magnitude decreases to zero at upstream location two times the square cylinder arm away from the model in the axial direction. Just as in the case of square cylinder at 10 m/s the magnitude of the spectral peak of the dominant frequency increases as the probe position is moved away from the centre line in the vertical direction as shown in Fig.4.23 corresponding to Y_1 of 13 mm.

4.4 TRIANGULAR CYLINDER

Spectral analyses of the velocity fluctuations around a triangular cylinder were conducted for two test section free stream wind speeds of 4m/s and 10 m/s. The corresponding Reynolds no were $6.7 * 10^3$ and $1.7 * 10^4$ respectively based on the kinematic viscosity $\nu = 15.8 * 10^{-6} \text{ m}^2/\text{sec}$ based on the triangular cylinder model base height $D = 25\text{mm}$. Co-ordinate system as adopted in the case of circular cylinder and square cylinder has been the same in the following discussion of results for triangular cylinder. For the spectral analysis, the velocity data has been presented in the same pattern as followed in the preceding cases, considering three regions (i) wake region, (ii) model region, and (iii) upstream region, as shown earlier in Fig. 4.3

4.4.1 Wake Region (10 m/sec)

Fig. 4.24 shows the power spectra and time traces of velocity fluctuations for the triangular cylinder in the wake region at probe position of X_6 (30mm). The spectral study shows similar patterns as seen earlier in the wake region of the circular cylinder and square cylinder. The presence of the single dominant spectral peak at 95 Hz corresponding to Strouhal number of 0.23 indicates the strong vortex shedding in the wake region. The magnitude of the spectral peak is maximum at X_6Y_2 (36mm, 8mm) as shown in Fig.4.24 (b) showing similarity with the other cylindrical models. The magnitude of this strong single dominant peak decreases almost to zero at Y_5 of 40 mm location almost two times the base height of the triangular cylinder as the probe is moved away from the wake centre line.

4.4.2 Model Region (10 m/sec)

Similar to the case of circular cylinder and square cylinder the peak of the dominant frequency that appeared in the wake region is also present in the model region. However, unlike in the earlier cases the magnitude of the single peak of dominant frequency is not as strong as evident in Fig 4.25. The magnitude of the single peak of dominant frequency at 95 Hz has the maximum magnitude at probe position X_5 (11mm) just at the point above separation and in addition to the peak of the dominant frequency few other peaks of smaller magnitude is also present. Again, probe location X_5Y_1 (11mm, 16mm) is the region of boundary layer separation region where the flow is more complex than the simple vortex shedding induced flow. Fig.4.26 shows the decay of power spectra and time traces of velocity fluctuations along the vertical axis as the probe is moved away from the model, due to the decrease in the influence of the vortex shedding.

4.4.3 Upstream Region (10 m/sec)

As expected, the single spectral peak at 95 Hz that corresponding to Strouhal number of 0.23 is spotted in the upstream region as well as in the wake and model region as shown in Fig. 4.27. The magnitude of this single spectral peak is weak and is maximum at probe position X_aY_1 (-14mm, 3mm) [Fig.4.27 (a)]. It is also present at position X_cY_1 (-27mm, 3mm) [Fig.4.27 (c)] but is quite weak to read its magnitude. The velocity fluctuations

reach free stream condition at X_dY_1 (-35mm, 3mm) upstream of the model as shown in Fig.4.27 (d).

4.4.4 Triangular Cylinder (4 m/sec)

The spectral analysis and time traces of velocity fluctuations for the triangular cylinder at test section speed of 4 m/s show similar results as that of 10 m/s case discussed in the previous sections, with the only difference that the magnitude of the single dominant spectral peak is considerably weak. In this case the peak frequency due to vortex shedding appears at 38 Hz that corresponds to Strouhal number of 0.23. It also appears in the upstream region as expected, however it is quite weak in amplitude for detection, but is obvious in time trace.

The **wake region** analysis of power spectra and time traces show similar results as that of the other two models as shown in Fig. 4.28. The maximum amplitude is at X_6Y_2 (36mm, 8mm) as shown in Fig.4.28 (b). Spectra and time traces of velocity fluctuations show similar pattern for the **model region** as that of triangular model at free stream test section wind speed of 10 m/s as shown in Fig.4.29 and its maximum amplitude is at X_5 (11mm) as shown in Fig.4.29 (c). The spectra and the time traces decay in the y direction to reach the free stream condition as shown in Fig. 4.30. In the spectra and time traces of velocity fluctuations for the **upstream region** the peaks of the dominant frequency are visible at locations X_aY_1 (-14mm, 3mm) and X_bY_1 (-19mm, 3mm) [Fig.4.31 (a) and (b)] and the signals are weak to read its amplitude.

4.5 MEAN VELOCITY AND RMS VELOCITY FLUCTUATIONS

The co-ordinate system as followed in the case of power spectra presentation is followed in the subsequent discussion of mean velocity and RMS fluctuations. For the presentation of data the x stations with respect to the model are grouped in to (i) wake region, (ii) model region and (iii) upstream region. All the velocities were non-dimensionalised using mean velocity or free stream velocity as the reference and all the distance were non-dimensionalised taking the diameter/ base height of the cylindrical model as the characteristic length.

4.5.1 Circular Cylinder

The mean velocity variation for the circular cylinder model for two free stream wind speeds are shown in Fig. 4.32. There is no appreciable change in mean velocity magnitude up to certain value of y of about half the diameter location in the **wake region** as shown in Fig.4.32 (a) and (b). This region is followed by large velocity gradient and velocity maximum occurs after this region, where the turbulence intensity is low. The mean velocity magnitude reaches free stream value at around two diameters away from the wake centerline.

The mean velocity in the **model region** is high at the coordinate origin location X_4 (0mm) for up to about half diameter height and the magnitude remain close to mean value, like the other probe location in the model region as shown in Fig. 4.32 (c) and (d).

Fig 4.32 (e) and (f) shows the mean velocity distribution in the **upstream region** for two test section speed conditions. The mean velocity is low just ahead of the stagnation point at location X_a (-18mm). It is low at first then increases with increase in y . At all other location there is not much variation in mean velocity along the y direction. The mean velocity which is low at the stagnation point reaches the free stream value at location X_f (-100mm) in the upstream direction.

The RMS velocity fluctuations for the circular cylinder for two test section speeds normalized with local mean velocity are shown in Fig. 4.33. The magnitude of the RMS velocity fluctuations are high in the wake center line region mainly because of low flow velocities in the wake center line as shown in Fig. 4.33 (a) and (b). The magnitude of RMS velocity fluctuations is initially high in the wake centerline then there is a gradient up to location one diameter away from the wake centerline and it decreases to very low values at location two diameters in the y direction.

The order of magnitude of RMS velocity fluctuations in the **model region** is very low compared to the wake region, for both the test section speeds, as shown in Fig. 4.33 (c) and (d). It is high close to the model then reaches the free stream value at one diameter away from the model in the y direction.

Fig. 4.33 (e) and (f) show the distribution of RMS velocity fluctuations in the **upstream region** for two different test section speeds. Just like in the model region the magnitude of RMS velocity fluctuation is small. The maximum amplitude of RMS velocity

fluctuation occurs at X_a (-18mm) and this position corresponds to location at which the spectral peak of the dominant frequency that also appear in the wake region had maximum amplitude in the upstream region. The RMS velocity fluctuation decreases along the vertical direction in that x location, for other locations X_b (-23mm), X_c (-28mm), X_d (-38mm), and X_e (-62mm), there is not much variation in the y direction but RMS velocity fluctuation decreases as one moves in the upstream direction. Free stream condition is reached at X_f (-100mm) in the upstream direction.

4.5.2 Square Cylinder

Fig.4.34 shows the mean velocity distribution in the y direction for the square cylinder model for the two test section speeds 4 m/s and 10 m/s. The mean velocity distribution in the **wake region** show similar pattern like the circular cylinder model. The magnitude of mean velocity is almost constant up to location half the base height from the wake center line and there is a gradient further till location a base height from the center line, after which it increases to free stream value at location two times the base height as shown in Fig. 4.34 (a) and (b).

In the **model region** the magnitude of mean velocity at locations X_4 (0mm) and X_5 (12mm) is low, close to the model surface, then it increases to magnitude higher than free stream value at location half the base height of the model. After which it show decrease in magnitude up to location twice the base height of the square model as shown in Fig. 4.34 (c) and (d).

The mean velocity at probe location X_3 (-12mm) show different trend, first the magnitude is higher than the mean value then it decreases to free stream condition at location twice the base height of the model as the separation would have started in the region. Just like in the circular model, the mean velocity is less in the region close to the stagnation region, up to probe location X_c (-25mm) in the **upstream direction**. In this region the mean velocity is low at first then there is an increase in magnitude with increase in height. There is no much variation in mean velocity along the y direction at other locations in the upstream region. The free stream condition is reached at X_f (-100mm) in the upstream region as shown in Fig. 4.34 (e) and 4.34 (f).

Fig. 4.35 (a) and (b) shows the RMS velocity fluctuations in the **wake region** of square cylinder model for two test section speeds. The RMS velocity fluctuation in the wake region show similar trend as in the case of circular cylinder in the wake region. In the **model region** the magnitude of the RMS velocity fluctuations are high up to the location one base height location, when compared to the other two models in this region, because in the case of square cylinder the separation occurs at the leading edge and after which the flow is turbulent and also the flow velocity is also low in this region, then it reaches free stream value at location twice the base height of the square model as shown in Fig. (c) and (d).

Fig. 4.35. (e) and (f) shows the RMS velocity fluctuations in the **upstream region**. The magnitude of the RMS velocity fluctuation is found to increase with bluntness in this region just ahead of the stagnation point. The maximum magnitude is at location X_a (-15mm) which corresponds to the point of maximum amplitude of the dominant spectral peak.

4.5.3 Triangular Cylinder

Fig. 4.36 shows the mean velocity distribution for the triangular cylinder for two test section speeds. The mean velocity distribution in the **wake region** show similar pattern as that in the case of circular and square model, in both the speed conditions as shown in Fig.4.36 (a) and (b). There is not much variation in the magnitude of the mean velocity from the free stream condition in the **model region** except at the point of separation X_5 (11mm), where it is maximum just away from the model and reaches free stream condition at location twice the base height of the triangular model as shown in Fig. 4.36 (c) and (d). The mean velocity distribution in the upstream region also show similar pattern as that of the other two models, with maximum variation from the free stream value at X_a (-14mm), which corresponds to the point of maximum intensity of spectral peak of the dominant frequency for the **upstream region** as shown in Fig. 4.36 (e) and (f). Fig. 4.37 shows the RMS velocity fluctuations for the triangular cylinder for two test section speeds. The RMS velocity fluctuation in all the regions wake, model, and the upstream regions show almost similar pattern and magnitude as that of the circular and square cylinder models discussed earlier.

4.6 DISCUSSION

The power spectra of velocity fluctuations for all the 2-D bluff body models show strong spectral peak of single dominant frequency in the **wake region**. This indicates the presence of strong vortex shedding in the **wake region** as expected. In all cases the magnitude of the spectral peak is less in the wake centerline, then it reaches the peak magnitude at around 0.5 D in the transverse direction and then decreases to very low values close to free stream condition at two diameters/ characteristic length location away from the wake center line for all the cases, where the influence of the vortex shedding is minimum.

The frequency component of the single strong spectral peak that appears in the wake region also appears in the **model region** for all the 2-D bluff body models. The magnitudes of the spectral peaks are less than in the **wake region**. This appearance of the spectral peak of the same frequency component in the **model region** corresponding to the vortex shedding in the wake region is due to the influence of the vortex shedding felt upstream even in the **model region** where the boundary layer separation would have started. For the square model at probe location X_4 (0mm) at the coordinate origin, in addition to the single strong spectral peak, other small peaks of low magnitude, which are sub-harmonics of the dominant peak, are also observed. Also the magnitude of the spectral peaks at location X_5 (12mm) is maximum as the separation of the flow would have started at the leading edge of the square model, when compared to the circular cylinder and triangular cylinder where the maximum magnitude is in the **wake region**. In the case of circular cylinder model, instead of single strong peak there are multiple peaks of at location X_5Y_1 (18mm, 3mm) just behind the model where the flow is fully turbulent. In all cases except the square cylinder the magnitude of the spectral peaks decay to free stream condition at around two diameters /characteristic length location in the transverse direction away from the model.

The spectra of velocity fluctuations of all the 2-D bluff body models in the present investigation show single dominant spectral peak at the location **upstream** of the model and the magnitude is strong enough to be traced, up to a location of X_b (-8mm) upstream after which it reaches free stream condition. The Strouhal number corresponding to the single dominant spectral peak is same as that of the Strouhal number in the wake and

model region. This indicates the effect of vortex shedding felt upstream. In the case of triangular cylinder for upstream condition the spectral peaks are observed in the power spectra but its magnitude is too weak to be recorded.

For all the models the mean velocity distribution in the wake region show similar pattern. There is no appreciable change in magnitude of mean velocity magnitude up to certain value of Y/D (in the wake region) this region is almost of constant velocity magnitude followed by a large velocity gradient and velocity maximum occurs just after this region, where the turbulence intensity is low. The magnitude of the mean velocity is low in the region just ahead of the stagnation point and it increases to local free stream value at around two diameters/ characteristic distance away in the upstream direction. There is no appreciable change in the mean velocity in the transverse direction of the upstream region for all the models.

Like the mean velocity, the magnitude of RMS velocity fluctuations are low with y then increases in the shear layer to attain maximum with further increase in y , a rapid reduction in the turbulence intensity follows for the wake region. The magnitude of the RMS fluctuation upstream of the models is very less and the maximum is at location just ahead of the model and there is no much variation in the transverse direction. The mean velocity and the RMS fluctuations in the wake region are in close agreement with the earlier findings of Sullerey, R. K. (1974).

4.6.1 Strouhal Number

As discussed earlier the Strouhal number is the same for all around a model for a particular free stream wind speed. The variation of Strouhal number with Reynolds for different 2-D bluff body models are shown in Fig. 4.38. The values of Strouhal number of the present investigation are in close agreement with the earlier experimental results, the comparison is given in the plot in Fig. 4.38. It is found that the Strouhal number for the square cylinder is low and is in good agreement with experimental results of Okajima, A. (1982).

4.6.2 U_{mean} Variation in the Model and Upstream Region

Comparison of the mean velocity distribution in the y direction at coordinate origin X_4 (0mm) in the model region show that there is not much variation in the mean velocity distribution in the case of triangular cylinder where as in the case of circular it is initially high and then reaches free stream condition at a about one diameter away in y direction. For square cylinder, initially it is low then reaches maximum at location half the base height of the square model. In all the cases it reaches free stream velocity at location almost twice the characteristic length in the y direction as shown in Fig. 4.39 (a). In the upstream region the mean velocity is low near the stagnation point and it varies with bluntness as shown in Fig. 4.39 (b). The magnitude of the mean velocity is minimum at the stagnation region for square model, but relatively high and less than free stream value for triangular model. Maximum deviation of the magnitude from the free stream value is found up to location twice the characteristic length in the upstream direction and then it attains free stream value after this location.

4.6.3 u_{rms} Variation in the Model and Upstream Region

Comparison of the RMS velocity fluctuations at the coordinate origin X_4 (0mm) in the model region and upstream region is shown in Fig. 4.40. In the model region magnitude of RMS velocity fluctuation is small, and show similar pattern for circular cylinder and triangular cylinder for both the free stream wind speeds. Whereas the magnitude of RMS velocity fluctuations are high for square cylinder at this location as the separation would have started at the square cylinder leading edge and the mean velocity is low in the separated turbulent region as shown in Fig. 4.40 (a). Also the RMS velocity fluctuation is maximum near the stagnation point in the upstream region as shown in Fig. 4.40 (b) and the variation is maximum up to a location twice the diameter/ characteristic length.

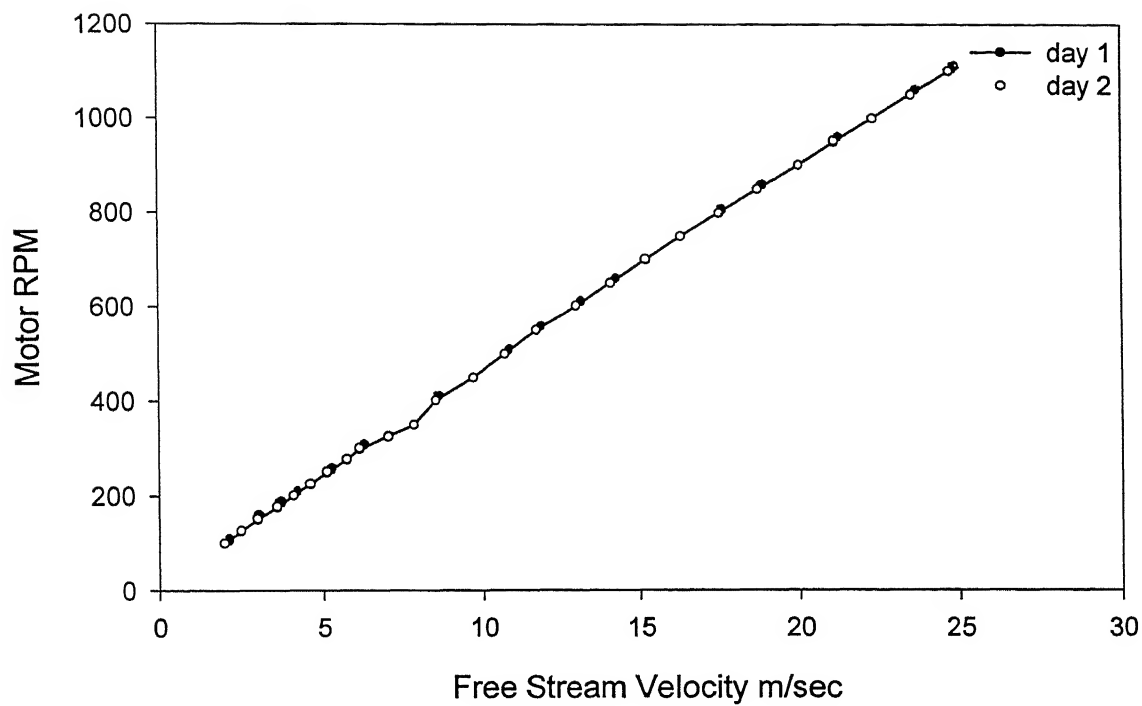
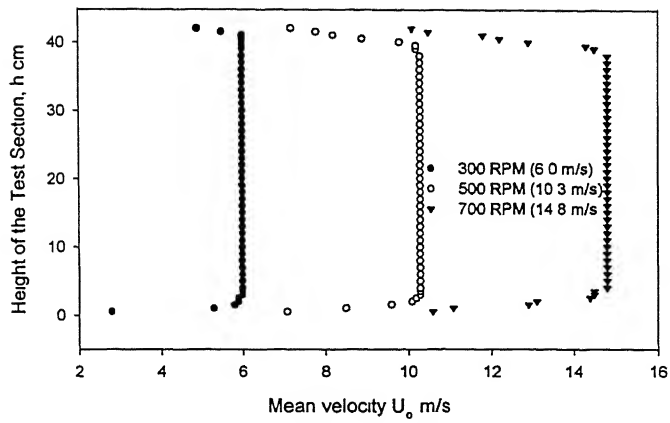
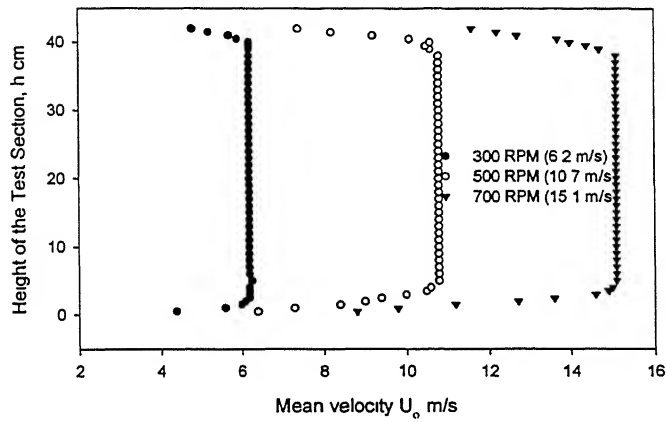


Fig.(4.1) Free Stream Velocity vs Motor RPM

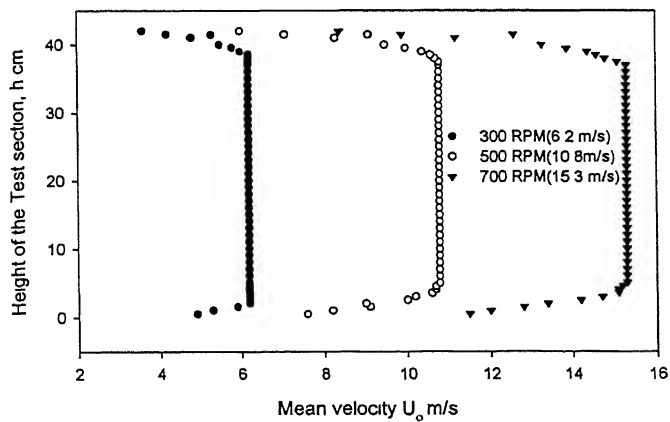


(a) Downstream of Test Section inlet 21 cm

(a) Upstream 21 cm of Test section



(b) Downstream of Test Section inlet 78 cm



(c) Downstream of Test Section inlet 177 cm

Fig. (4.2) Free Stream Velocity Profile of the Test section at Three Locations
For different Motor RPM

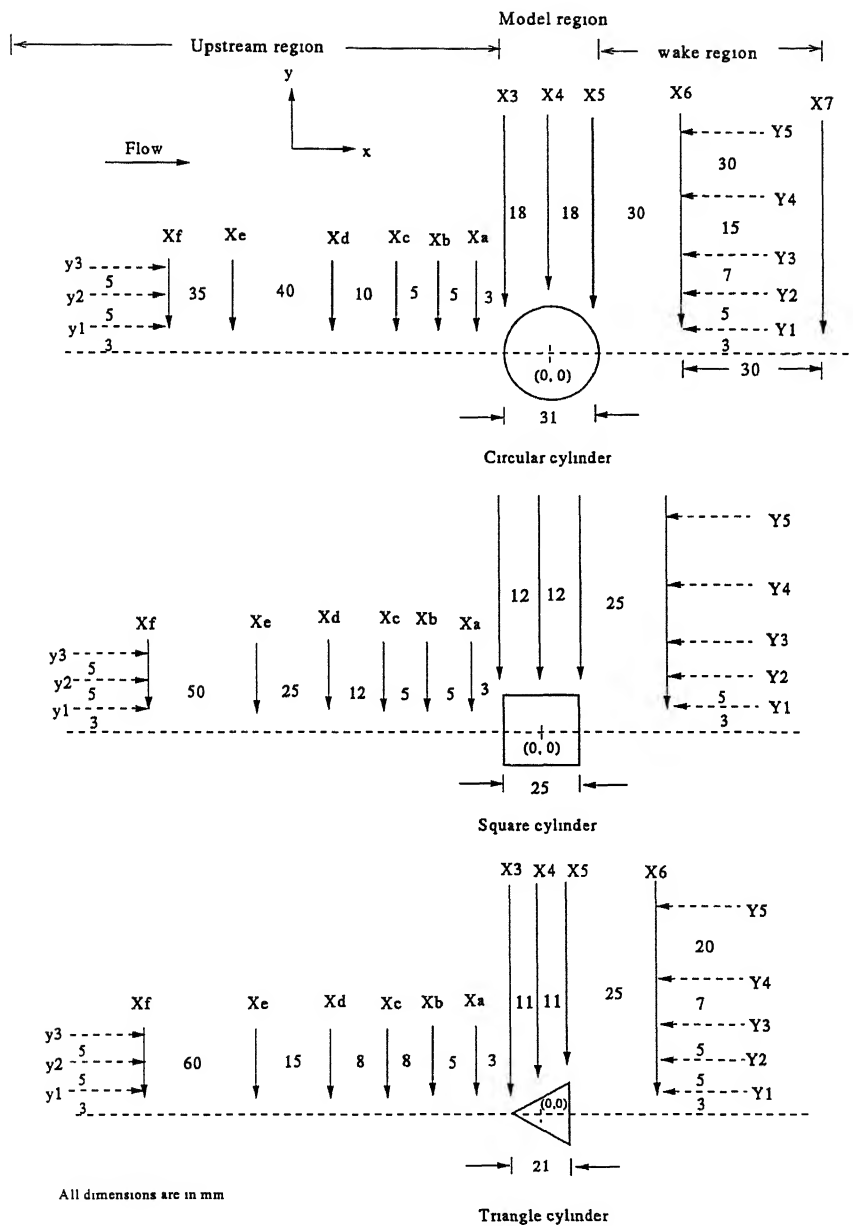
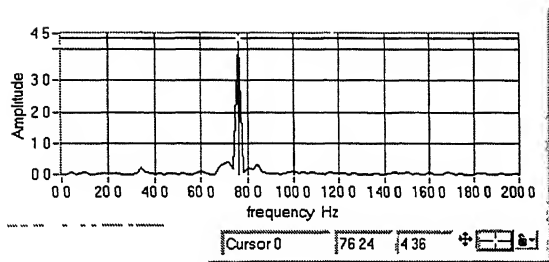
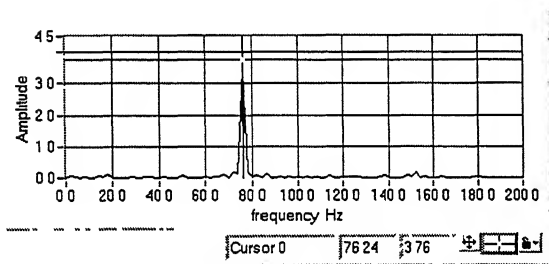
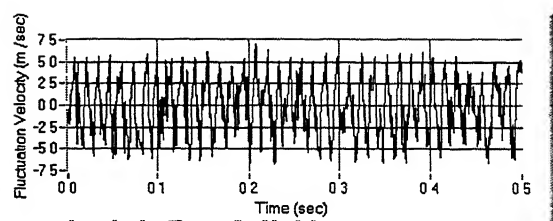


Fig (4 3) Models and Probe Locations



(a) Probe Position X_6Y_1 (45mm, 3mm)



(b) Probe Position X_7Y_1 (75mm, 3mm)

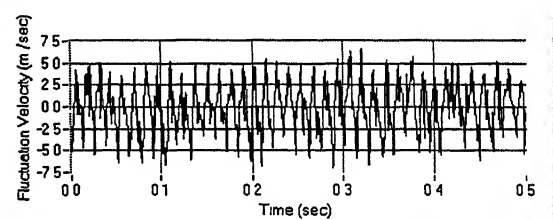
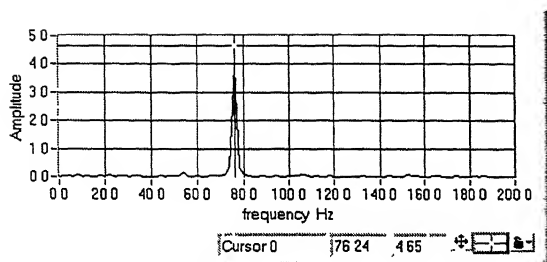
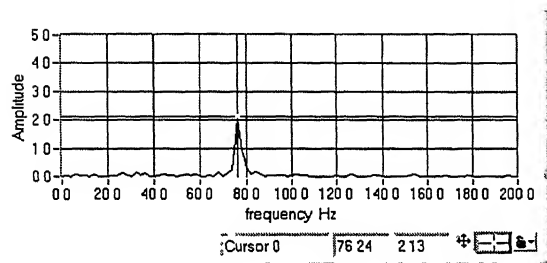
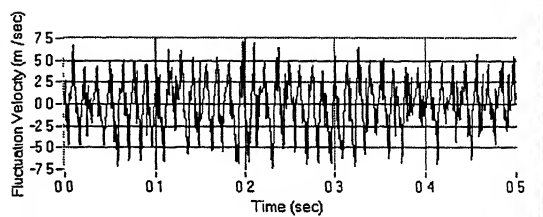


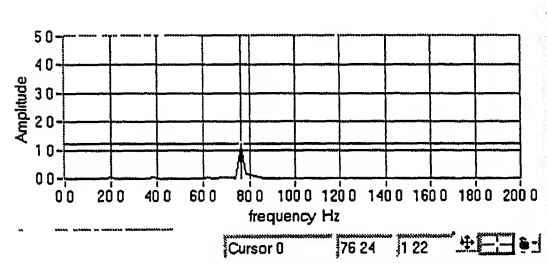
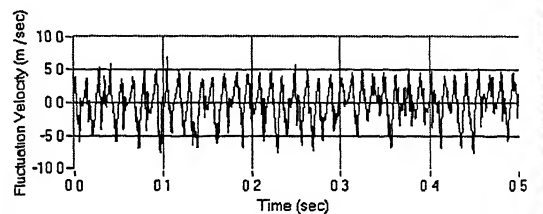
Fig. (4.4) Power spectra and time trace of velocity fluctuations for **circular cylinder**
10 m/s wake region



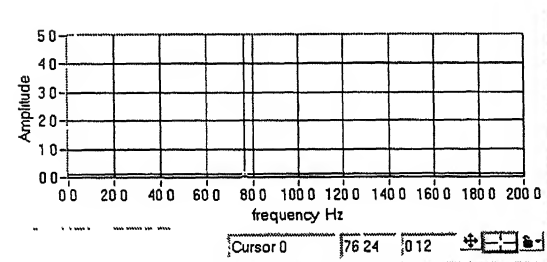
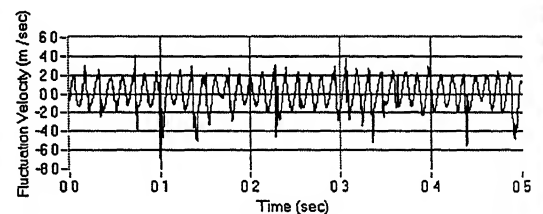
(a) Probe Position X_7Y_2 (75mm, 8mm)



(b) Probe Position X_7Y_3 (75mm, 15mm)



(c) Probe Position X_7Y_4 (75mm, 30mm)



(d) Probe Position X_7Y_5 (75mm, 60mm)

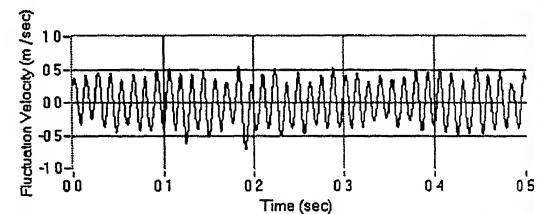
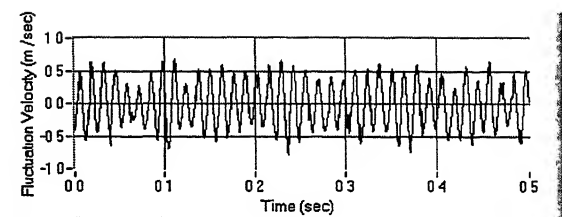
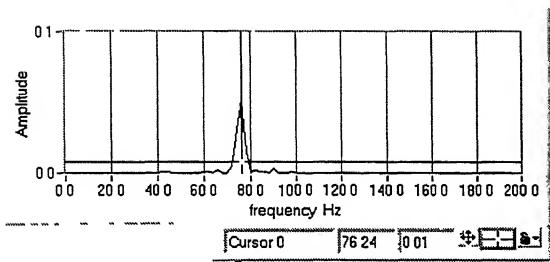
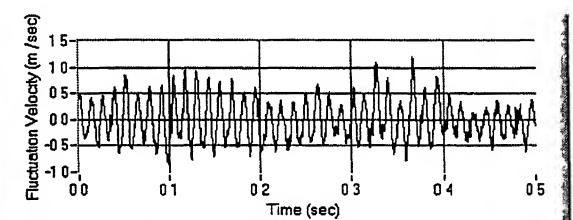
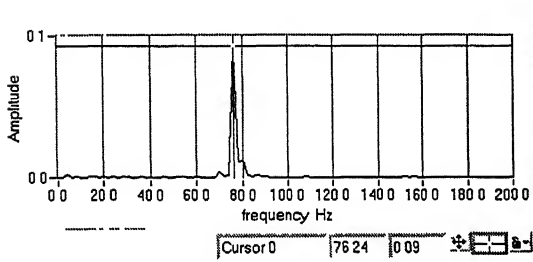


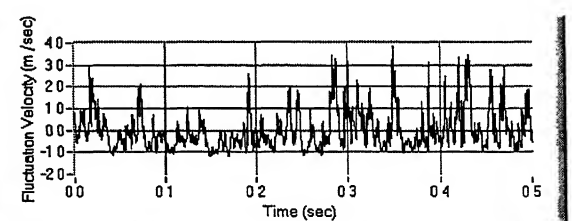
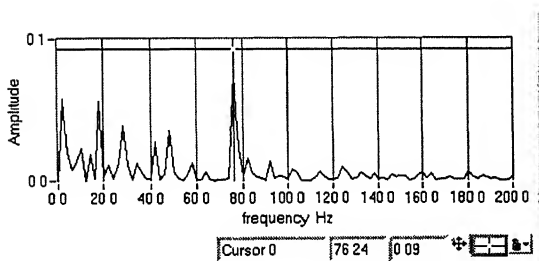
Fig. (4.5) Decay of power spectra and time trace in the vertical direction for **Circular cylinder 10 m/s wake region**



(a) Probe Position X_3Y_1 (-18mm, 3mm)

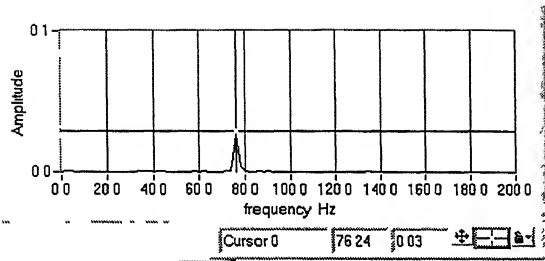


(b) Probe Position X_4Y_1 (0mm, 18mm)

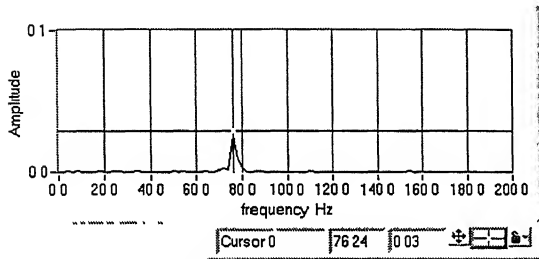
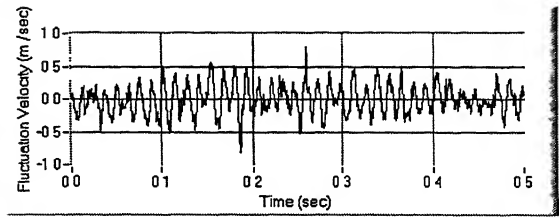


(c) Probe Position X_5Y_1 (18mm, 3mm)

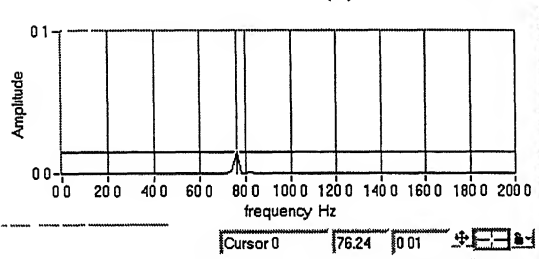
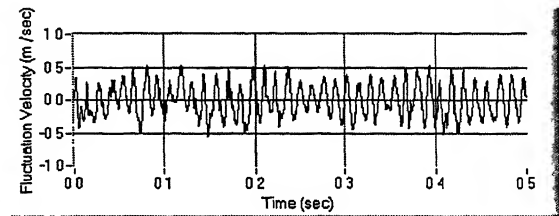
Fig. (4.6) Power spectra and time trace of velocity fluctuations for **circular cylinder**
10 m/s model region



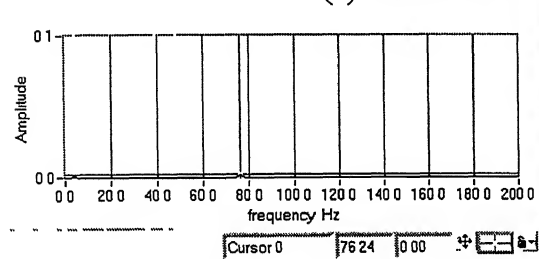
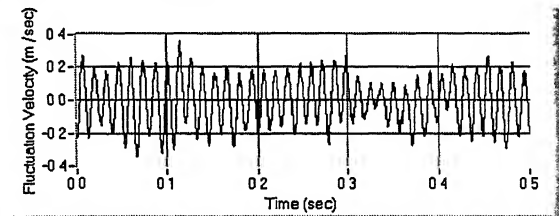
(a) Probe Position X_4Y_2 (0mm, 23mm)



(b) Probe Position X_4Y_3 (0mm, 30mm)



(c) Probe Position X_4Y_4 (0mm, 45mm)



(d) Probe Position X_4Y_5 (0mm, 75mm)

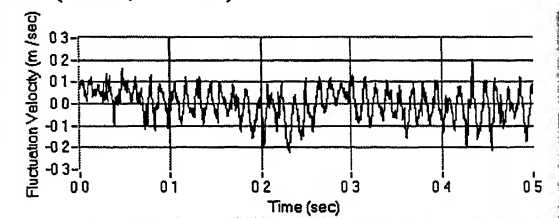
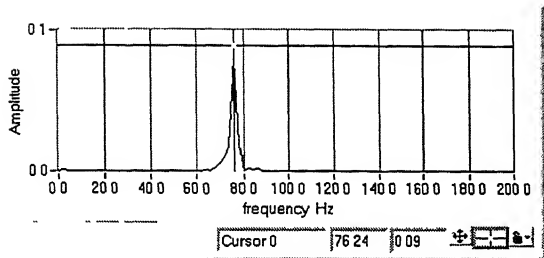
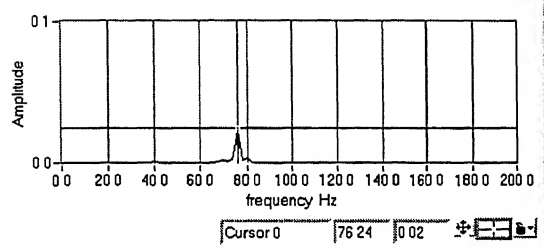
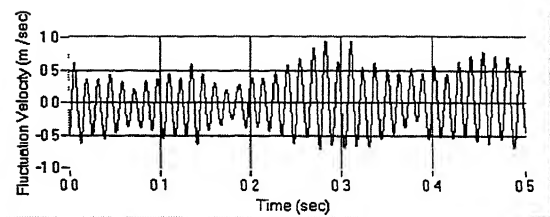


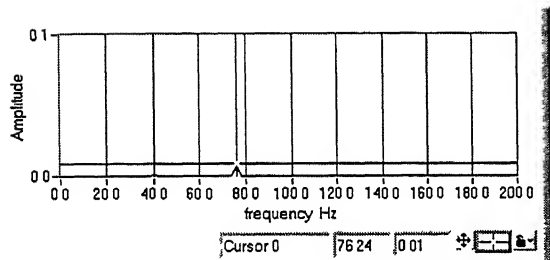
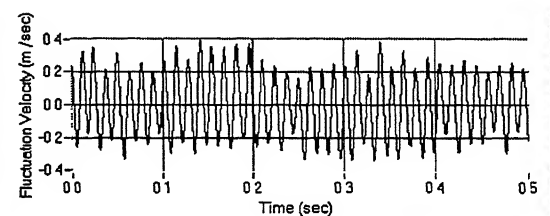
Fig. (4.7) Decay of Power spectra and time trace in the vertical direction for **Circular cylinder 10 m/s model region**



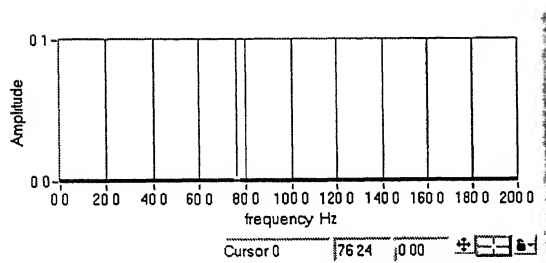
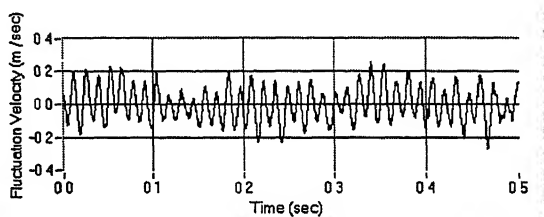
(a) Probe Position $X_a Y_1$ (-18mm, 3mm)



(b) Probe Position $X_b Y_1$ (-23mm, 3mm)



(c) Probe Position $X_c Y_1$ (-28mm, 3mm)



(d) Probe Position $X_d Y_1$ (-38mm, 3mm)

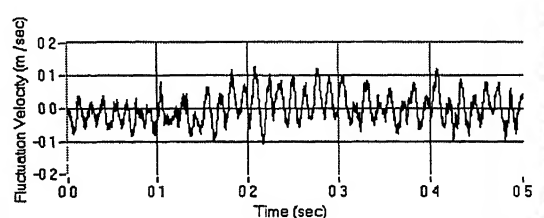
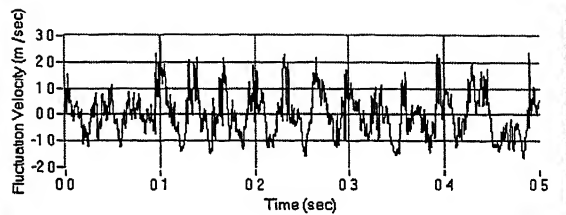
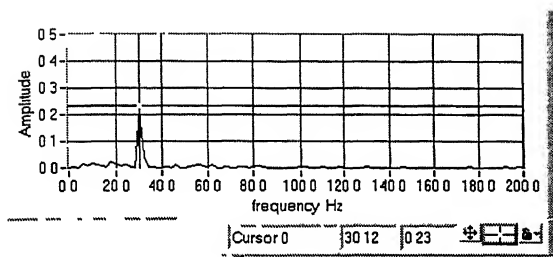
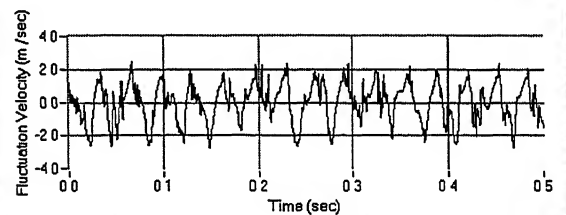
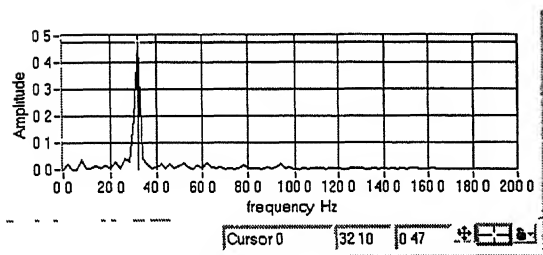


Fig. (4.8) Power spectra and time trace of velocity fluctuations for **circular cylinder**
10 m/s upstream region

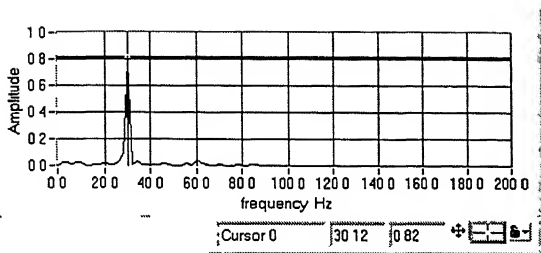


(a) Probe Position X_6Y_1 (45mm, 3mm)

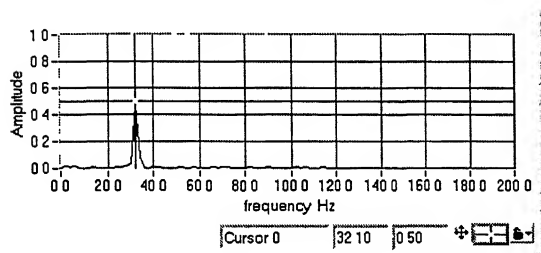
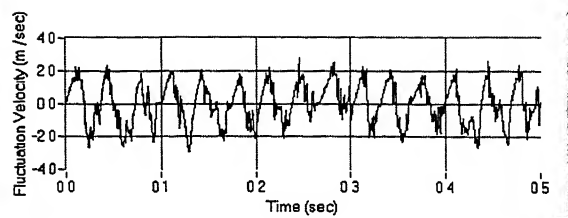


(b) Probe Position X_7Y_1 (75mm, 3mm)

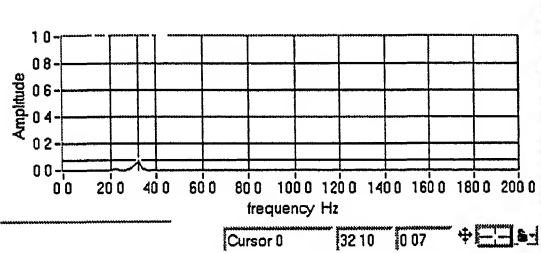
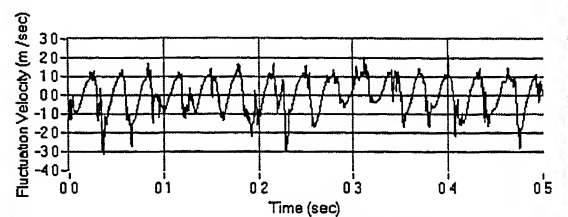
Fig. (4.9) Power spectra and time trace of velocity fluctuations for **circular cylinder**
4m/s wake region



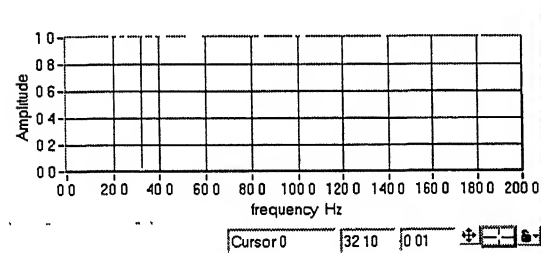
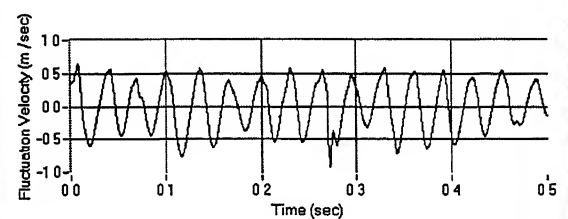
(a) Probe Position X_7Y_2 (75mm, 3mm)



(b) Probe Position X_7Y_3 (45mm, 8mm)



(c) Probe Position X_7Y_4 (45mm, 15mm)



(d) Probe Position X_7Y_5 (45mm, 30mm)

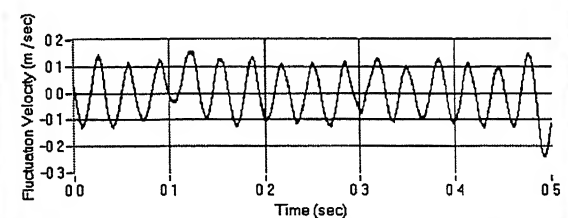
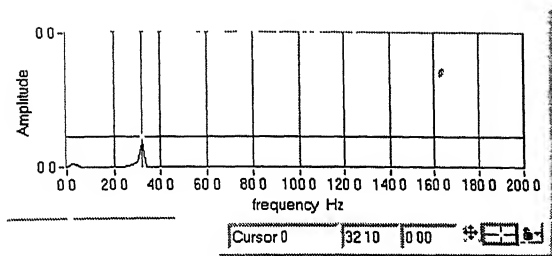
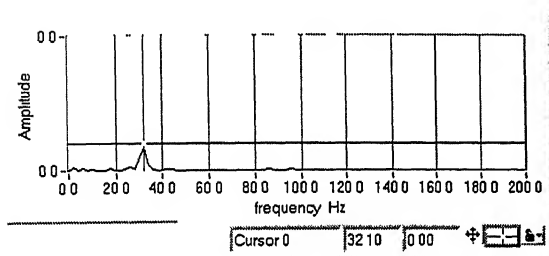
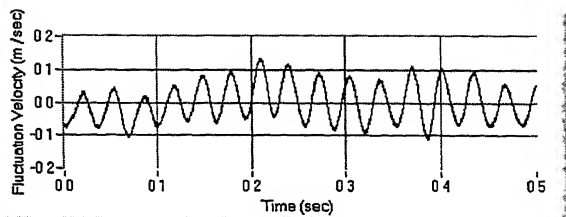


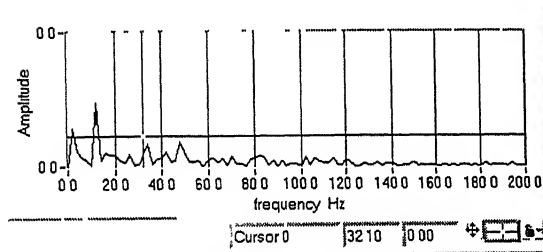
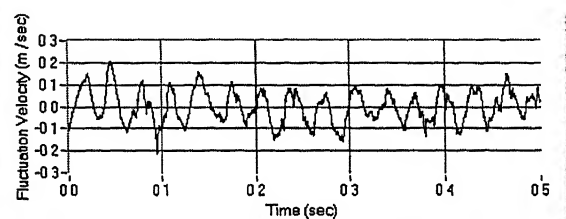
Fig. (4.10) Decay of Power spectrum and Time trace in the vertical direction
Circular cylinder 4 m/s wake region



(a) Probe Position X_3Y_1 (-18mm, 3mm)



(b) Probe Position X_4Y_1 (0mm, 3mm)



(c) Probe Position X_5Y_1 (18mm, 3mm)

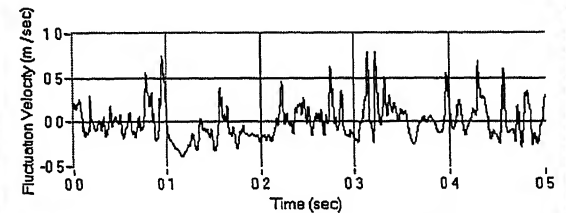
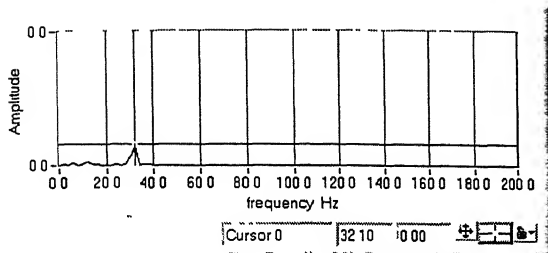
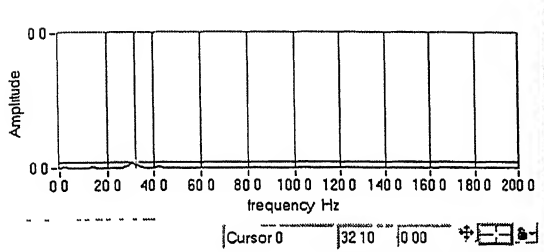
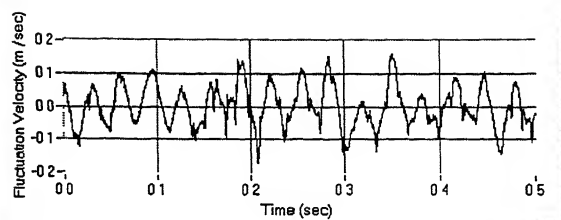


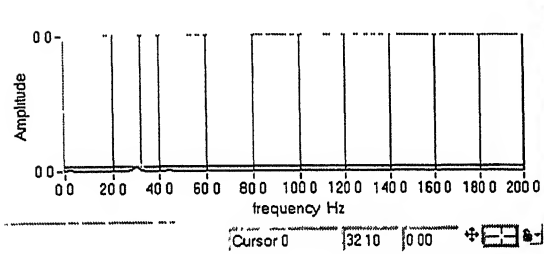
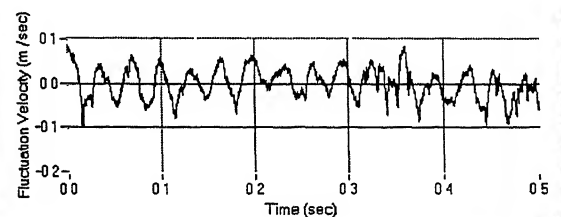
Fig. (4.11) Power spectra and time trace of velocity fluctuations for **circular cylinder** 4m/s model region



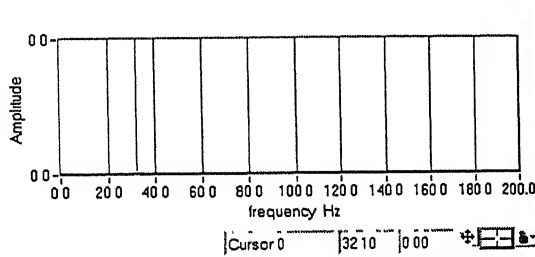
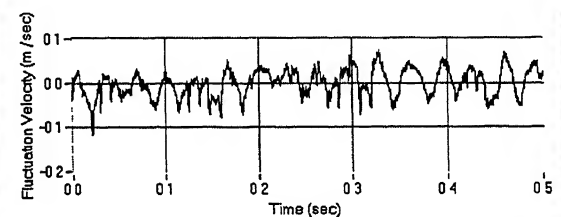
(a) Probe Position X_4Y_2 (0mm, 23mm)



(b) Probe Position X_4Y_3 (0mm, 30mm)



(c) Probe Position X_4Y_4 (0mm, 45mm)



(d) Probe Position X_4Y_5 (0mm, 75mm)

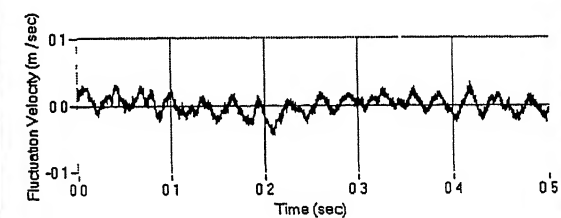
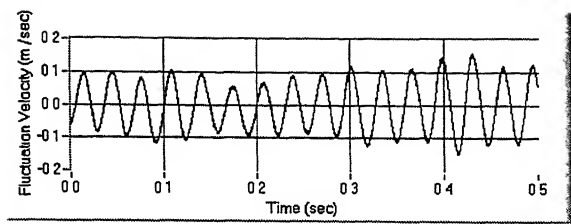
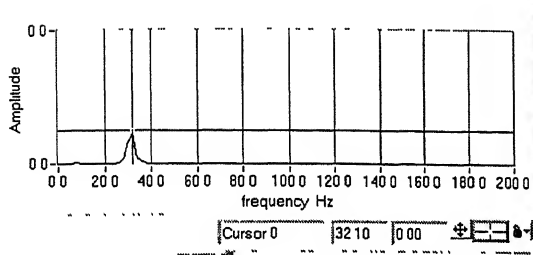
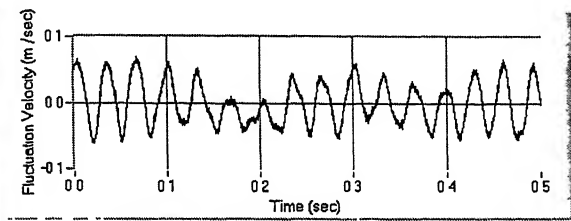
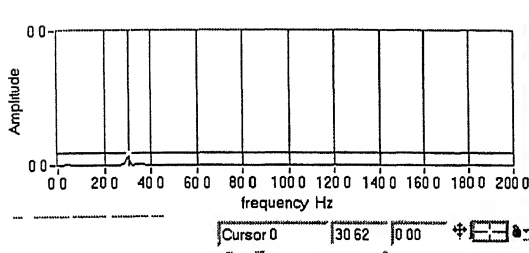


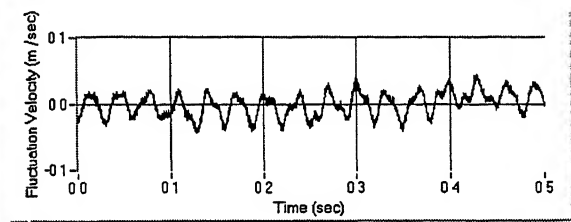
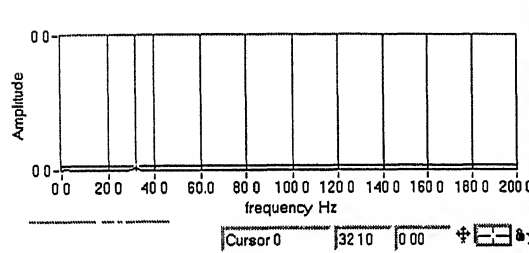
Fig. (4.12) Decay of power spectrum and time trace in the vertical direction
Circular cylinder 4 m/s model region



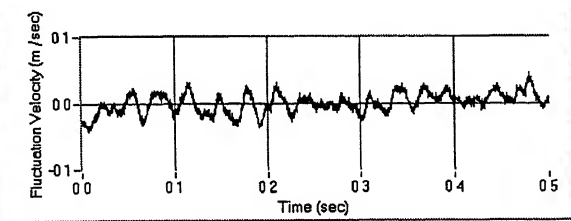
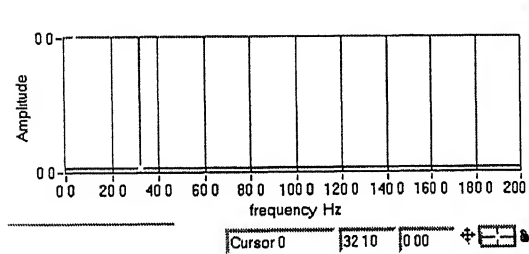
(a) Probe Position $X_a Y_1$ (-18mm, 3mm)



(b) Probe Position $X_b Y_1$ (-23mm, 3mm)

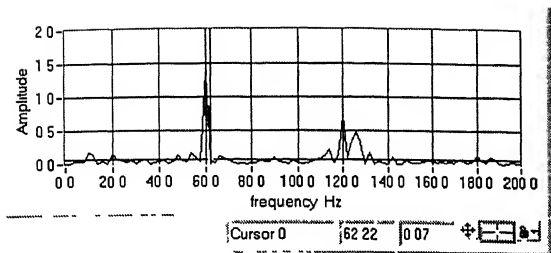


(c) Probe Position $X_c Y_1$ (-28mm, 3mm)

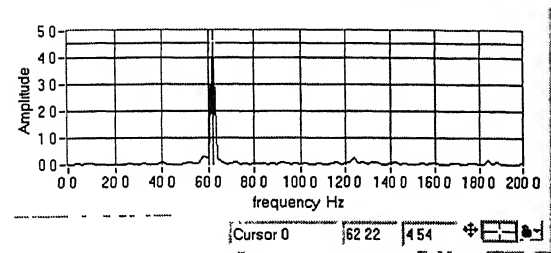
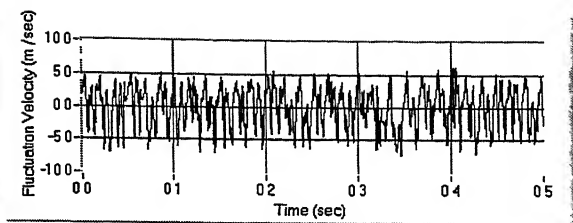


(d) Probe Position $X_d Y_1$ (-38mm, 3mm)

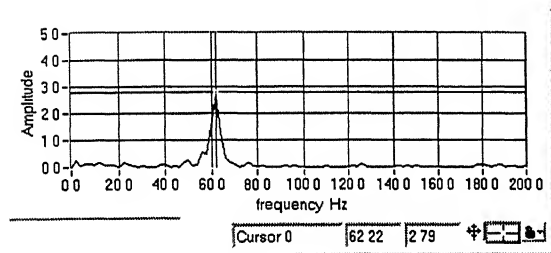
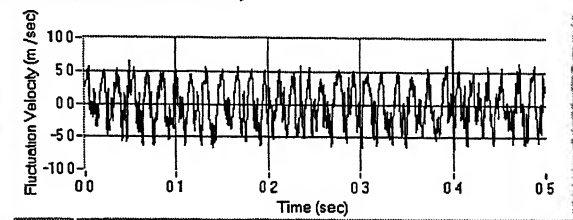
Fig. (4.13) Power spectra and time trace of velocity fluctuations for circular cylinder
4m/s upstream region



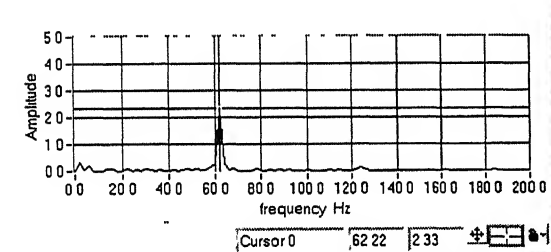
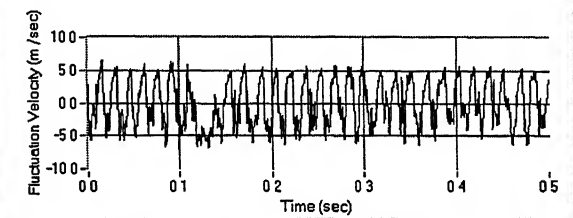
(a) Probe Position X_6Y_1 (37mm, 3mm)



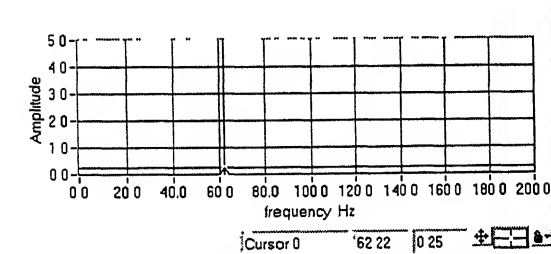
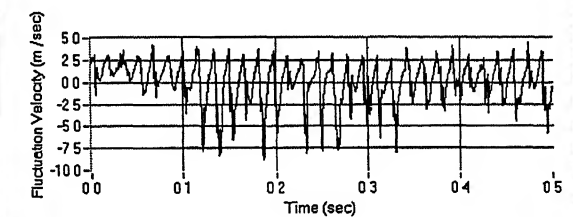
(b) Probe Position X_6Y_2 (37mm, 8mm)



(c) Probe Position X_6Y_3 (37mm, 12mm)



(d) Probe Position X_6Y_4 (37mm, 24mm)



(a) Probe Position X_6Y_5 (37mm, 50mm)

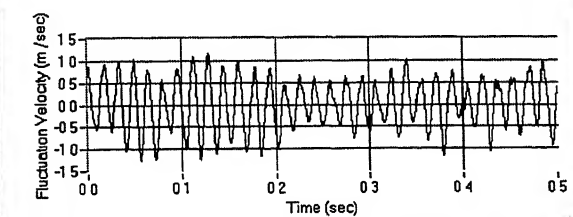
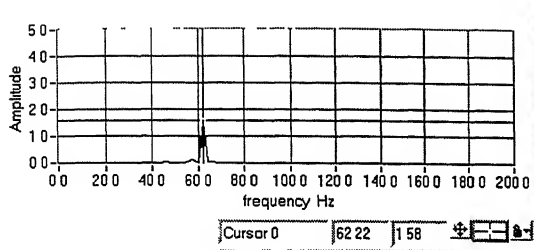
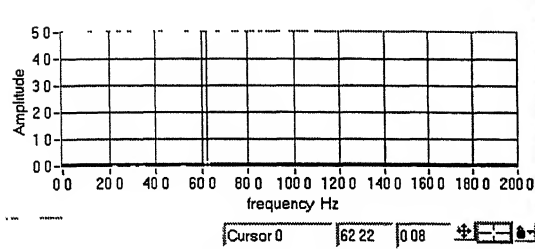
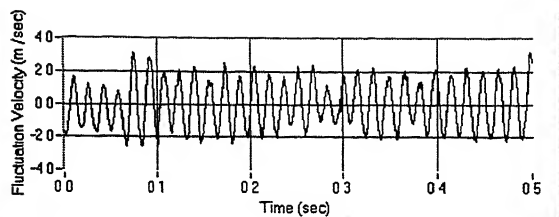


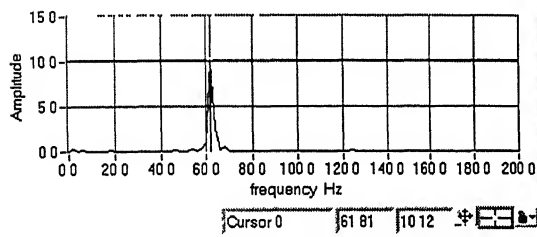
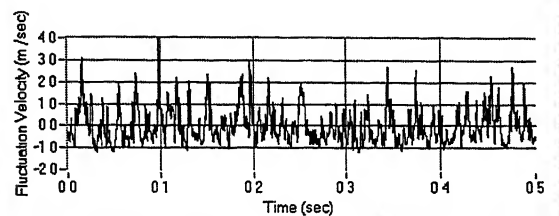
Fig. (4.14) Power spectra and time trace of velocity fluctuations for Square cylinder 10 m/s wake region



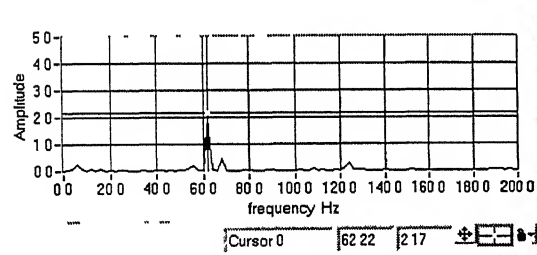
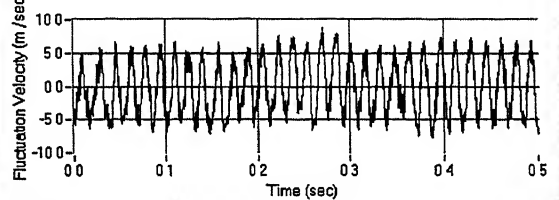
(a) Probe Position X_3Y_1 (-12mm, 16mm)



(b) Probe Position X_4Y_1 (0mm, 16mm)



(c) Probe Position X_4Y_2 (0mm, 21mm)



(d) Probe Position X_5Y_1 (12mm, 16mm)

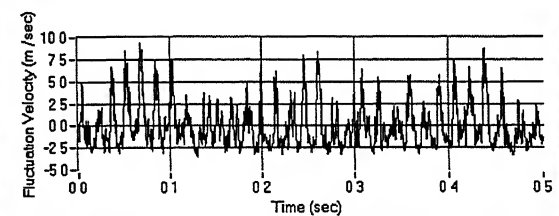
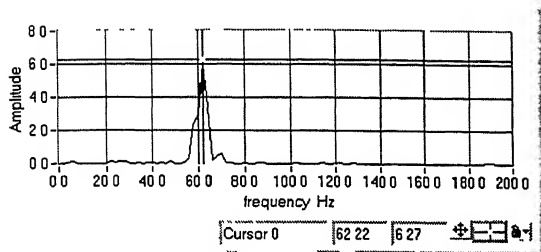
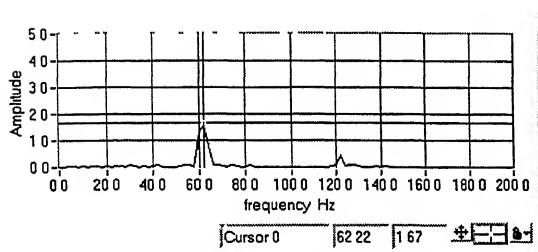
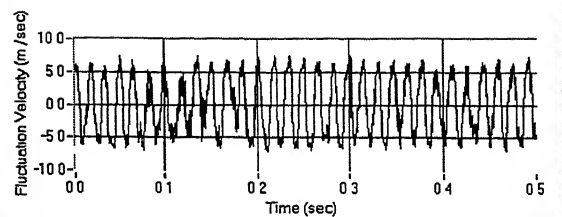


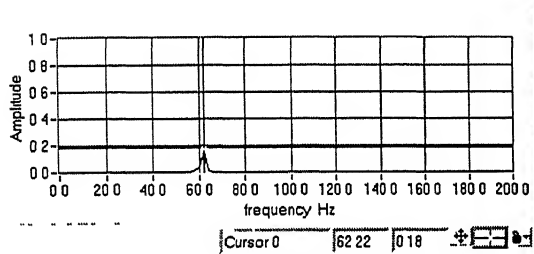
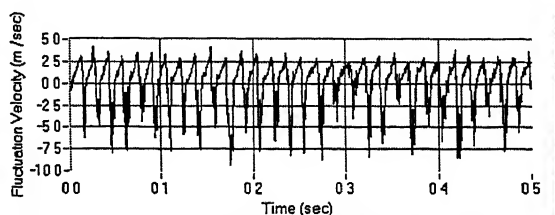
Fig. (4.15) Power spectra and time trace of velocity fluctuations for **Square cylinder**
10 m/s model region



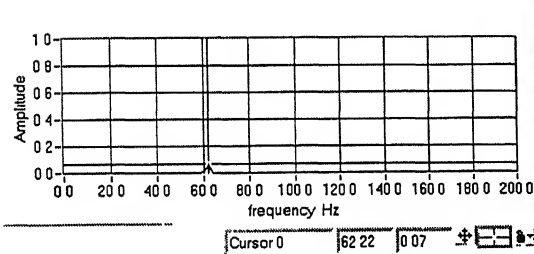
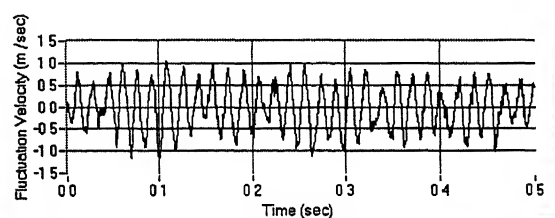
(a) Probe Position X_5Y_2 (12mm, 21mm)



(b) Probe Position X_5Y_3 (12mm, 25mm)



(c) Probe Position X_5Y_4 (12mm, 37mm)



(d) Probe Position X_5Y_5 (12mm, 53mm)

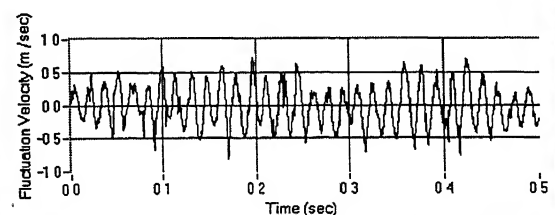
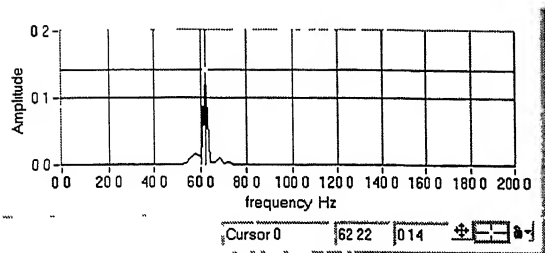
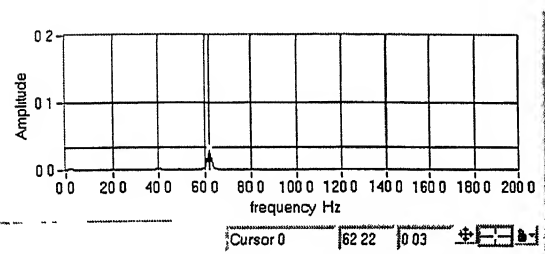
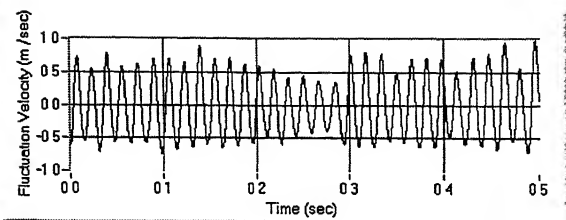


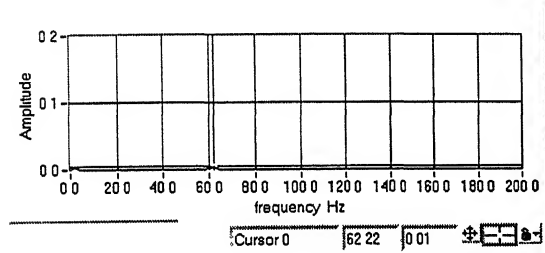
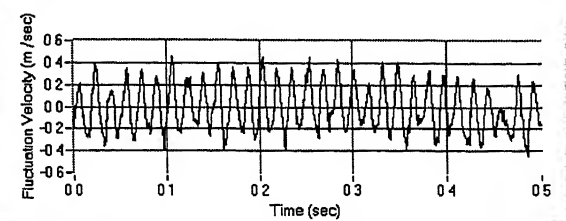
Fig. (4.16) Decay of Power spectra and time trace in the vertical direction
Square cylinder 10 m/s model region



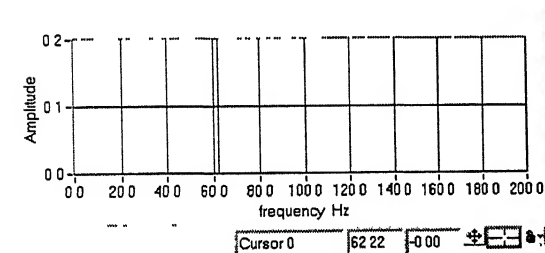
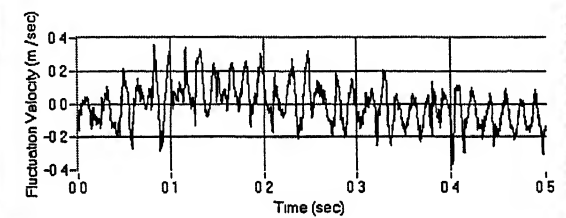
(a) Probe Position $X_a Y_1$ (-15mm, 3mm)



(b) Probe Position $X_b Y_1$ (-20mm, 3mm)



(c) Probe Position $X_c Y_1$ (-25mm, 3mm)



(d) Probe Position $X_d Y_1$ (-37mm, 3mm)

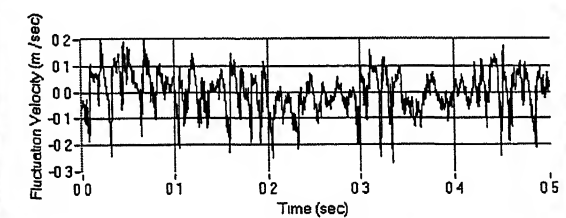
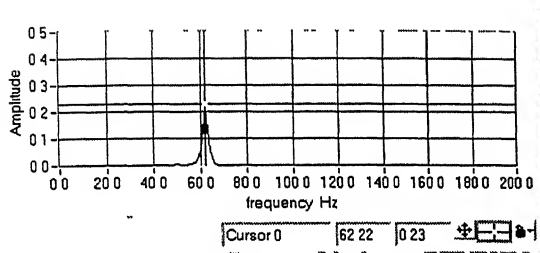
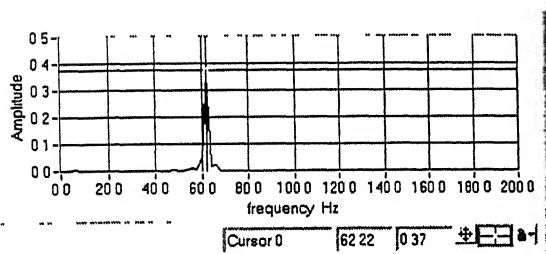
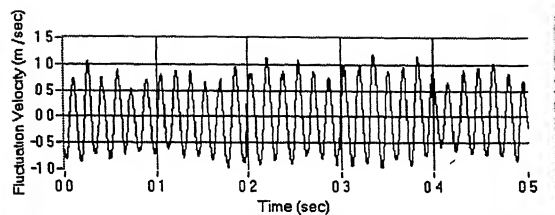


Fig. (4.17) Power spectra and time trace of velocity fluctuations for **Square cylinder**
10 m/s upstream region



(a) Probe Position $X_a Y_2$ (-15mm, 8mm)



(b) Probe Position $X_a Y_3$ (-15mm, 13mm)

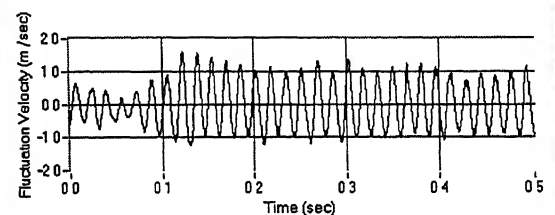
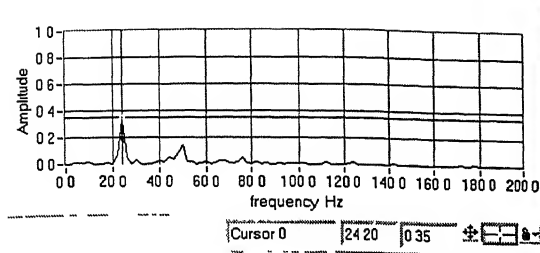
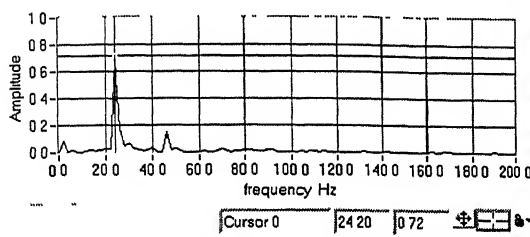
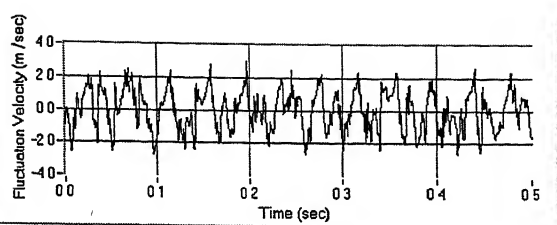


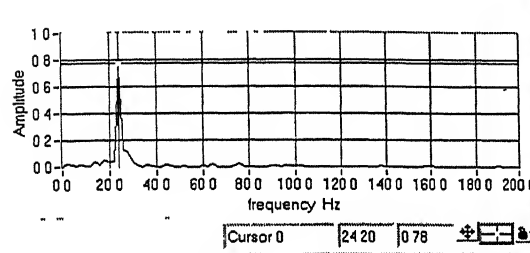
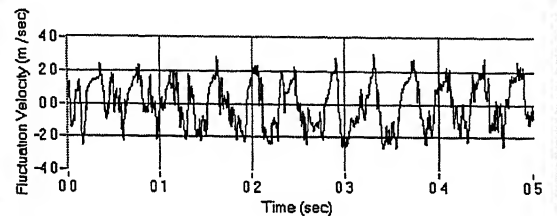
Fig. (4.18) Power spectra and Time trace of velocity fluctuations for **Square cylinder**
10 m/s **upstream region**



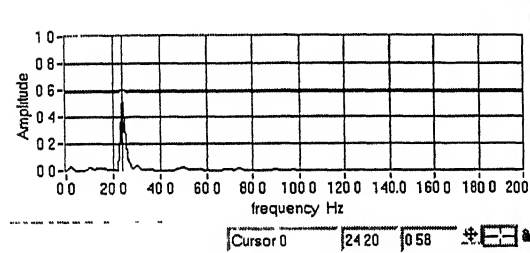
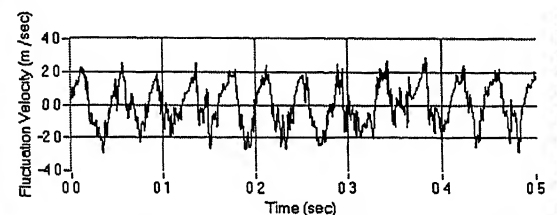
(a) Probe Position X_6Y_1 (37mm, 3mm)



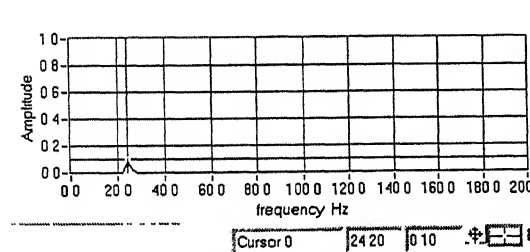
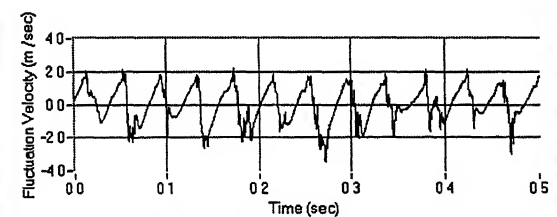
(b) Probe Position X_6Y_2 (37mm, 8mm)



(c) Probe Position X_6Y_3 (37mm, 12mm)



(d) Probe Position X_6Y_4 (37mm, 24mm)



(e) Probe Position X_6Y_5 (37mm, 50mm)

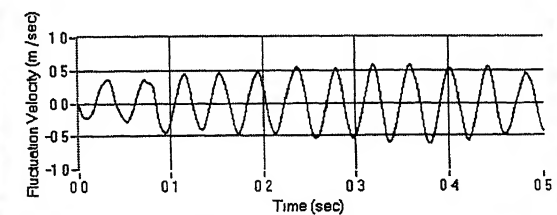


Fig. (4.19) Power spectra and time trace of velocity fluctuations for **Square cylinder** 4 m/s wake region

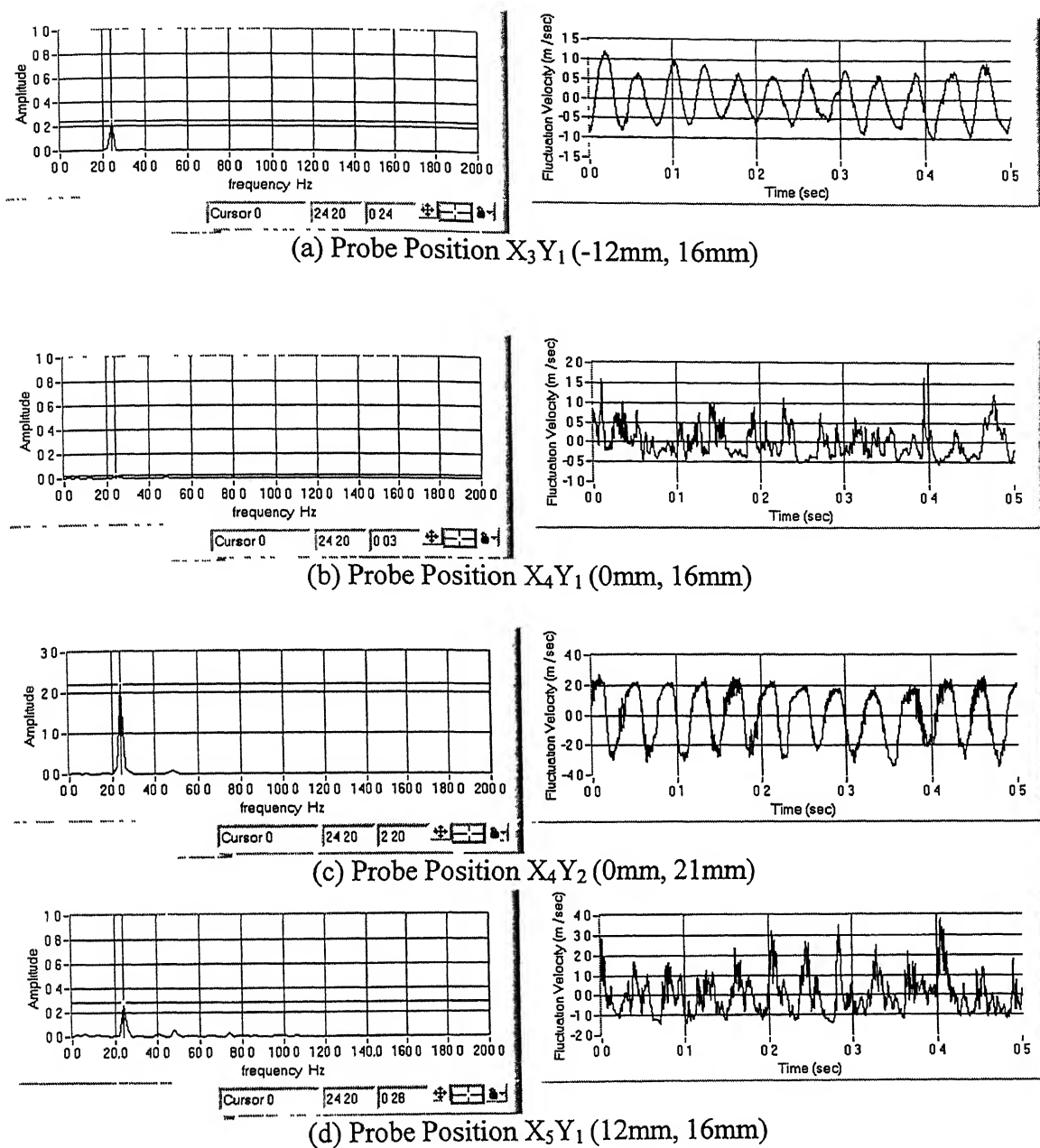
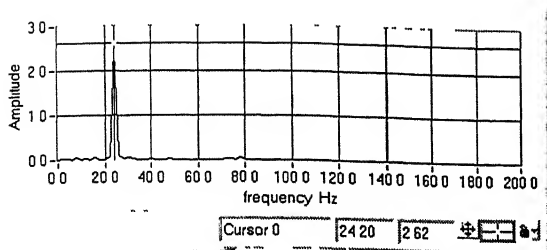
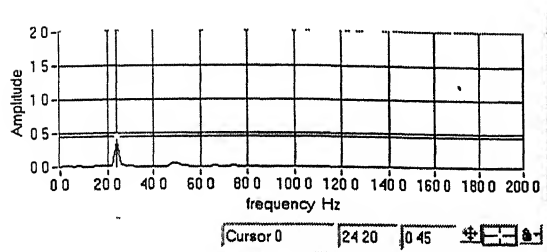
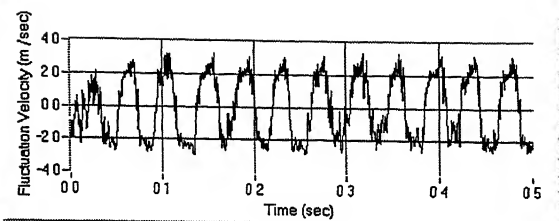


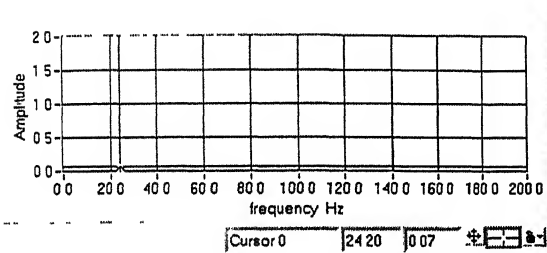
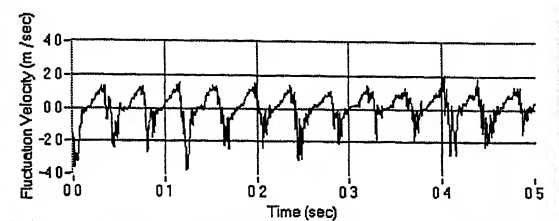
Fig. (4.20) Power spectra and Time trace of velocity fluctuations for **Square cylinder**
4 m/s model region



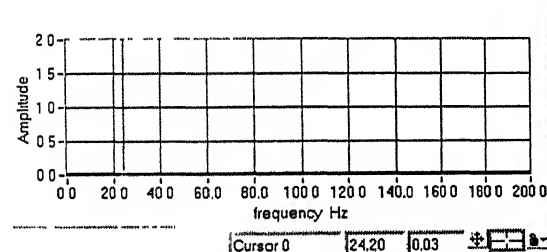
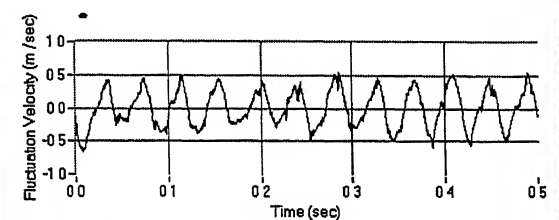
(a) Probe Position X_5Y_2 (12mm, 21mm)



(b) Probe Position X_5Y_3 (12mm, 25mm)



(c) Probe Position X_5Y_4 (12mm, 37mm)



(d) Probe Position X_5Y_5 (12mm, 53mm)

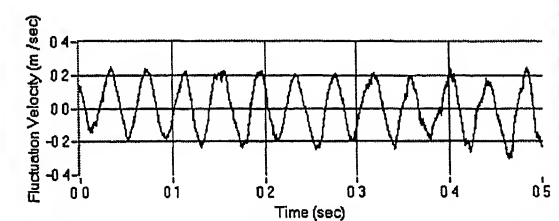
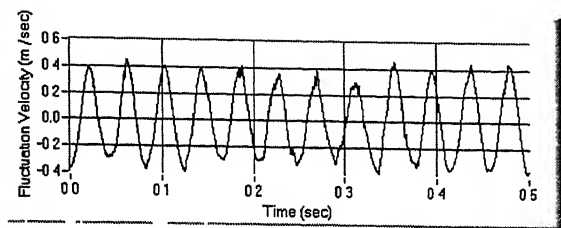
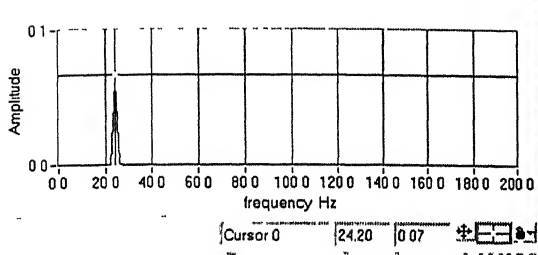
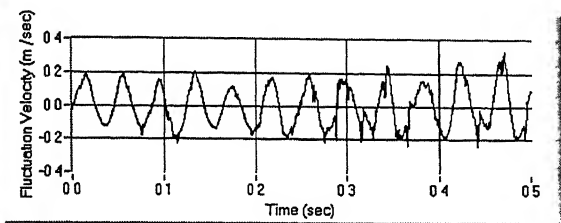
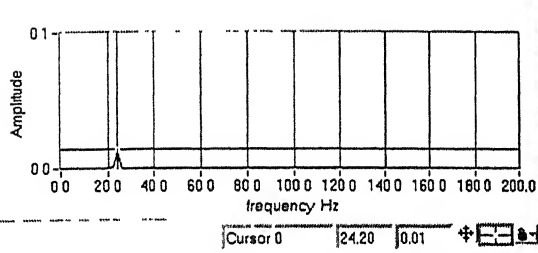


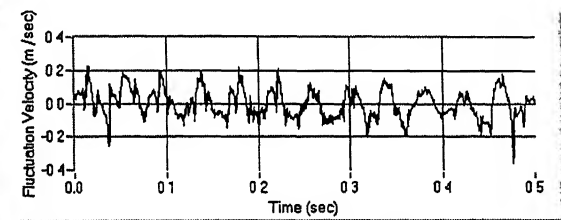
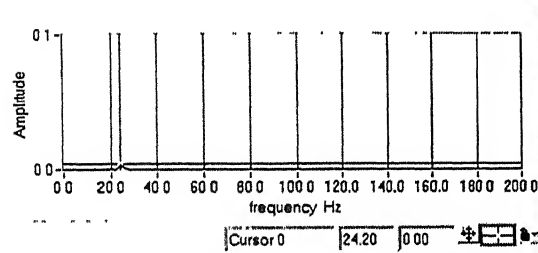
Fig. (4.21) Decay of Power spectra and time trace in the vertical direction
Square cylinder 4 m/s model region



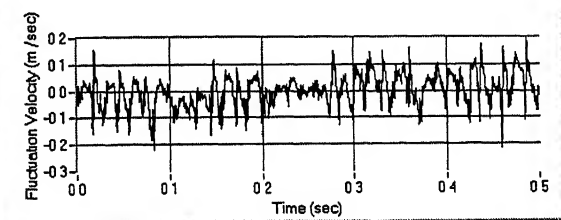
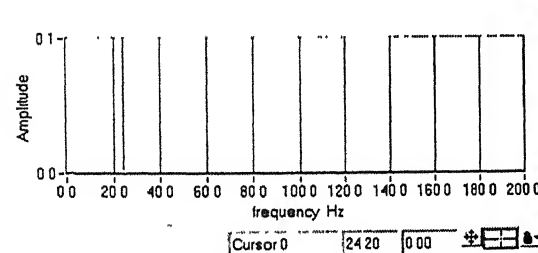
(a) Probe Position $X_a Y_1$ (-15mm, 3mm)



(b) Probe Position $X_b Y_1$ (-20mm, 3mm)

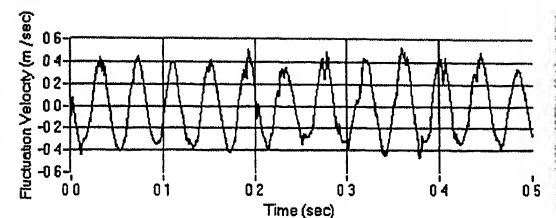
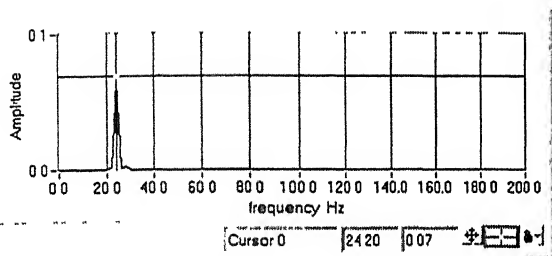


(c) Probe Position $X_c Y_1$ (-25mm, 3mm)

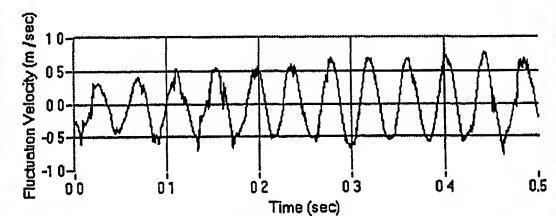
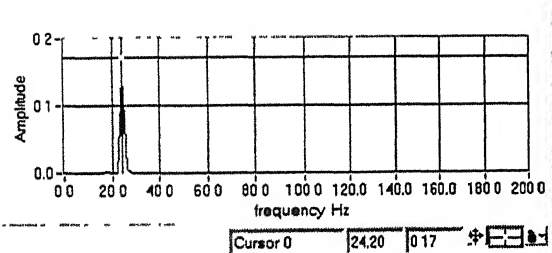


(d) Probe Position $X_d Y_1$ (-37mm, 3mm)

Fig. (4.22) Power spectra and time trace of velocity fluctuations for Square cylinder
4 m/s upstream region



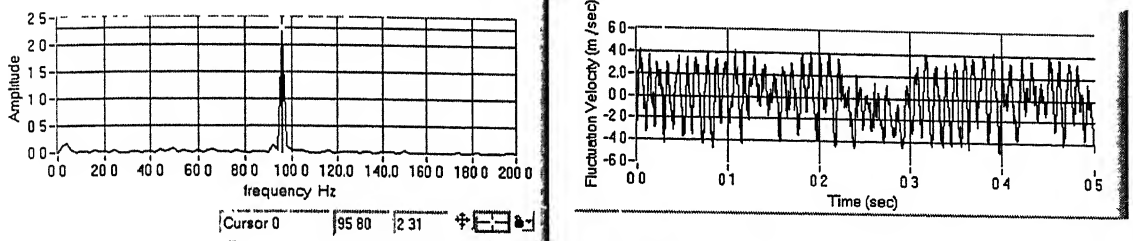
(d) Probe Position $X_a Y_2$ (-15mm, 8mm)



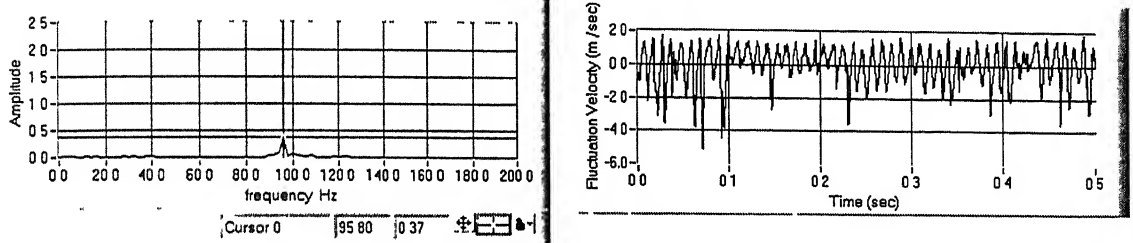
(d) Probe Position $X_a Y_1$ (-15mm, 13mm)

Fig. (4.23) Power spectra and Time trace of velocity fluctuations for **Square cylinder**
4 m/s upstream region

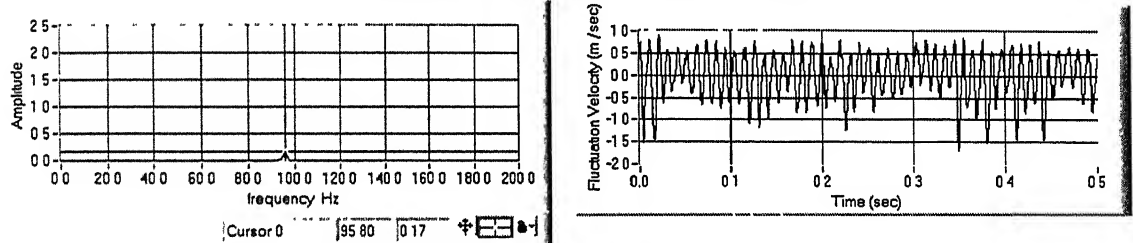
(a) Probe Position X_6Y_1 (36mm, 3mm)



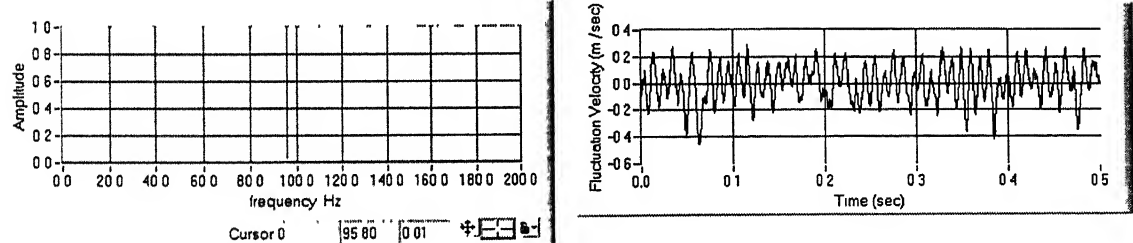
(b) Probe Position X_6Y_2 (36mm, 8mm)



(c) Probe Position X_6Y_3 (36mm, 13mm)

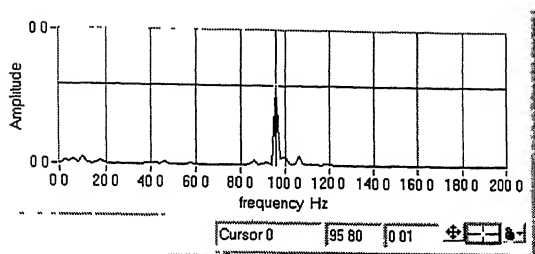


(d) Probe Position X_6Y_4 (36mm, 20mm)

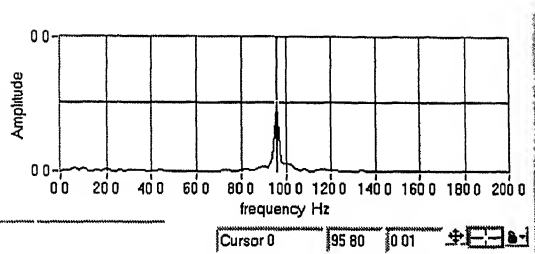
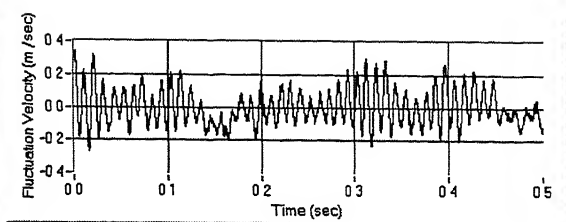


(e) Probe Position X_6Y_5 (36mm, 40mm)

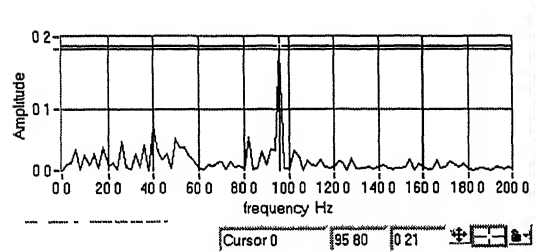
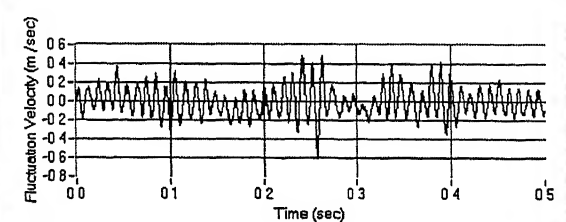
Fig. (4.24) Power spectra and Time trace of velocity fluctuations for **triangular cylinder**
10 m/s wake region



(a) Probe Position X_3Y_1 (-11mm, 3mm)



(b) Probe Position X_4Y_1 (0mm, 9mm)



(c) Probe Position X_5Y_1 (11mm, 16mm)

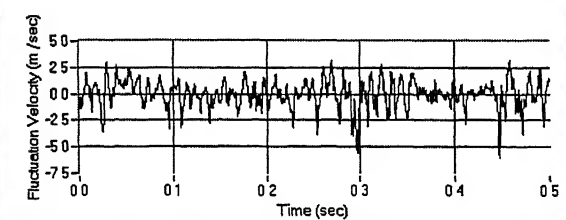
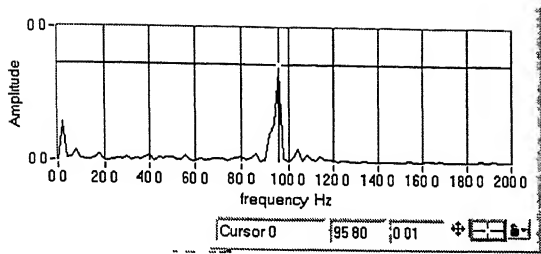
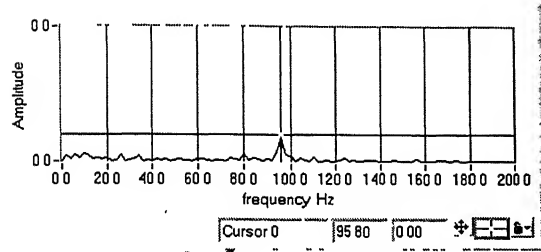
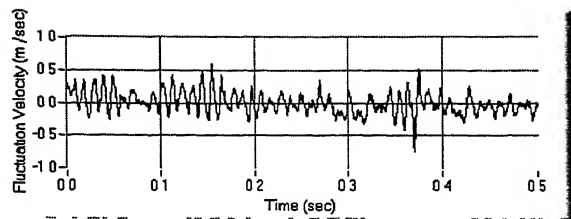


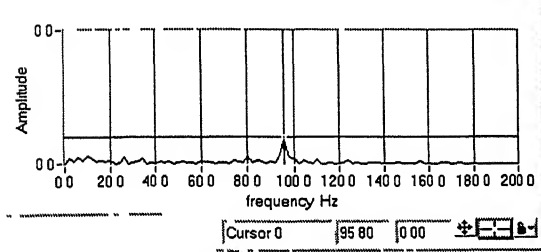
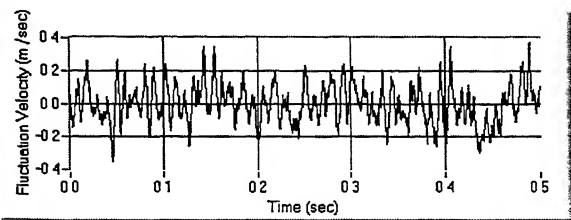
Fig. (4.25) Power spectra and time trace of velocity fluctuations for **triangular cylinder**
10 m/s **model region**



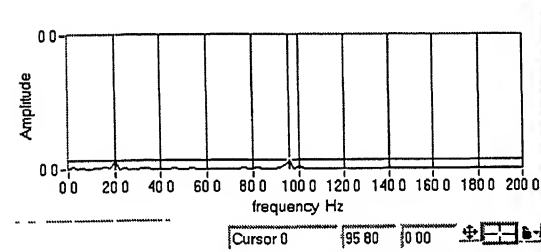
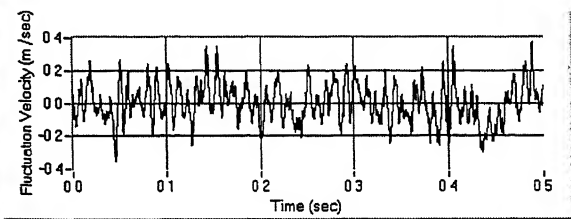
(a) Probe Position X_5Y_2 (11mm, 20mm)



(b) Probe Position X_5Y_3 (11mm, 25mm)



(c) Probe Position X_5Y_4 (11mm, 32mm)



(d) Probe Position X_5Y_5 (11mm, 52mm)

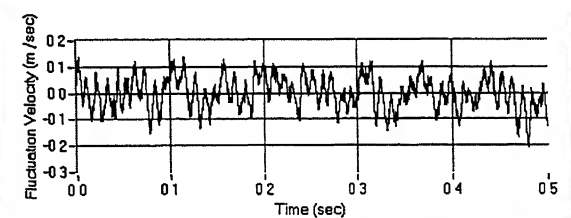
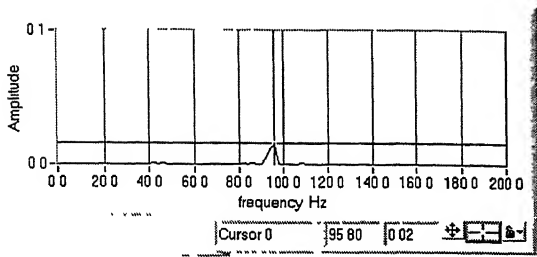
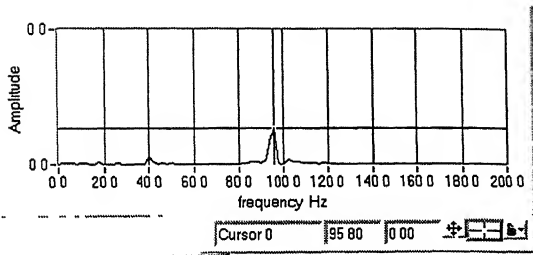
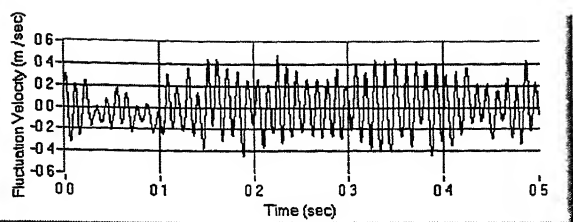


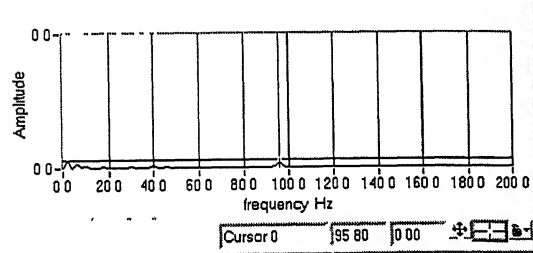
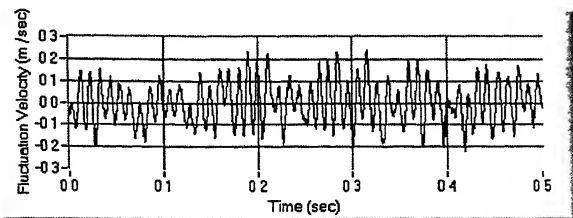
Fig. (4.26) Decay of Power spectra and Time trace in the vertical direction
Triangular cylinder 10 m/s model region



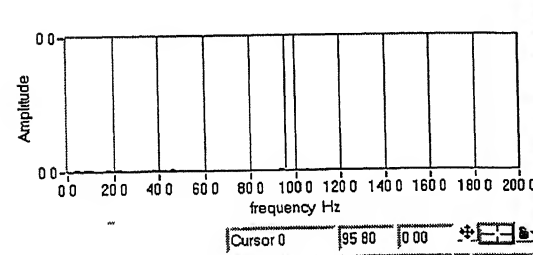
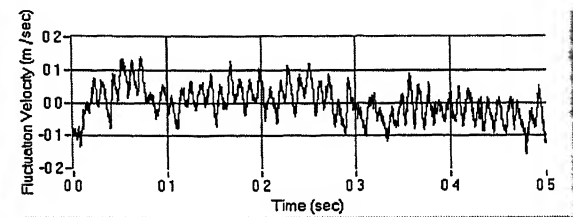
(a) Probe Position X_aY_1 (-14mm, 3mm)



(b) Probe Position X_bY_1 (-19mm, 3mm)



(c) Probe Position X_cY_1 (-27mm, 3mm)



(d) Probe Position X_dY_1 (-35mm, 3mm)

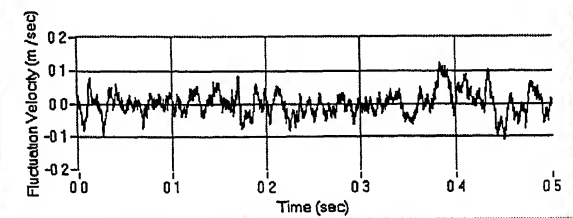
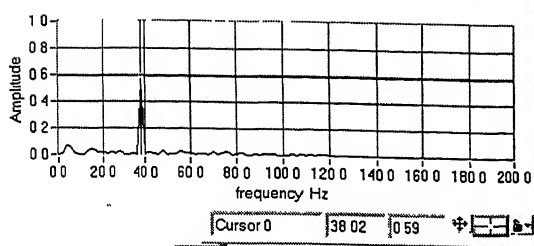
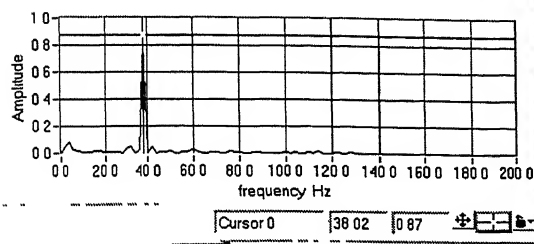
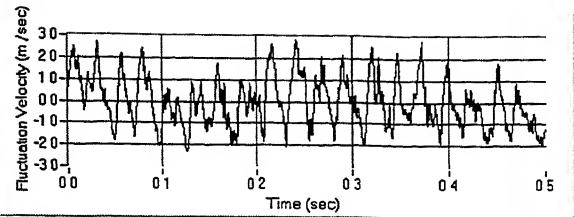


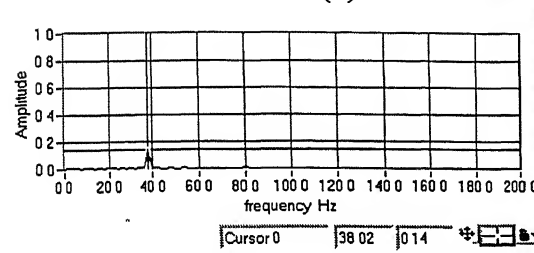
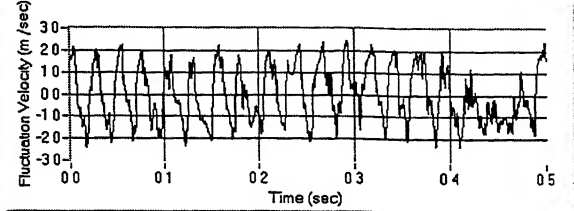
Fig. (4.27) Power spectra and Time trace of velocity fluctuations for **triangular cylinder**
10 m/s upstream region



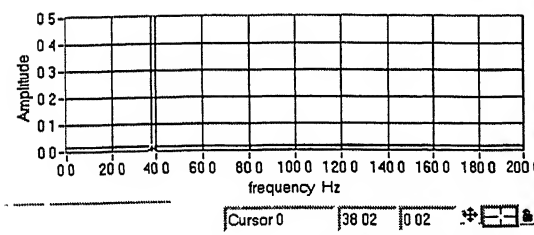
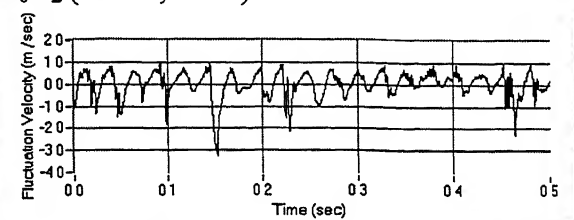
(a) Probe Position X_6Y_1 (36mm, 3mm)



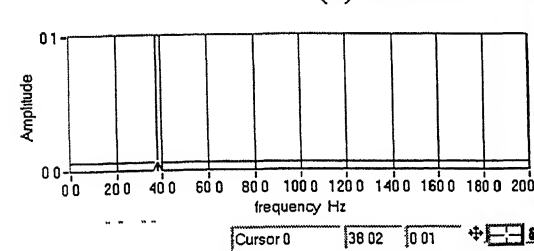
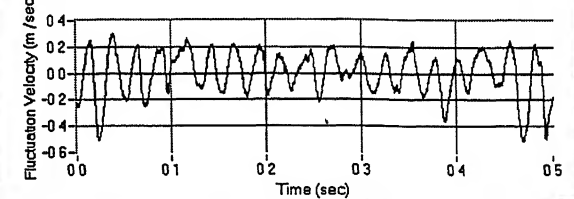
(b) Probe Position X_6Y_2 (36mm, 8mm)



(c) Probe Position X_6Y_3 (36mm, 13mm)



(d) Probe Position X_6Y_4 (36mm, 20mm)



(e) Probe Position X_6Y_5 (36mm, 40mm)

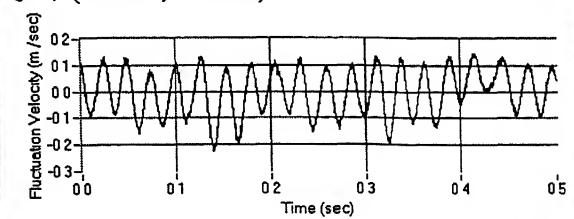
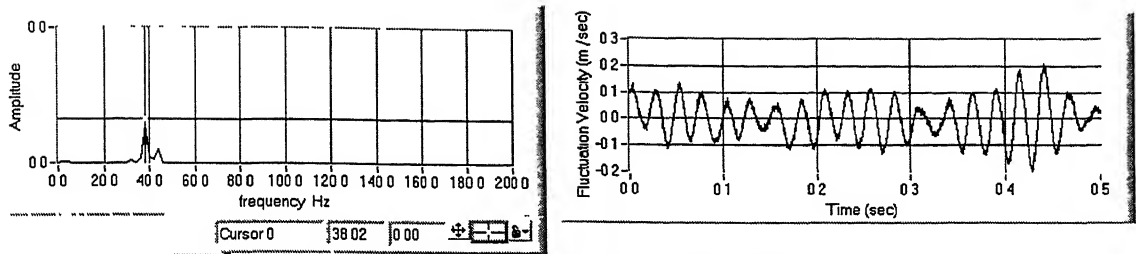
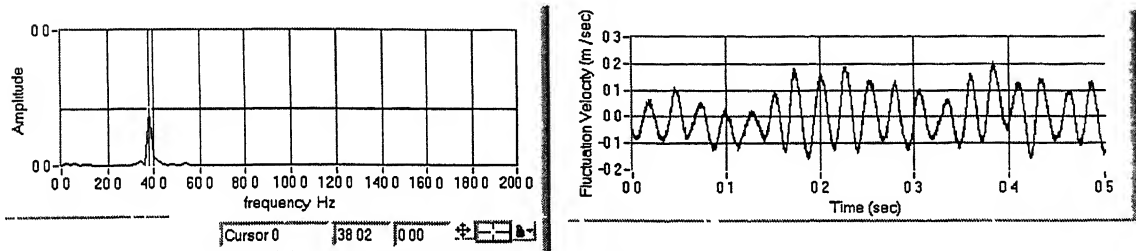


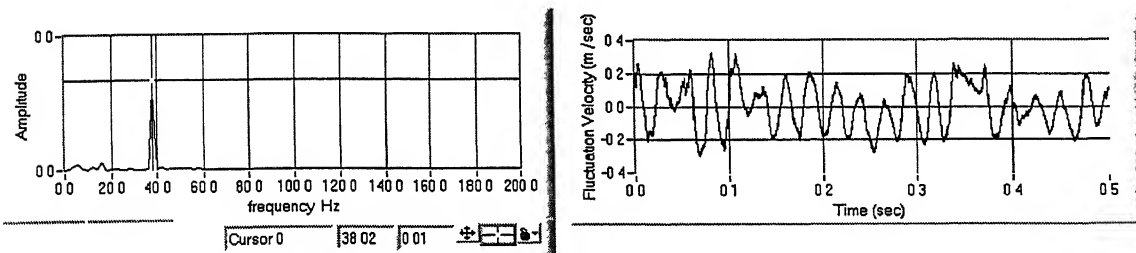
Fig. (4.28) Power spectra and Time trace of velocity fluctuations for **triangular cylinder** 4 m/s wake region



(a) Probe Position X_3Y_1 (-11mm, 3mm)

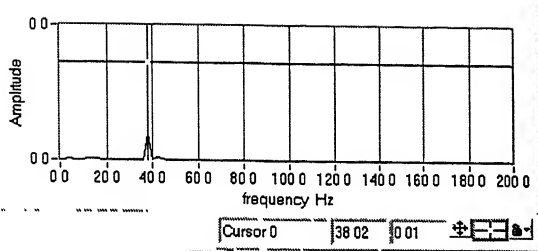


(b) Probe Position X_4Y_1 (0mm, 9mm)

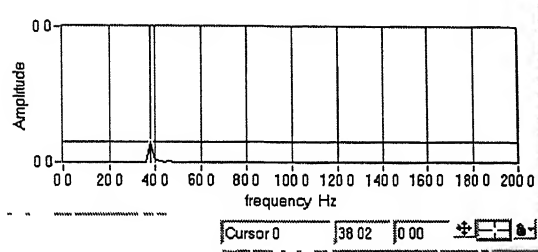
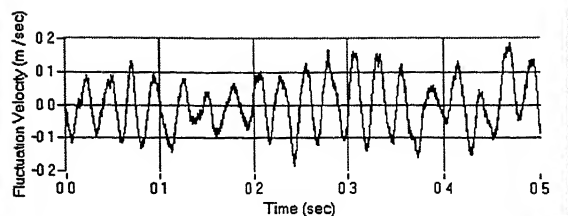


(c) Probe Position X_5Y_1 (11mm, 16mm)

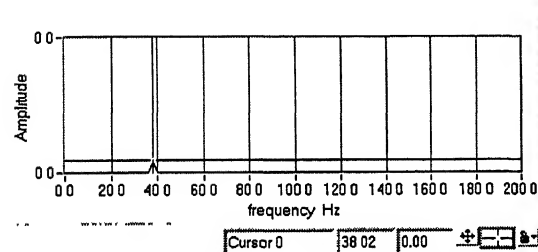
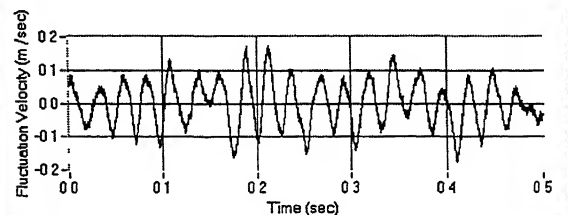
Fig. (4.29) Power spectra and time trace of velocity fluctuations for **triangular cylinder**
4 m/s **model region**



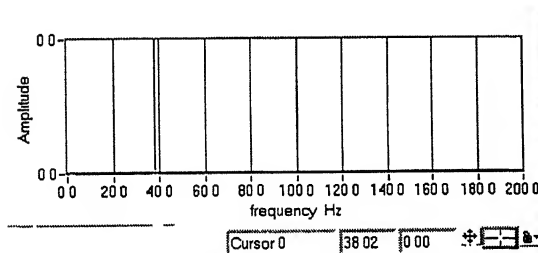
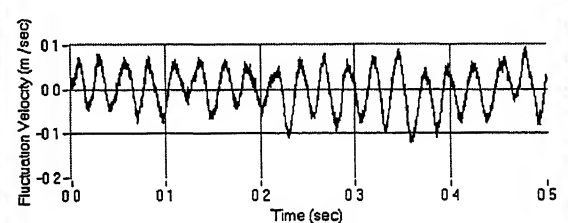
(a) Probe Position X_5Y_2 (11mm, 20mm)



(b) Probe Position X_5Y_3 (11mm, 25mm)



(c) Probe Position X_5Y_4 (11mm, 32mm)



(d) Probe Position X_5Y_5 (11mm, 50mm)

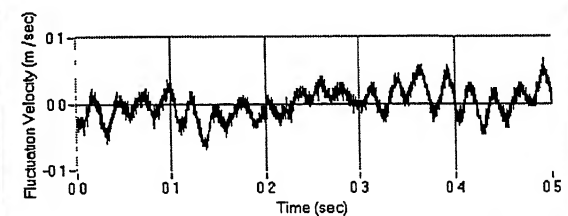
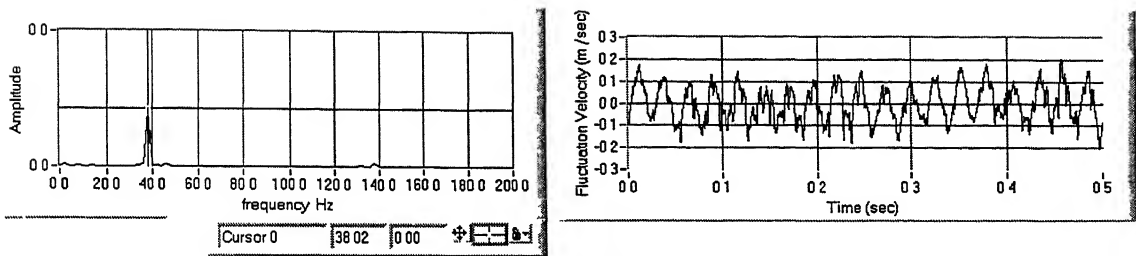
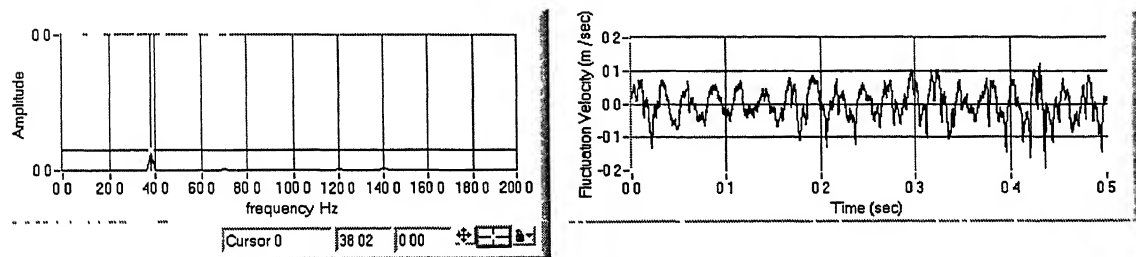


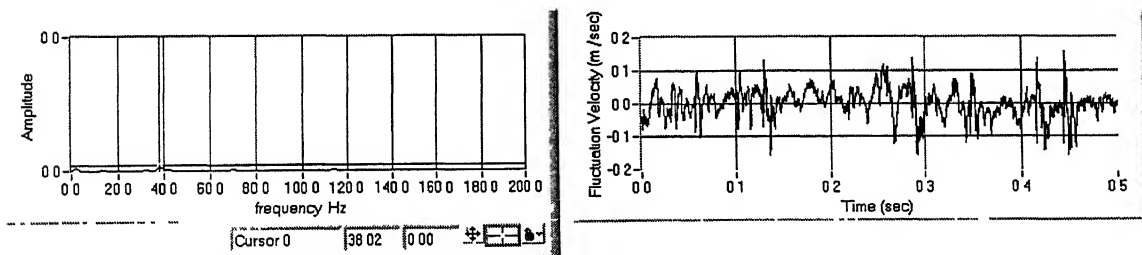
Fig. (4.30) Decay of Power spectra and Time trace in the vertical direction
Triangular cylinder 4 m/s model region



(a) Probe Position X_aY_1 (-14mm, 3mm)

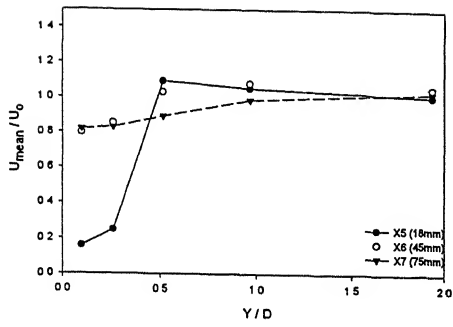


(b) Probe Position X_bY_2 (-19mm, 3mm)

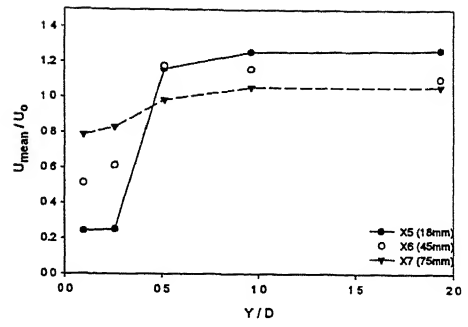


(c) Probe Position X_cY_3 (-27mm, 3mm)

Fig. (4.31) Power spectra and Time trace of velocity fluctuations for **triangular cylinder**
4 m/s upstream region

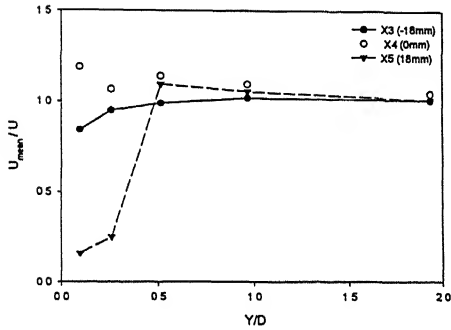


(a) Circular cylinder 10 m/s

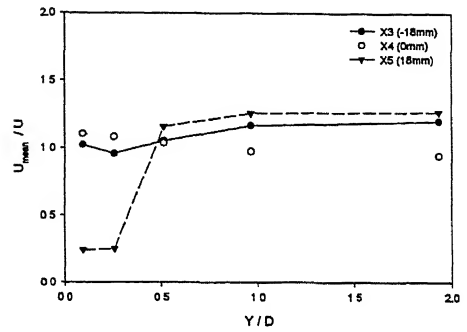


(b) Circular Cylinder 4 m/s

Wake Region

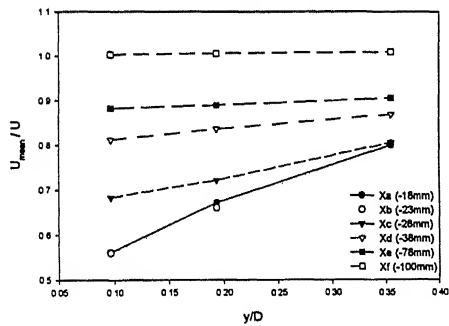


(c) Circular cylinder 10 m/s

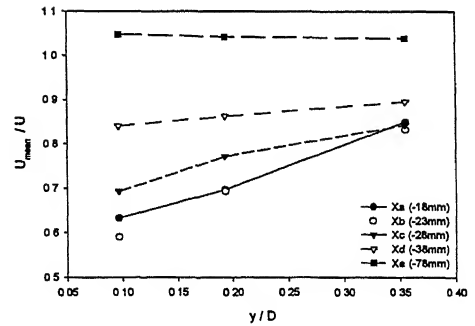


(d) Circular Cylinder 4 m/s

Model Region



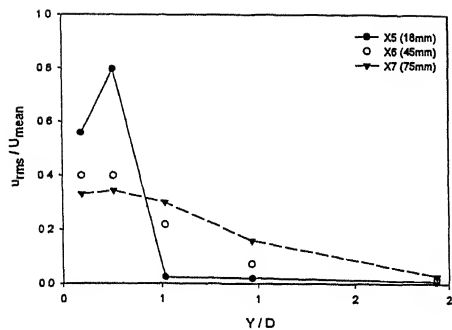
(e) Circular cylinder 10 m/s



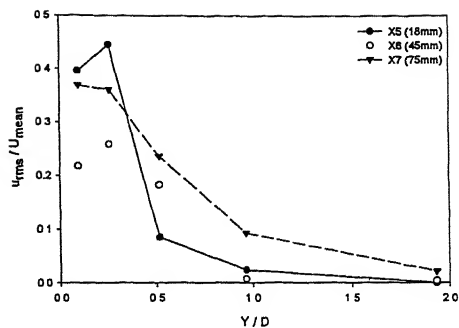
(f) Circular cylinder 4 m/s

Upstream Region

Fig. (4.32) Mean velocity distribution for Circular Cylinder

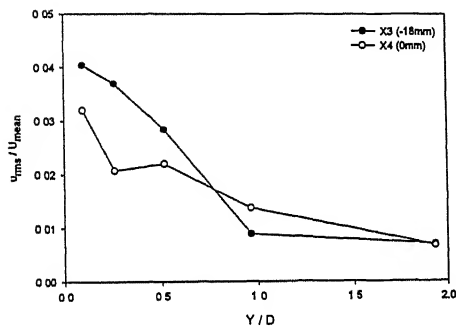


(a) Circular cylinder 10 m/s

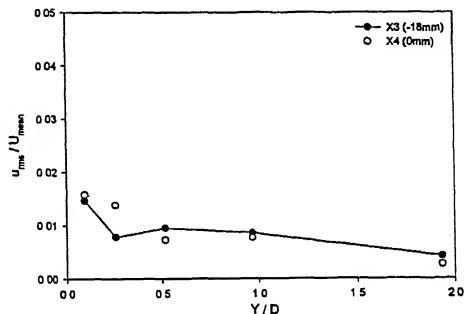


(b) Circular Cylinder 4 m/s

Wake region

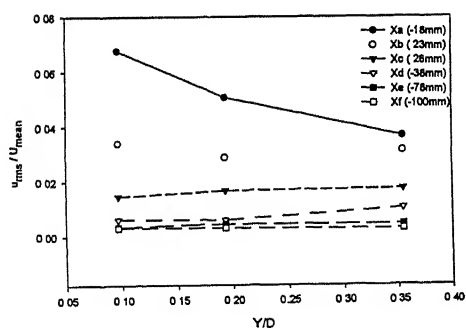


(c) Circular cylinder 10 m/s

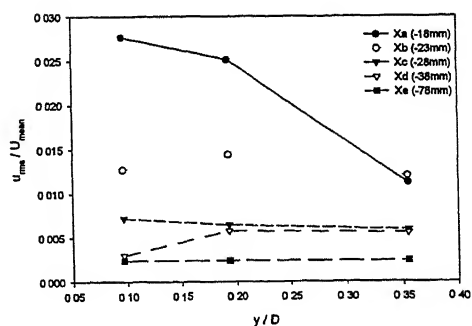


(d) Circular cylinder 4 m/s

Model Region



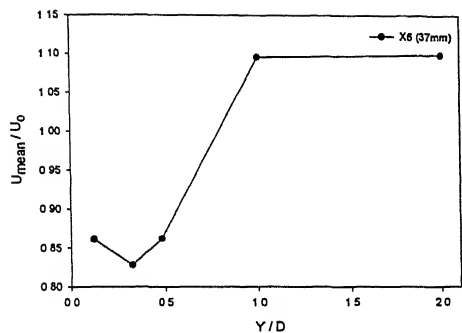
(e) Circular cylinder 10 m/s



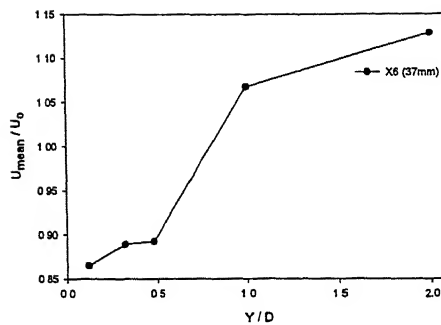
(f) Circular cylinder 4 m/s

Upstream Region

Fig. (4.33) RMS velocity fluctuations in the vertical direction for Circular Cylinder

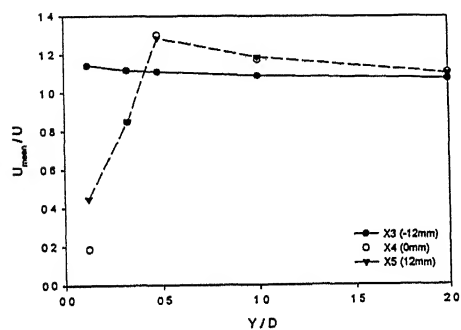


(a) Square cylinder 10 m/s

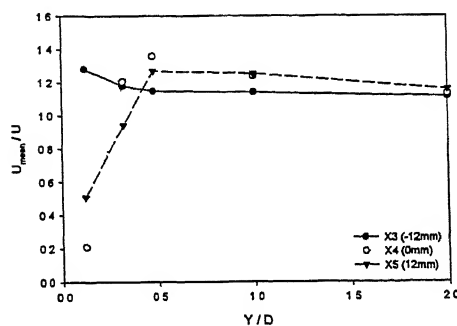


(b) Square cylinder 4 m/s

Wake Region

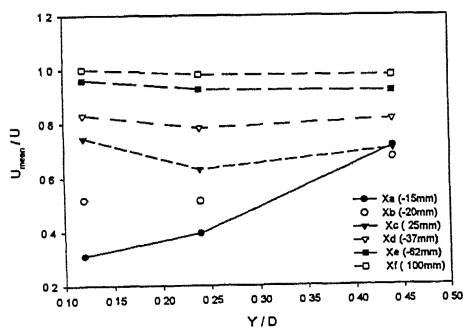


(c) Square cylinder 10 m/s

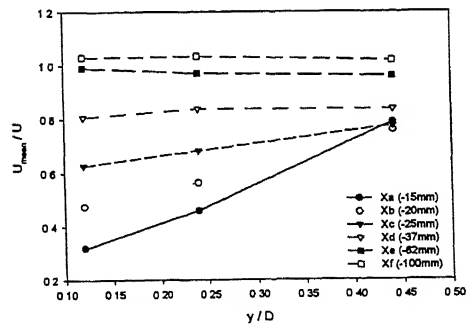


(d) Square cylinder 4 m/s

Model Region



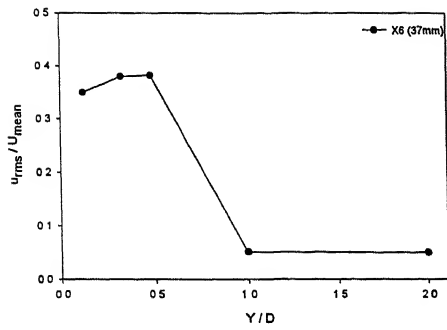
(e) Square cylinder 10 m/s



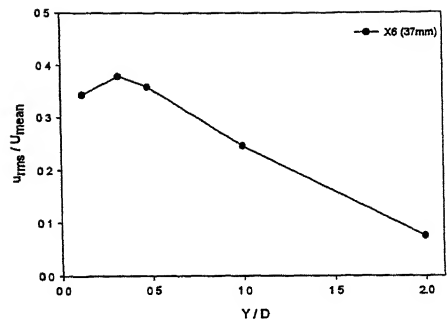
(f) Square cylinder 4 m/s

Upstream Region

Fig.(4.34) Mean velocity distribution for Square Cylinder

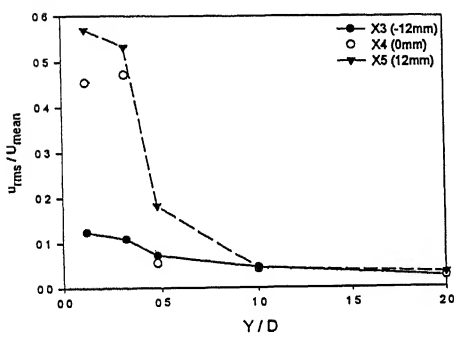


(a) Square cylinder 10 m/s

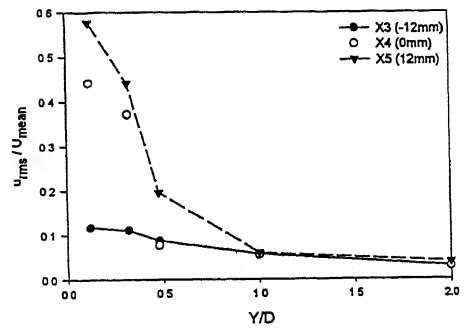


(b) Square cylinder 4 m/s

Wake Region

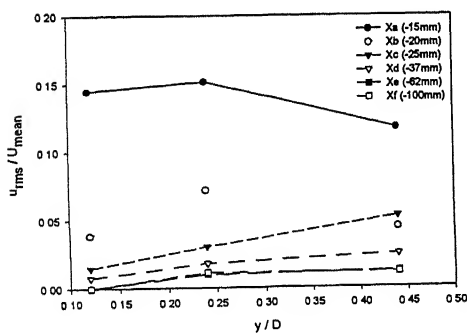


(c) Square cylinder 10 m/s

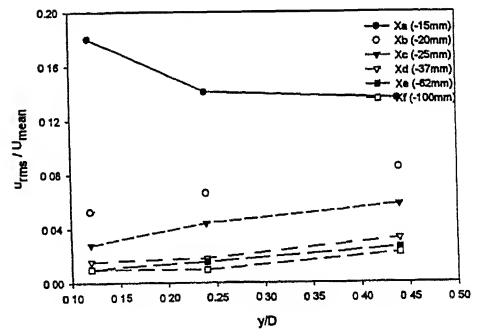


(d) Square cylinder 4 m/s

Model Region



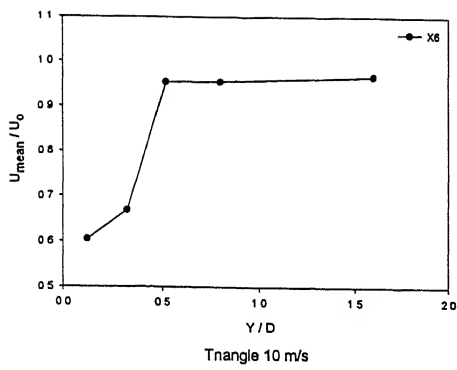
(e) Square cylinder 10 m/s



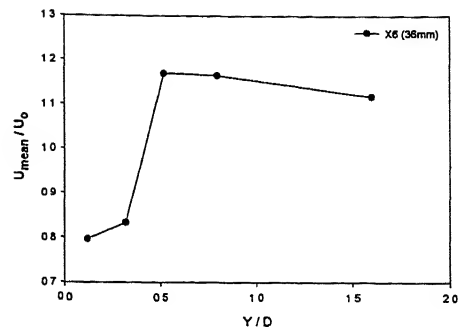
(f) Square cylinder 4 m/s

Upstream Region

Fig.(4.35) RMS velocity fluctuations in the vertical direction for Square Cylinder

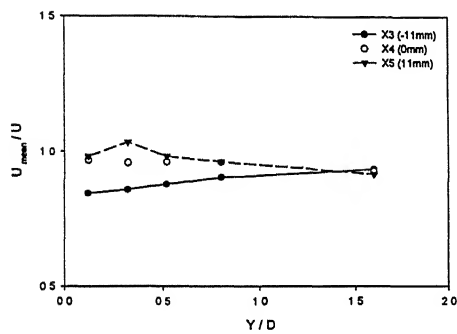


(a) Triangular cylinder 10 m/s

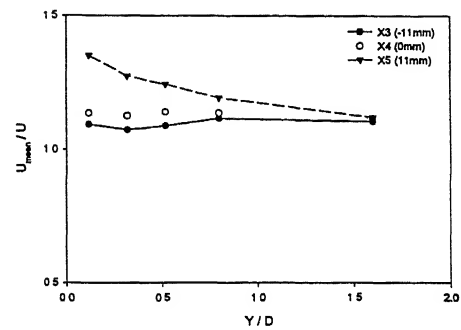


(b) Triangular cylinder 4 m/s

Wake Region

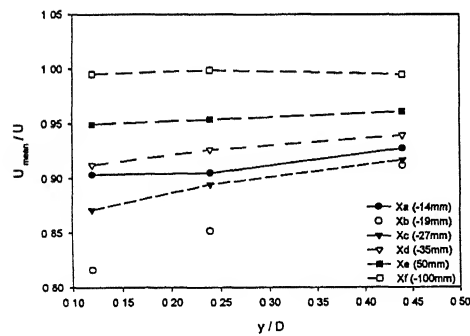


(c) Triangular cylinder 10 m/s

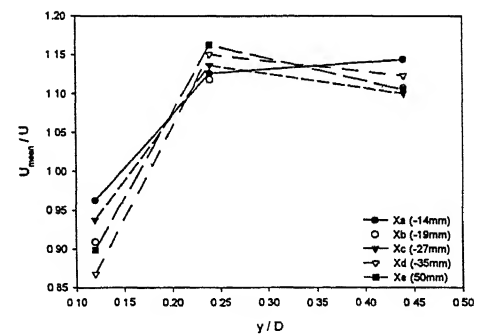


(d) Triangular cylinder 4 m/s

Model Region



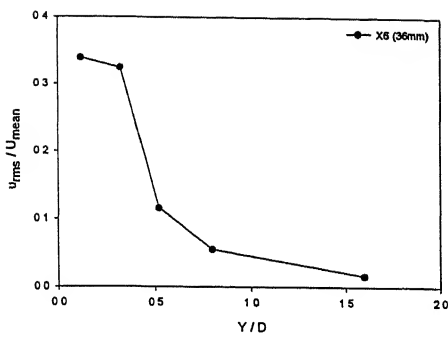
(e) Triangular cylinder 10 m/s



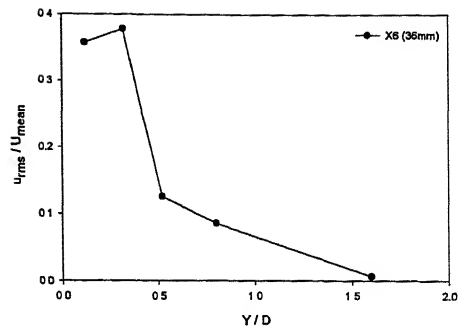
(f) Triangular cylinder 4m/s

Upstream Region

Fig. (4.36) Mean velocity distribution for Triangular Cylinder

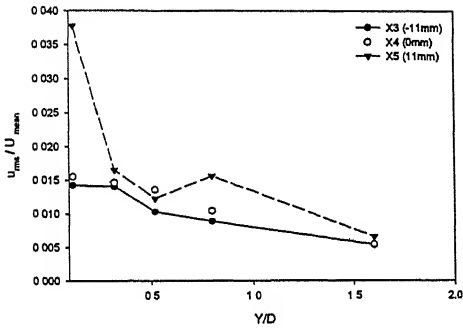


(a) Triangular cylinder 10 m/s

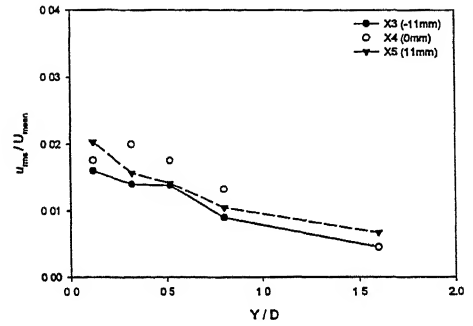


(b) Triangular cylinder 4m/s

Wake region

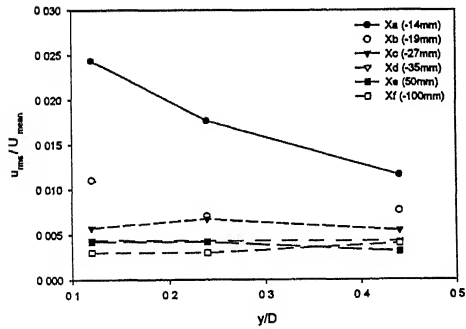


(c) Triangular cylinder 10 m/s

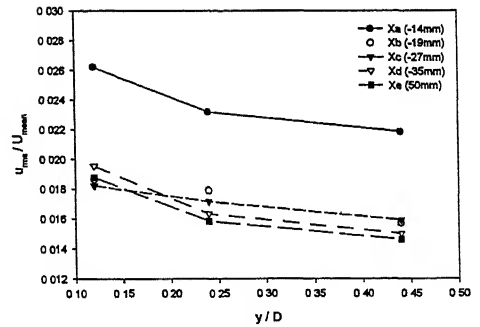


(d) Triangular cylinder 4m/s

Model region



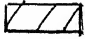
(e) Triangular cylinder 10 m/s



(f) Triangular cylinder 4m/s

Upstream Region

Fig.(4.37) RMS velocity fluctuations in the vertical direction for Triangular Cylinder

 Square Cylinder Okajima, A. (1982)
 x Circular Cylinder Roshko, A. (1961)

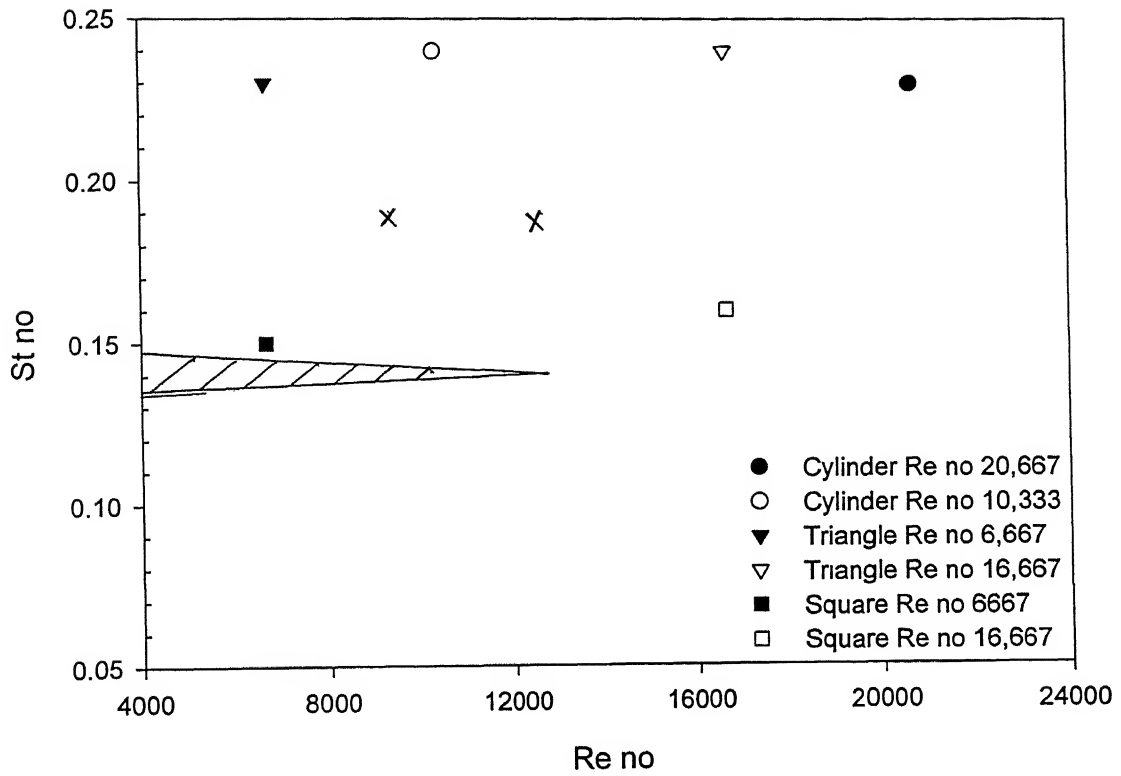
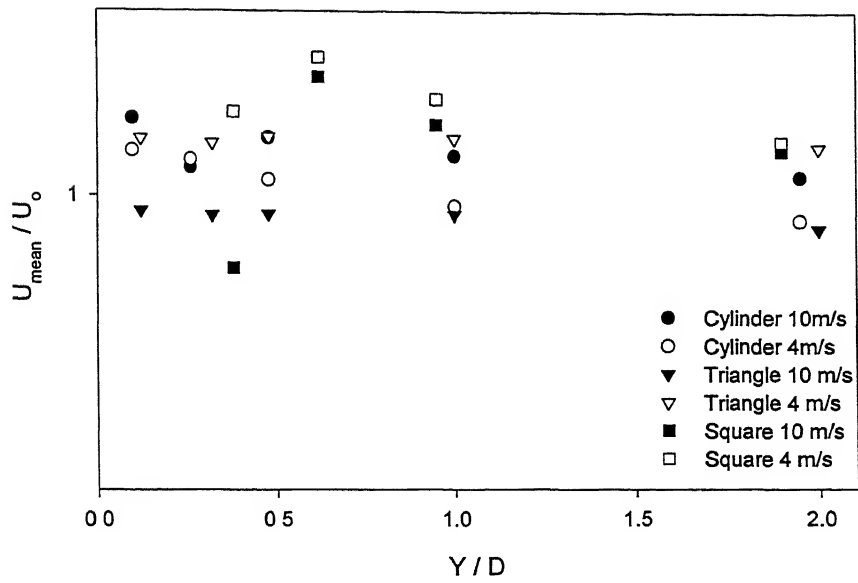
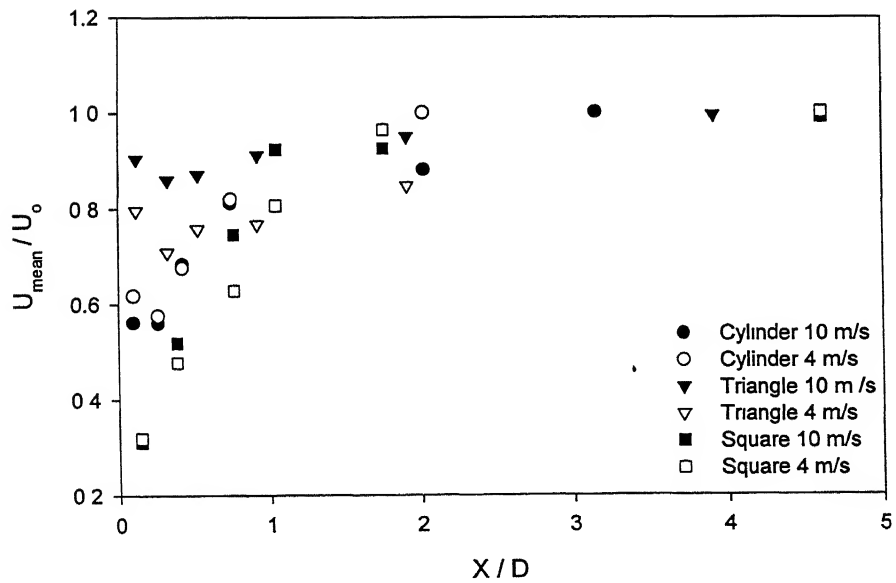


Fig. (4.38) Strouhal number vs Reynolds number for different models

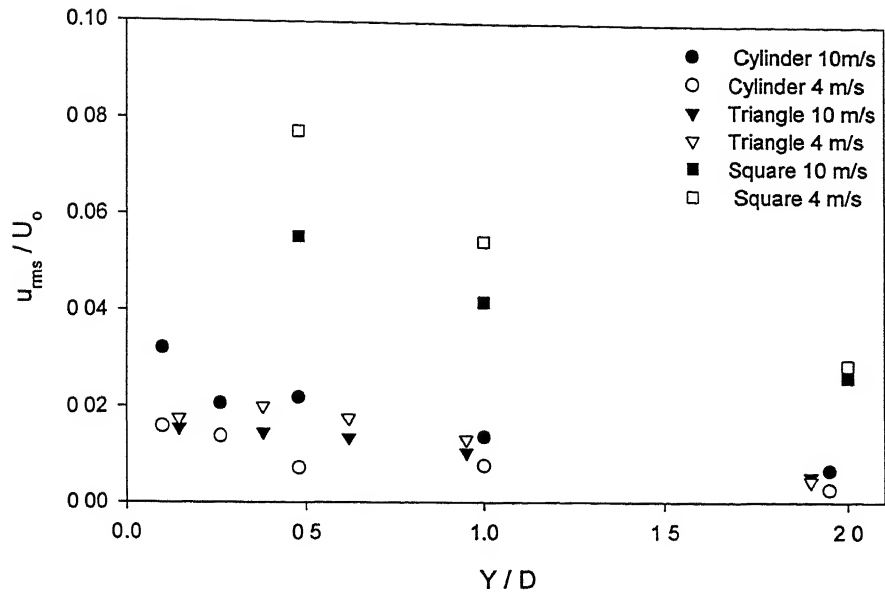


(a) Model region X_4 (0mm)

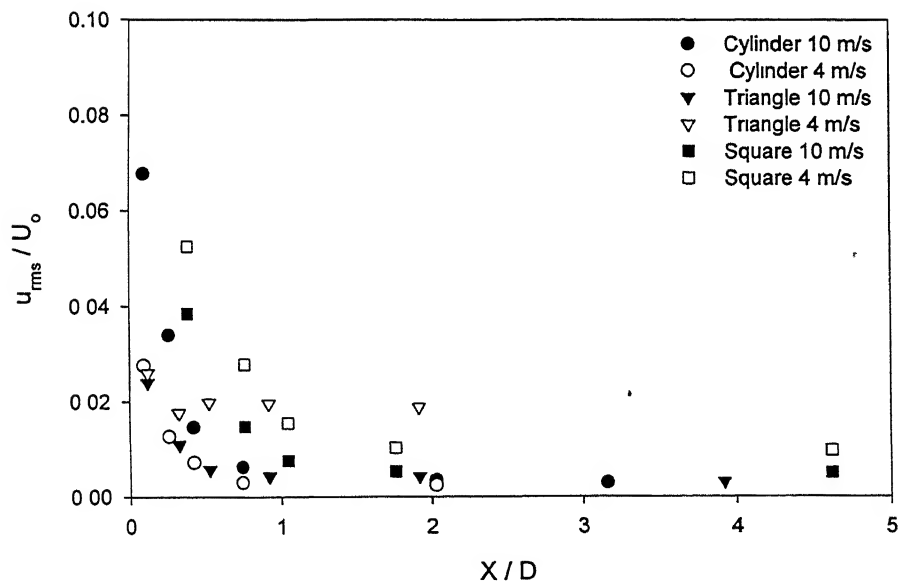


(b) Upstream region

Fig.(4.39) Variation of U_{mean} in the model and upstream region for different models



(a) Model region X_4 (0mm)



(b) Upstream region

Fig. (4.40) Variation of u_{rms} in the model and upstream region for different models

Chapter 5 CONCLUSIONS AND SUGGESTIONS

From the results of the present experimental investigation following conclusions can be made.

5.1 CIRCULAR CYLINDER MODEL

1. A single strong dominant spectral peak of the vortex shedding frequency in the power spectra appear in the wake region for both the test section speeds as expected.
2. The magnitude of the single dominant spectral peak decays to the almost zero at twice the diameter height in the y direction in the wake region, but the corresponding time traces still show weak vortex shedding oscillations of the dominant frequency.
3. The maximum amplitude of the dominant spectral peak at one diameter downstream location in the wake region is in good agreement with earlier experimental investigations of Roshko, A (1961) and Bearman, P. W. (1965).
4. Similar peaks of lesser magnitude of the dominant frequency appear in the model region indicating the effect of vortex shedding influence felt in the velocity fluctuations in the model region.
5. At probe position X_5 (18mm) corresponding to the rear stagnation point, in addition to the strong spectral peak, several sub-harmonics of the fundamental are observed both in the power spectra and time traces.
6. As in the case of wake region, the magnitude of the spectral peaks decay to free stream condition at twice the diameter height in the vertical direction, whereas the time trace still show vortex shedding oscillations.
7. The spectral peaks of the dominant vortex shedding frequency that appeared in the wake and the model regions appear also in the upstream region, but they are of smaller magnitude.

8. The magnitude of the spectral peak almost dies to zero at axial location X_c (-28mm) in the upstream region.
9. The mean velocity distribution and the RMS velocity fluctuations along the transverse direction in the wake region for all the three models show similar pattern for both the test section speeds and it is in good agreement with earlier experimental investigation by Sullerey, R. K. (1974).
10. The mean velocity distribution in the upstream region also show similar pattern for all the three models for both the test section speeds. The magnitude of the mean velocity is low at first near to the stagnation region up $X/D = 1$, after which it reaches free stream condition at location X_f (-100mm) for all the models in both the speed cases.
11. The magnitude of RMS velocity fluctuations in the upstream region is very low compared to the wake and upstream region.
12. The maximum RMS velocity fluctuations in the upstream region extend up $X/D=1$ after which there is no much variation in the RMS velocity fluctuations.

5.2 SQUARE AND TRIANGULAR CYLINDER MODELS

1. The spectral peak and time traces of hot wire for the square cylinder and the triangular cylinder in the wake region show similarity in their patterns with that of the circular cylinder for both the test section speed conditions.
2. For the square cylinder at probe location X_4Y_1 (0mm, 16mm) there is no single dominant spectral peak, as the boundary layer separation would have started from the leading edge and there is no single dominant peak in the separated turbulent region.
3. The magnitude of the spectral peak is maximum in the model region at location X_4 (0mm) for the square cylinder than in the wake region.
4. For the square cylinder at probe location X_5Y_1 (12mm, 16mm), sub-harmonics of the fundamental frequency are observed.
5. The spectral peak and time traces for the square cylinder and the triangular cylinder show similarity in their pattern in the upstream region with that of the circular cylinder for both the test section speed conditions. Presence of the

spectral peak of the dominant vortex shedding frequency in the upstream region is due to the effect of the vortex shedding on the velocity fluctuations in the upstream region.

6. In the case of triangular cylinder the velocity fluctuation signals are too weak to record the magnitude but the spectra show the presence of the spectral peak of the dominant frequency up to location of one base height of the model in the upstream region.
7. After this location there is no spectral peak of any frequency and also the time trace shows free stream condition in the upstream region.

5.3 STROUHAL NUMBER

1. The Strouhal number is same all around a model for a particular free stream wind speed for the all the 2-D bluff body models.
2. The Strouhal number for circular cylinder and triangular cylinder is around 0.23 where as for the square cylinder it is around 0.15.
3. Comparisons of the Strouhal number with earlier experimental investigations are in close agreement with the present findings.

5.4 SUGGESTIONS FOR FUTURE WORK

- Only two Reynolds numbers are taken in to consideration for the present investigation, this can be extended for a wider Reynolds number range.
- Presence of splitter plate behind a bluff body suppresses the vortex shedding formation in the wake and hence the splitter plate can be introduced to study the effect of splitter plate upstream of the bluff bodies.
- In the present investigation only stream wise fluctuations have been measured. The v' and w' fluctuation components and the turbulent shear stress measurements can be made with X hot wire in the upstream region. In addition correlation measurements can also be made in the upstream region.
- The angle of orientation of the models can be varied especially in the case of square and triangular cylinder, as significant changes have been reported in literature for 2-D square and triangular prism at an angle of attack.

REFERENCE

1. Roshko, A. 1960, "Experiments on the flow past a circular cylinder at very high Reynolds number", *J. Fluid Mech*, Vol. 10, pp. 345-356.
2. Schlichting, H. 1960, "Boundary Layer Theory", *MaGRAWH-HiLL* publication.
3. Gerrard, J. H. 1965, "The mechanics of the formation region of vortices behind bluff bodies", *J. Fluid Mech*, Vol. 25, pp. 401-413.
4. Vickery, B. J. 1966, "Fluctuating Lift and Drag on a long cylinder of square cross-section in a smooth and in a turbulent stream", *J. Fluid Mech*, Vol.25, pp.481-494.
5. Bearman, P. W. 1968, "On vortex shedding from a circular cylinder in the critical Reynolds number regime", *J. Fluid Mech*, Vol.37, pp.577-585.
6. Nakabuchi, H. *et al.* 1968, "An experimental study of aerodynamic drag of rectangular cylinders", *J. Japan Soc. Aero. Space Sci.* Vol. 16, pp.1-5.
7. Surry, D. 1971, "Some effects of intense turbulence on the aerodynamics of a circular cylinder at subcritical Reynolds number", *J. Fluid Mech*, Vol.52, pp.543-563.
8. Sullerey, R. K. 1974, "Investigation in the Low Speed Turbulent Near Wake of Bluff Bodies", *Ph.D. Thesis, Dept. of Aerospace Engg., I.I.T. Kanpur.*
9. Otsuki, Y. *et al.* 1974, "A note on the aeroelastic instability of a prismatic bar with square section", *J. Sound Vib*, Vol. 34, pp. 233-248.

10. Lee, B. E. 1975, "The effect of turbulence on the surface pressure field of a square prism", *J. Fluid Mech*, Vol. 69, pp. 263-282.

11. Achenbach, E. and Heinecke, E. 1981, " On vortex shedding from smooth and rough cylinders in the range of Reynolds numbers $6 \cdot 10^3$ to $5 \cdot 10^6$ ", *J. Fluid Mech*., Vol. 109, pp. 239-251.

12. Okajima, A. 1982, "Strouhal numbers of rectangular cylinders", *J. Fluid Mech*, Vol.123, pp.379-398.

13. Kiya, M. *et al.* 1982, "A contribution to the free-stream turbulence effect on the flow past a circular cylinder", *J. Fluid Mech*, Vol. 115, pp. 151-164.

14. Nakagawa, T. 1986, "Vortex shedding behind a square cylinder in transonic flows", *J. Fluid Mech*, Vol. 178, pp. 303-323.

15. West, G. S. and Apelt, C. J. 1989, " The effect of tunnel blockage and aspect ratio on the mean flow past a circular cylinder with Reynolds number between 10^4 and 10^5 ", *J. Fluid Mech*, Vol.118, pp. 1-26.

16. Williamson, C. H. K. 1989, "Oblique and parallel modes of vortex shedding in the wake of a circular cylinder at low Reynolds numbers", *J. Fluid Mech*, Vol. 206, pp. 579-627

17. Franke, R. *et al.* 1990, "Numerical calculation of laminar vortex shedding flow past cylinders", *J. of Wind Engineering and Industrial Aerodynamics*, Vol. 35, pp.237-257.

18. Bruesti, G. 1998, "Low aspect-ratio triangular prisms in cross-flow: measurements of the wake fluctuating velocity field", *J.of Wind Engineering and Industrial Aerodynamics*, Vol. 74-76, pp. 713-723.

19. Pope, A. *et al* 1999, "Low Speed Wind Tunnel Testing", a *Wiley-Interseience* Publication.
20. Park, C. *et al.* 2000, "Free end effects on the near wake flow structure behind a finite circular cylinder", *J. of Wind Engineering and Industrial Aerodynamics*, Vol. 88, pp.231-246.
21. Nishimura, H and Taniike, Y. 2001, "Aerodynamic charatersitics of fluctuating forces on a circular cylinder", *J.of Wind Engineering and Industrial Aerodynamics*, Vol. 89, pp. 713-723.